PNE-507
FINAL REPORT

Plowshare civil, industrial and scientific uses for nuclear explosives

UNITED STATES ARMY CORPS OF ENGINEERS

BRUNEAU PLATEAU, IDAHO
30 September 1965

PROJECT PRE-SCHOONER II

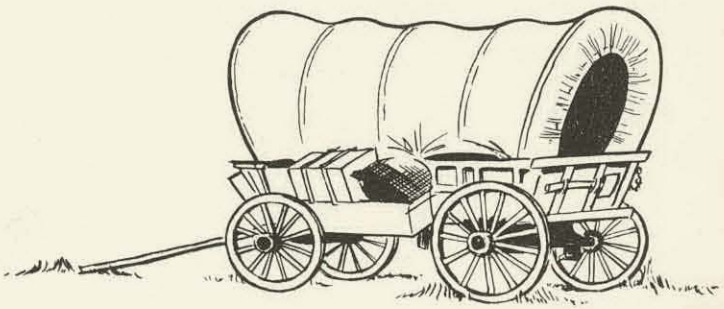

TECHNICAL DIRECTOR'S SUMMARY REPORT

B. C. HUGHES

U. S. Army Engineer Nuclear Cratering Group
Livermore, California

U. S. Army Engineer Nuclear Cratering Group
Livermore, California

■ ISSUED: OCTOBER 1966

DISCLAIMER

Printed in USA. Price $2.00. Available from the Clearinghouse for Federal
Scientific and Technical Information, National Bureau of Standards
U. S. Deparment of Commerce, Springfield, Virginia

PNE-507
Final Report

PROJECT PRE-SCHOONER II

TECHNICAL DIRECTOR'S SUMMARY REPORT

B. C. Hughes
U. S. Army Engineer Nuclear Cratering Group

R. H. Benfer
U. S. Army Engineer Nuclear Cratering Group

W. C. Day
U. S. Army Engineer Nuclear Cratering Group

K. L. Larner
U. S. Army Engineer Nuclear Cratering Group

M. Heusinkveld
Lawrence Radiation Laboratory
Livermore, California

R. E. Marks
Lawrence Radiation Laboratory
Livermore, California

R. F. Rohrer
Lawrence Radiation Laboratory
Livermore, California

Roland F. Beers, Inc.
Alexandria, Virginia

December 1965

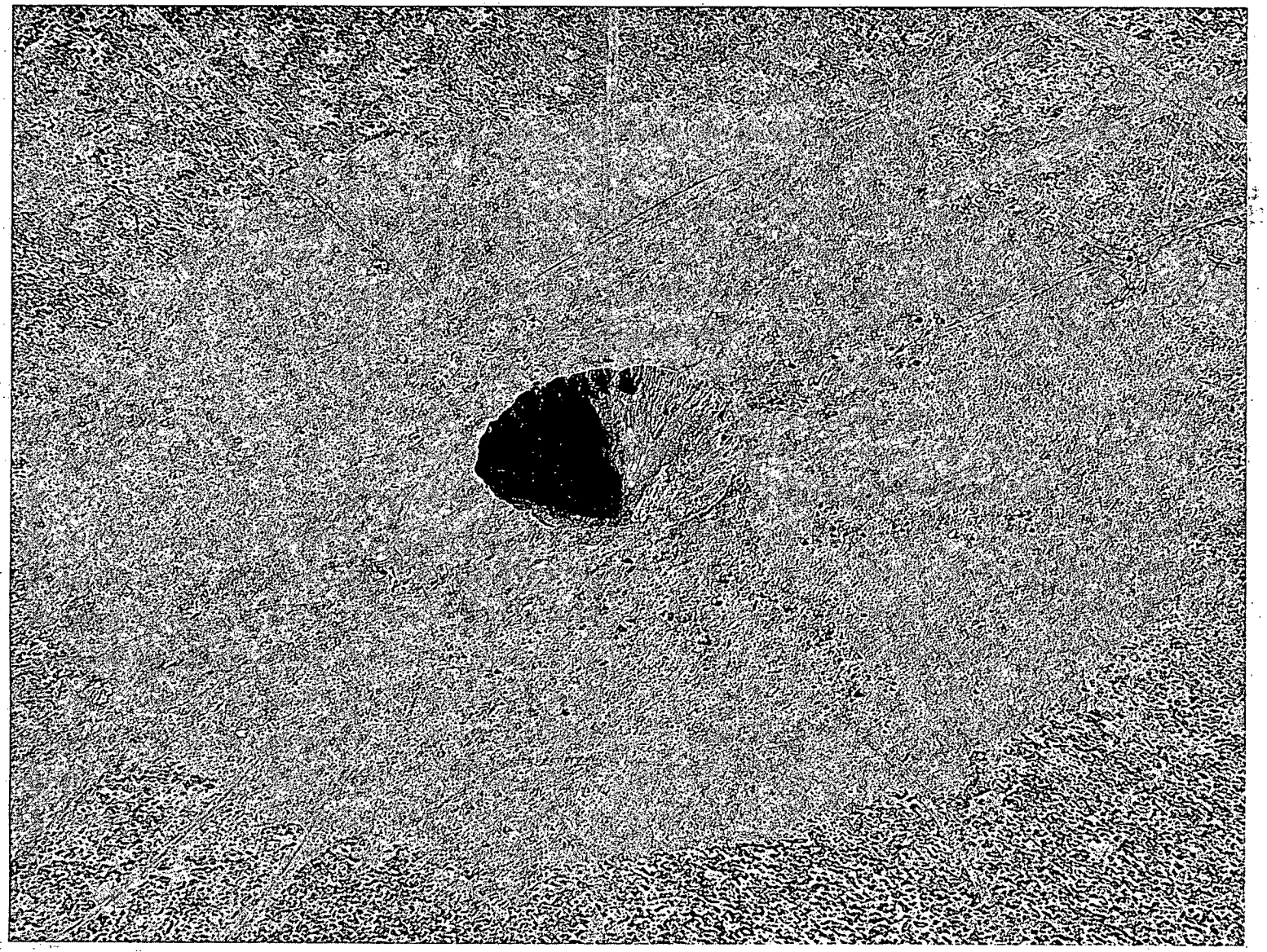

Pre-Schooner II Crater.

ABSTRACT

Project Pre-Schooner II was a chemical explosive single-charge cratering experiment conducted by the U. S. Army Engineer Nuclear Cratering Group as a correlation detonation for the Atomic Energy Commission's proposed Plowshare 100-kt Schooner nuclear cratering experiment. Pre-Schooner II was executed as a part of the joint AEC-Corps of Engineers nuclear excavation research program. The primary purpose of this experiment was to improve the knowledge of cratering in a hard, dry rock and to provide information which can be used in the emplacement design of the Schooner event and in the assessment of the operational safety aspects of that event.

The Pre-Schooner II design consisted of a 100-ton liquid explosive nitromethane (CH_3NO_2) charge emplaced in a spherical cavity at a depth of 71 feet in the rhyolitic rock formation of the Bruneau Canyon region in southwestern Idaho. The charge was detonated on 30 September 1965 at 1709 MST. As a result of a leak which developed in the cavity, there were only 85.5 tons of nitromethane in the cavity at detonation time. This charge weight of nitromethane has an energy equivalent yield of 94.6 tons.[1]

The crater produced by the detonation had an apparent crater radius of 95.2 feet and an apparent crater depth of 60.7 feet. The apparent crater volume was 24,780 yd^3, and the average lip crest height was 17.2 feet. The maximum range of missiles resulting from the detonation was 2320 feet.

The results of surface motion studies which were based on analysis of high-speed photography of the motion of a falling-mass target at Ground Zero (GZ) indicate that a peak spall velocity of 129 ft/sec occurred at GZ at 27 msec after zero time.

The results of the subsurface measurements program indicate that: (1) the signal time of arrival measurements and peak stress measurements in the horizontal direction from the shot point were in close agreement with the SOC computer calculation predictions; (2) the signal time of arrival and peak stress measurements in the vertical direction evidenced considerable scatter and were generally lower (for stress measurements) or occurred at a later time (for time of arrival measurements) than was predicted by the SOC calculation; (3) a peak positive vertical acceleration of 3000 g was measured by the accelerometer located near the upper surface of the rhyolite medium approximately 10 feet below the surface of the ground; and (4) the cavity pressure

---

[1] Based on the assumption that an energy equivalent yield of one ton releases 10^9 cal and that nitromethane releases 1220 cal/gm of charge weight.

measurements, recorded over the time period that the fluid column functioned properly, agreed quite well with predicted measurements.

Strong motion measurements recorded at two stations, located 2.4 and 4.7 km east of GZ, produced acceleration data which agree quite well with predictions. The observed displacements at these two stations and the velocities recorded at four other stations located east and north of GZ were higher than predicted.

The following were maximum observed cloud dimensions: crosswind base surge radius, 2100 feet; base surge height, 1060 feet; main cloud radius, 875 feet; and main cloud height, 1400 feet.

Preliminary analysis of the close-in air blast measurements indicates that the ground-shock-induced pressures from the Pre-Schooner II detonation were twice those from previous cratering detonations at comparable scaled ranges. Analysis of the microbarograph measurements show that the average long-range air blast transmission factor for Pre-Schooner II was 0.19.

It should be noted that the observations, results, and conclusions outlined above are preliminary and subject to change based upon detailed analyses and interpretation of data. Final results will be presented in the reports listed in Appendix A.

CONTENTS

CONTENTS (Continued)

TABLES (Continued)

FIGURES

FIGURES (Continued)

FIGURES (Continued)

THIS PAGE

WAS INTENTIONALLY

LEFT BLANK

CHAPTER 1

INTRODUCTION

Project Pre-Schooner II was a chemical explosive, single-charge cratering experiment conducted by the U. S. Army Engineer Nuclear Cratering Group (NCG) as a correlation detonation for the Atomic Energy Commission (AEC) proposed Plowshare Schooner 100-kt nuclear cratering experiment. Pre-Schooner II was executed as a part of the joint AEC-Corps of Engineers nuclear excavation research program.

The purpose of this report is to discuss the objectives, scope, and preliminary results of Pre-Schooner II. Final reports, as listed in the appendix, will be prepared for each Pre-Schooner II Technical Program. These final reports will provide a complete coverage of the objectives, experimental methods, results obtained, conclusions reached, and recommendations for future work, as appropriate, for each technical program.

1.1 OBJECTIVES OF EXPERIMENT

Project Pre-Schooner II was designed to accomplish the following objectives:

a. To improve the knowledge of cratering in a hard, dry rock and to provide information which can be used in the emplacement design of the Schooner event and in assessing the operational safety aspects of that event.

b. To provide information on cratering physics in a hard, dry rock medium which can be used in the theoretical cratering calculations program.

c. To give interested agencies an opportunity to test new scientific measurements instrumentation and techniques to determine the suitability of using such methods on nuclear cratering experiments.

d. To provide data on the engineering properties of the crater which can be used as input into studies pertaining to the stability of crater slopes and other aspects which influence the engineering usefulness of explosion-produced craters.

1.2 TECHNICAL PROGRAMS AND ORGANIZATION

The following technical programs were included in Pre-Schooner II to accomplish the project objectives:

a. Crater Studies to include: (1) measurement of apparent crater dimensions by aerial stereophotogrammetric techniques and analysis of the extent of missile throwout and (2) geological investigations to establish preshot conditions and postshot

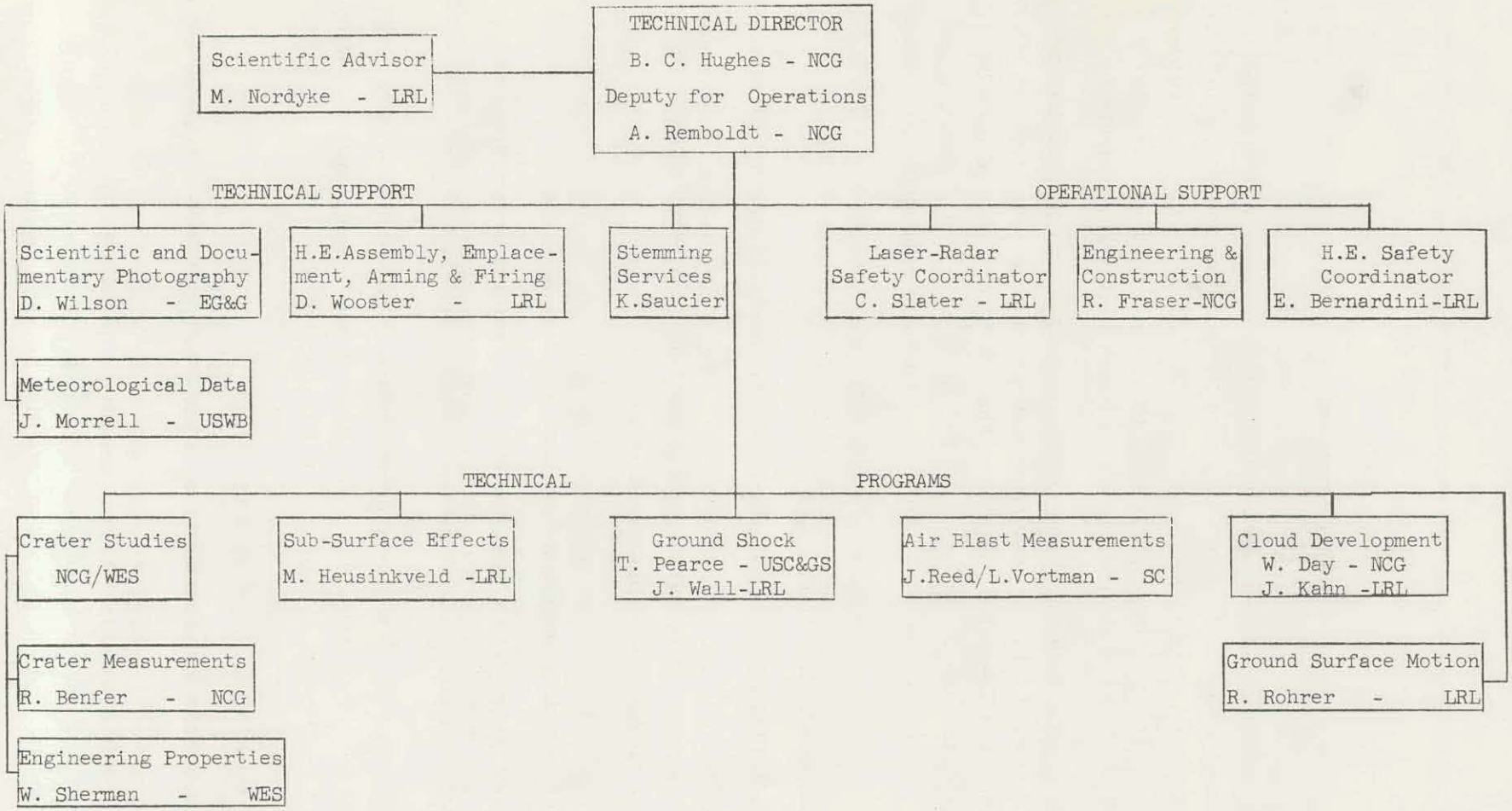

NCG - U. S. Army Engineer Nuclear Cratering Group
LRL - Lawrence Radiation Laboratory
SC - Sandia Corporation
USWB - U. S. Weather Bureau
EG&G - Edgerton, Germeshausen & Grier
WES - U. S. Army Engineer Waterways Experiment Station
USC&GS - U. S. Coast & Geodetic Survey

Figure 1.1 Technical Director's Organization, Project Pre-Schooner II

investigations to delineate the zones in the vicinity of the crater which were affected by the detonation and the nature of the changes in these zones.

b. Subsurface Effects Measurements to measure early subsurface wave phenomena, late cavity pressure, and late vertical subsurface ground motion.

c. Ground Shock Measurements to collect ground motion data which may be used to facilitate more accurate ground motion predictions for the Schooner event.

d. Close-in and Long Range Air Blast Measurements to establish air blast attenuation factors for explosions at optimum depth in hard rock and to compare results with data from other cratering tests.

e. Cloud Development Studies to include: (1) measurement of the main cloud and base surge growth and displacement with time using cloud cameras and (2) a laser-radar cloud tracking operation to determine the feasibility of using the laser to obtain estimates of distances to the cloud and cloud dimensions at times when standard photographic methods are no longer effective.

f. Surface Motion Studies to record ground surface motion in the vicinity of Ground Zero (GZ) using high-speed photography.

B. C. Hughes of NCG was the Pre-Schooner II Technical Director. Figure 1.1 shows the Technical Director's organization for the conduct of the experiment.

CHAPTER 2

GENERAL DESCRIPTION OF EXPERIMENT

2.1 DESCRIPTION OF SITE

2.1.1 Regional Area (Reference 1). The site selected for Project Pre-Schooner II was adjacent to the proposed Project Schooner site on the Bruneau Plateau, approximately 40 miles southeast of Bruneau, Idaho (Figure 2.1). The Bruneau Plateau has a gently rolling surfacethat slopes gradually north toward the Snake River Valley. Narrow, steep-sided canyons of the Bruneau and Jarbridge Rivers cut through the plateau to depths of 900 feet near the Schooner and Pre-Schooner II sites.

The site area is located between the East and West Forks of the Bruneau River. The rock types occurring in the site area are a thick sequence of rhyolitic or latitic lava flows, welded ask flows, and obsidian flows overlain by interbedded basalt flows and stream and lake deposits.

2.1.2 Site Selection (References 1 and 2). Since Project Pre-Schooner II was designed as a correlation cratering detonation for the proposed Schooner event, an attempt was made to select a site which was a geological analog to the Schooner site. Five sites near the Schooner site were explored by a combination of refraction seismic surveys and limited core drilling. Based on the data obtained from this preliminary investigation, the most analogous site was selected for Pre-Schooner II. Figure 2.2 shows a comparison of the geological cross sections of the Schooner and Pre-Schooner II sites.

2.1.3 Site Area (References 1, 2, 3, and 4). The Pre-Schooner II site is located approximately 7600 feet southwest of the Schooner site. The site is a local depression in an east-west trending ridge. This depression is bordered to the north and south by low hills and to the west by a relatively high volcanic dome. The emplacement hole for Pre-Schooner II was designated Hole No. 2.7 (Figure 2.3) and located at the following coordinates: N 267,639.53, and E 547,783.11.

The scope of preshot geologic investigations for Pre-Schooner II included refraction seismic surveying, the drilling of 13 core borings (the deepest of which was 150 feet), and an uphole seismic survey near the GZ point. The locations of these explorations are shown in Figure 2.3.

The subsurface materials occurring at the site are silty overburden underlain by vitrophyre, vitrophyre breccia, and felsite. Mineralogically, the rock types are all rhyolite. Detailed geological cross sections of the Pre-Schooner II site are shown in

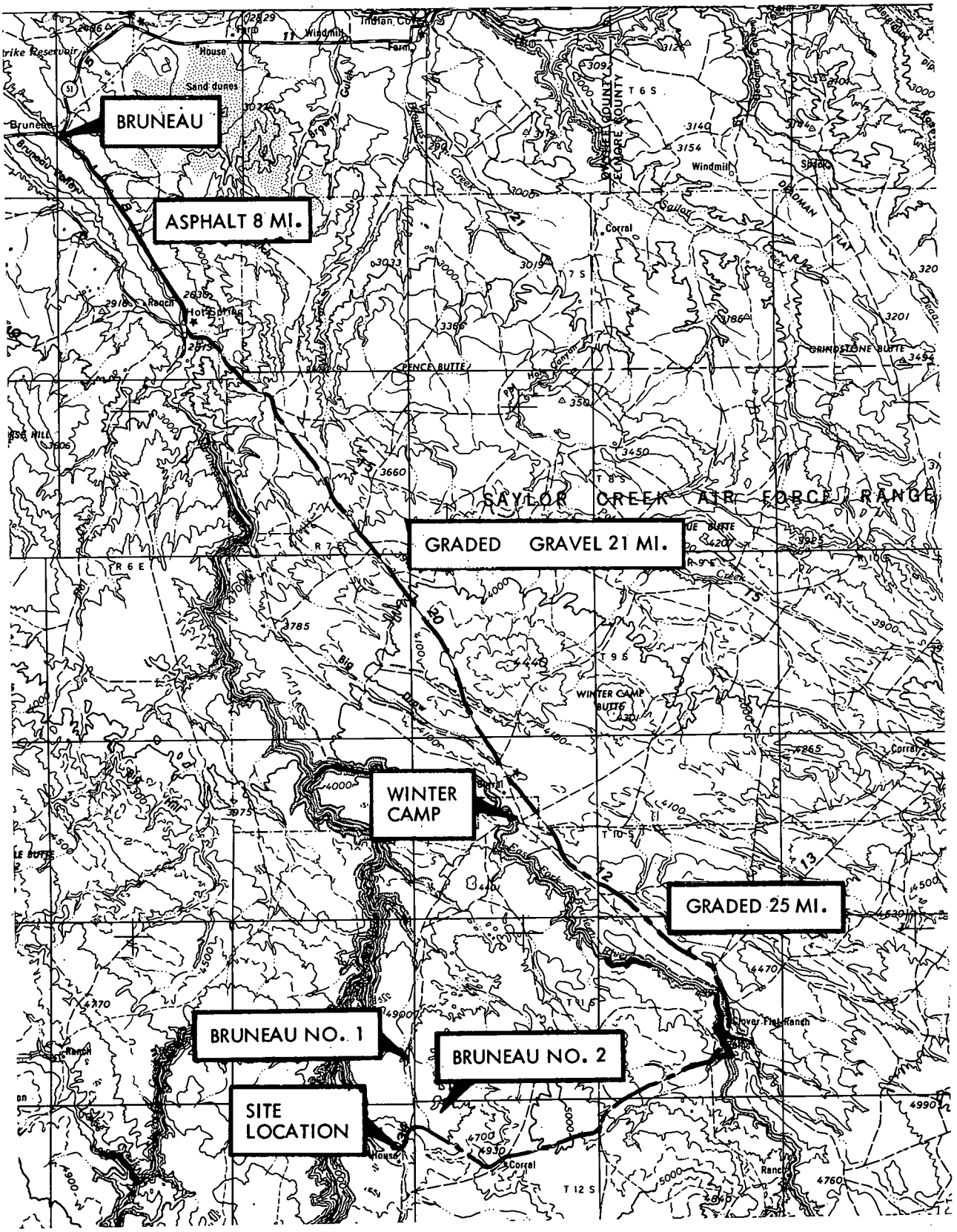

Figure 2.1 Project Pre-Schooner II Site Location.

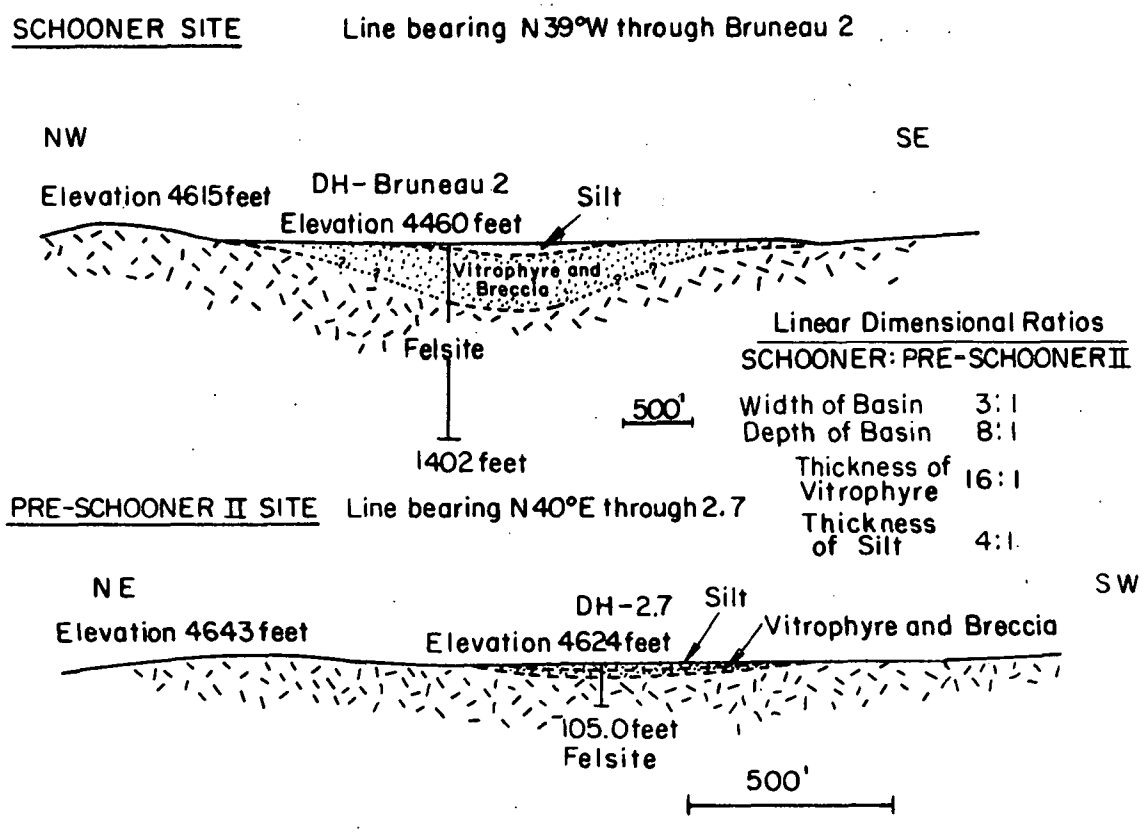

Figure 2.2 Comparison of Geological Cross Sections of Pre-Schooner II and Schooner Sites.

Figure 2.4. The vitrophyre consists of light-colored feldspar crystals (phenocrysts) set in a black glassy groundmass. It is closely fractured by small arcuate cracks (perlitic cracks). The virtophyre breccia consists of gravel to block-sized fragments of black vitrophyre set in a red granular groundmass of sand-sized fragments of glass. Both the vitrophyre and vitrophyre breccia will shatter into sand-sized or pea-gravel-sized fragments when struck with a hammer. The felsite is composed of light-colored feldspar crystals (phenocrysts) set in a grayish (cryptocrystalline) groundmass. It is moderately to highly fractured.

Average values of the physical properties of the medium at the Pre-Schooner II site are plotted in Figure 2.5 as a function of depth below the ground surface.

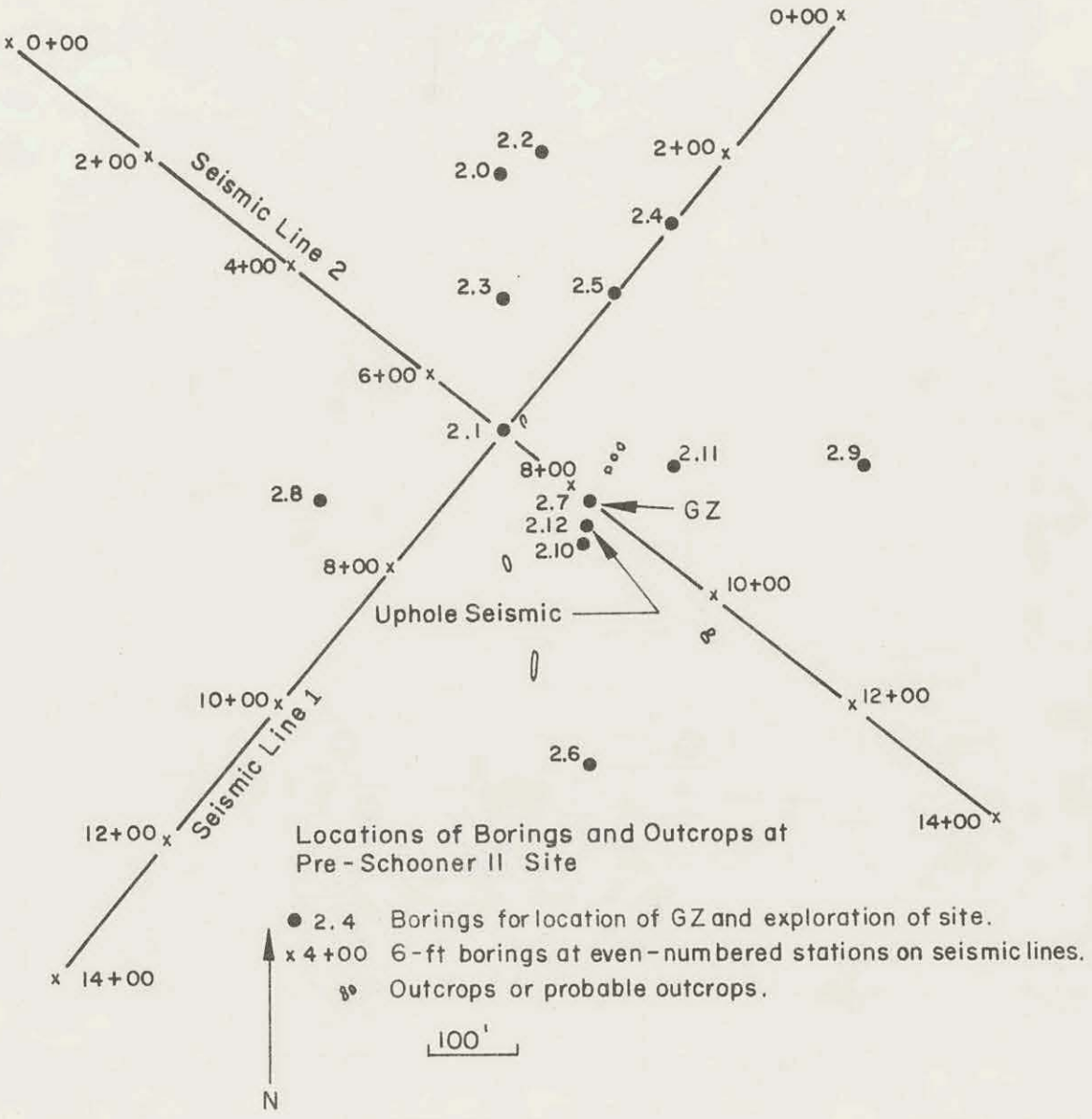

Figure 2.3 Locations of Explorations at the Pre-Schooner II site.

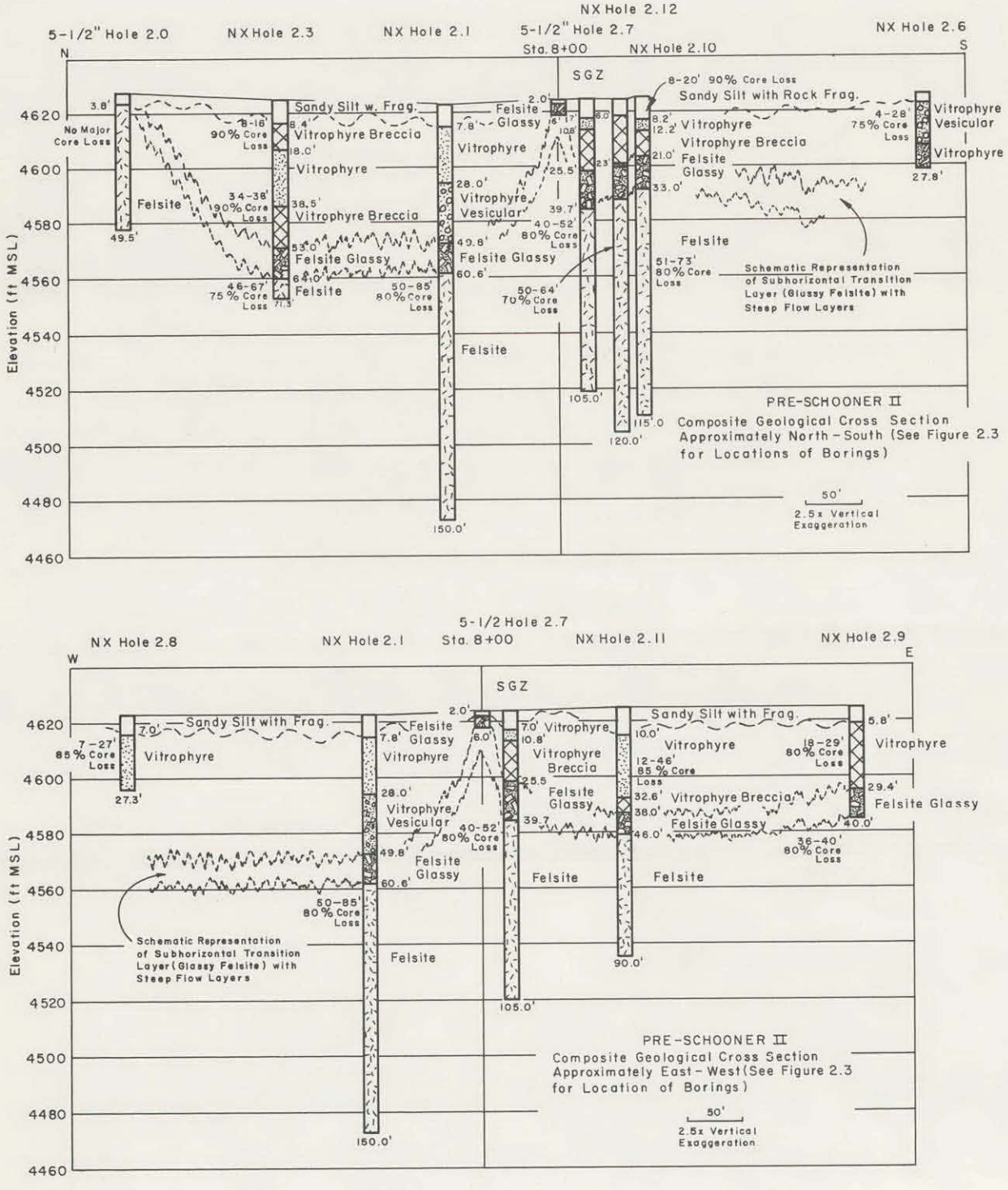

Figure 2.4 Detailed Geological Cross Sections at Pre-Schooner II Site.

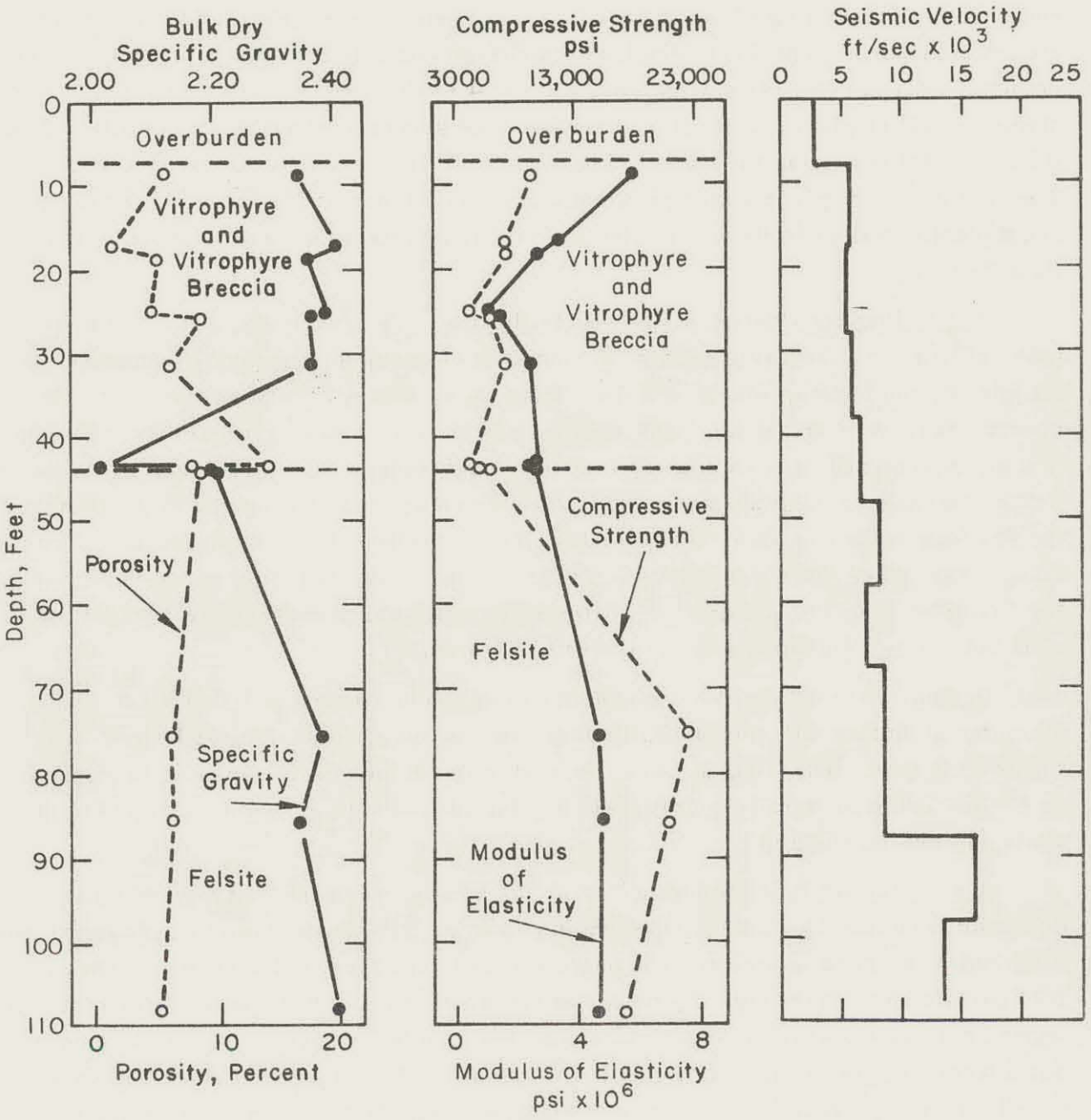

Figure 2.5 Average Physical Properties of Medium at Pre-Schooner II Site.

2.2 DESCRIPTION OF CHARGE EMPLACEMENT (Reference 5)

2.2.1 General Description. The Pre-Schooner II design consisted of a 100-ton, liquid explosive, nitromethane (CH_3NO_2) charge emplaced at a depth of 71 feet in the rhyolitic rock formation of the Bruneau Canyon region in southwestern Idaho. Construction required to properly emplace the charge consisted of: (1) drilling a 36-inch-diameter access hole, (2) mining out a spherical cavity approximately 18 feet in diameter, (3) emplacing a booster charge and the properly-sized aluminum fill and vent lines, and (4) stemming the access hole with concrete keyed into the existing rock. The cavity was prepared with a pneumatically applied mortar lining over wire mesh and a plastic sealant (Adiprene L-100) to bring it into tolerance and to provide liquid tightness.

2.2.2 Booster Charge and Downhole Hardware Emplacement. After the access hole drilling, cavity mining and lining, and shear keyway mining operations were completed, the booster charge and the hardware necessary for filling the cavity with nitromethane were emplaced. The booster charge consisted of approximately 25 pounds of C-4, 2 pounds of 9404 explosive, four SE-1 high energy detonators, and the associated firing cables and accessory items. The booster charge was suspended in the center of the cavity by means of an extension rod anchored to a 1-inch-thick aluminum collar plate. The collar plate was secured in place in the access hole just above the top of the cavity by means of 3/4-inch-diameter coil-proof chains anchored to 1 × 18-inch rock bolts set in the shear keyway (refer to Figure 2.6).

In addition to the booster charge, the downhole hardware included a 1-1/2-inch-diameter aluminum fill line, a 1-inch-diameter aluminum vent line, and a 1/4-inch manometer tube. These pipes were mounted in the aluminum collar plate (described in the preceding paragraph) and extended up the access hole to termination points just above the ground surface.

2.2.3 Access Hole Stemming. After the booster assembly charge and other downhole hardware had been positioned and secured, the access hole was stemmed with a carefully designed concrete. The basic rationale used in the design of the stemming configuration was to provide, by means of concrete-rhyolite bond shear and reinforced concrete shear keyways, a shear resistance between the concrete-rhyolite interface equal to the in situ shear resistance of the rhyolite. Based on the results of dynamic punch-out tests, dynamic compressive strength tests, dynamic tensile splitting tests, and Mohr's circle analyses, it was determined that one shear keyway was required in the porphyritic felsite zone. An 8-foot high reinforced concrete shear keyway was placed in this section of the access hole as shown in Figure 2.6. In addition to matching the shear strength properties of the in situ medium, the concrete stemming material was designed to match the density, velocity, and compressibility of the in situ medium to the maximum practicable extent.

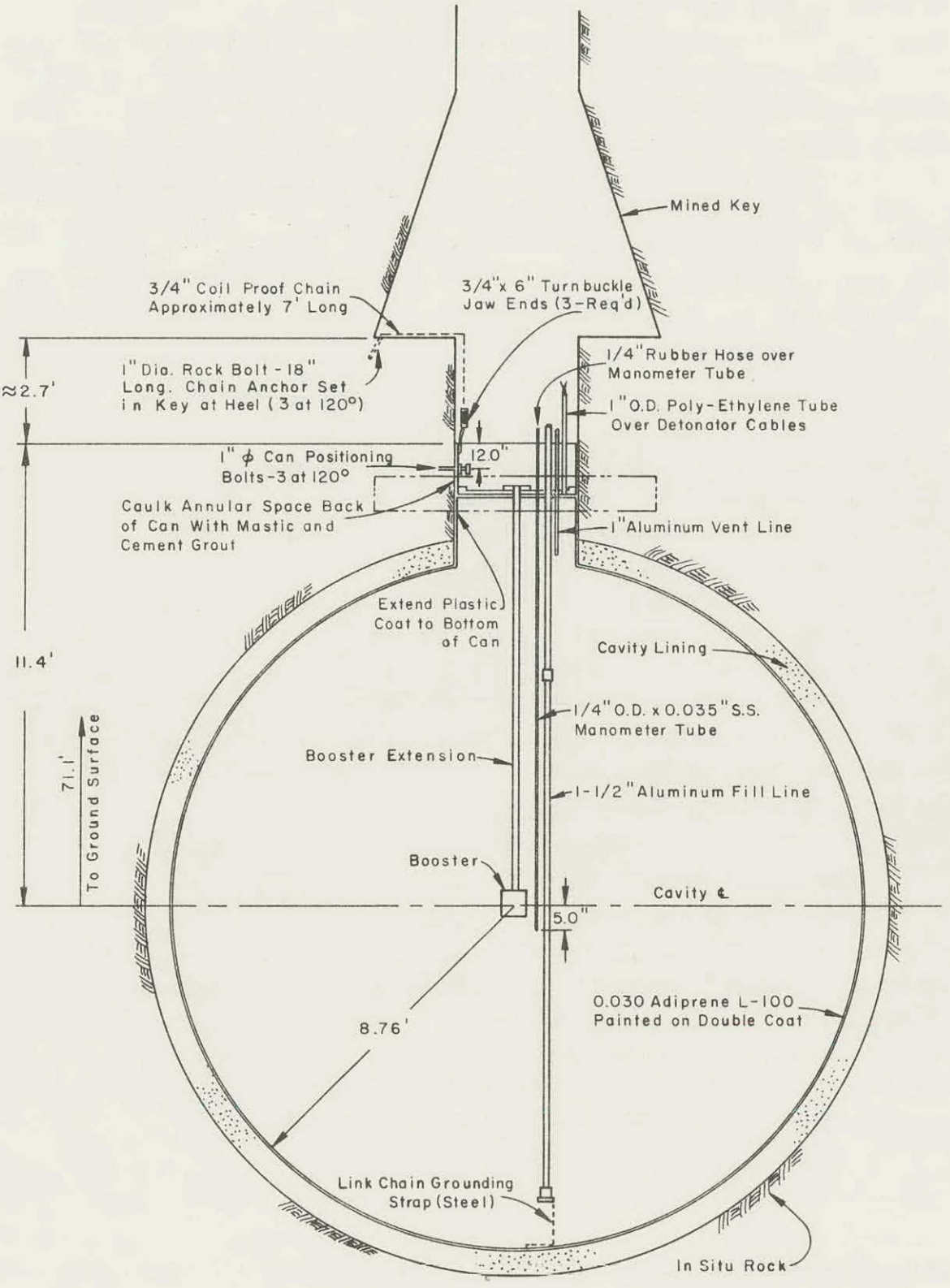

Figure 2.6 Cross Section of Pre-Schooner II Chemical Explosive Charge.

2.2.4 Nitromethane Emplacement. The nitromethane (NM) required for the experiment was shipped to the project site and stored in 55-gallon 17E drums weighing approximately 550 pounds each. At the start of fill operations on the morning of 28 September 1965 (D - 2 days), the NM was transported by explosive-handling trucks from the storage area (located approximately 4300 feet from GZ) to the GZ area. The drums were placed on a prefabricated NM transfer stand, and the liquid explosive was transferred to the cavity through a manifold system connected to the downhole 1-1/2-inch-diameter aluminum fill pipe. This technique permitted the draining of eight drums simultaneously. It had been estimated that approximately 400 drums of NM would be required to fill the cavity. At the conclusion of the first-day NM filling operations, approximately 200 drums of NM had been placed in the cavity.

Filling operations were continued starting at 0800 on 29 September 1965 (D - 1 day), and by 1100 a total of 405 NM drums had been drained into the cavity. A manometer reading taken at this time indicated that the cavity was not full, but, in fact, had a void approximately 2.9 feet in height. Since sufficient NM had been placed in the cavity to fill it, it was suspected that the cavity was leaking. Manometer readings taken over the next several hours indicated that the cavity was leaking at a loss rate of several drums per hour. Immediate action was taken to have additional NM shipped from the Nevada Test Site in time for the scheduled detonation on 30 September 1965 (D-Day) in order to make up for the deficit caused by leakage. An additional 23 drums of NM were shipped from the Nevada Test Site (NTS) and drained into the cavity. This final emplacement operation was completed at 1545 on 30 September 1965. The manometer reading taken at this time indicated that a void of approximately 4.15 feet in height existed in the charge cavity.

2.3 DESCRIPTION OF DETONATION

Since a survey of available supply sources of NM indicated that it would take a minimum of several weeks to ship a sufficient quantity to the site to refill the cavity, the Technical Director decided to execute Pre-Schooner II on the scheduled date with an explosive charge less than the design charge weight of 100 tons. Pre-Schooner II was detonated on 30 September 1965 at 1709 MST. Based on observed leakage rates and the manometer reading taken at 1545, it is estimated that at the time of detonation approximately 85.5 tons of NM were in the cavity.

A preshot examination of the Pre-Schooner II explosive cavity by NCG geologists indicated that the cavity walls were highly jointed but that the joint planes were tight and that a few were healed with calcite. Sections of the southwestern wall of the cavity were characterized by friable felsite which was permeated by tiny irregular hairline fractures. Many of these fractures were healed by calcite, the remainder were tight. Since laboratory tests have shown that NM will not propagate in a geometry with a cross

section of less than about 3/4 inch, it is believed that the NM which leaked out of the cavity did not detonate and contribute to the cratering phenomena.

The following are pertinent characteristics of the Pre-Schooner II explosive charge at time of detonation:

Estimated Weight of NM in Cavity at Shot Time	171,000 lbs (85.5 tons)
Percent of Cavity Volume Filled	85.5
Height of Spherical Segment Above Partially Filled Sphere	4.2 ft.
Energy Equivalent Yield[1]	94.6 tons (0.0946 kt)
Scaled Depth of Burst	142 ft/kt$^{1/3.4}$

[1]Based on assumption that an energy equivalent yield of 1 ton releases 10^9 cal and that NM releases 1220 cal/gm of charge weight.

REFERENCES

1. J. L. Decell, F. E. Girucky, R. W. Hunt, and R. J. Lutton; "Selection and Preshot Inventigation of Pre-Schooner II Test Site"; U. S. Army Engineer Waterways Experiment Station, July 1965.

2. "Compilation of Geologic and Engineering Properties Investigations"; U. S. Army Engineer Nuclear Cratering Group, September 1965.

3. R. Paul; "Geologic Examination of the Access Shaft and Explosive Cavity for Pre-Schooner II"; NCG/TM 65-4, November 1965; U. S. Army Engineer Nuclear Cratering Group, Livermore, California.

4. R. T. Stearns; "Seismic Uphole Survey, Pre-Schooner II, Idaho"; LRL Internal Memorandum, July 1965; Lawrence Radiation Laboratory, Livermore, California.

5. "Technical Director' s Operation Plan for Project Pre-Schooner II"; NCG, September 1965; U. S. Army Engineer Nuclear Cratering Group, Livermore, California.

CHAPTER 3

CRATER MEASUREMENTS STUDIES

3.1 INTRODUCTION

3.1.1 Objectives. The objectives of the Pre-Schooner II crater measurements studies program were: (1) to determine the size and shape of the crater produced by the detonation and (2) to ascertain the maximum range of missiles resulting from the detonation.

3.1.2 Background. Previous experiments in hard, dry rock showed considerable variation in crater dimensions as a function of depth of burst and yield. The results of Project Pre-Schooner II were to reduce the uncertainties in apparent crater dimensions and to serve as a correlation shot for the Schooner event (see Reference 1).

3.1.3 Comparison of Craters in Alluvium and Basalt (References 2, 3, and 4).

Figure 3.1 shows the H. E. cratering curves for alluvium and basalt scaled to 1 kt using a yield scaling power of 1/3.4. Both the apparent crater radius and depth are shown. As expected, the basalt craters are smaller than craters in alluvium made by equal yields detonated at identical depths of burst.

The data from 44 H. E. shots with charge weights of 256 pounds (33 shots), 2560 pounds (6 shots), 40,000 pounds (3 shots), and 1,000,000 pounds (1 shot) were used to determine the cratering curves for alluvium. Data from 17 H. E. shots with charge weights of 1000 pounds (10 shots) and 40,000 pounds (7 shots) were used to determine the cratering curves for basalt. The 1000-pound data were weighted about 1/40 of the 40,000-pound data.

For basalt, at depths of burst greater than optimum, the curves reduce to zero more rapidly than those for alluvium. This results from "bulking" or increase in volume of the loose rock in comparison with its original in-place volume. Since at depths of burst greater than optimum proportionately less material is ejected, the bulking of basalt fills the true crater more rapidly than would alluvium material. Experience indicates that bulking for the basalt of Buckboard Mesa results in a percentage increase in original volume of about 25 to 65 percent. NTS desert alluvium shows almost no evidence of bulking.

3.2 EXPERIMENTAL PROCEDURES

3.2.1 Aerial Stereophotogrammetric Mapping. Preshot and postshot topographic maps were prepared from aerial stereophotographs by the Aerial Mapping Company of Boise, Idaho. A K&E camera with a 6-inch focal length and a 9 × 9-inch format was

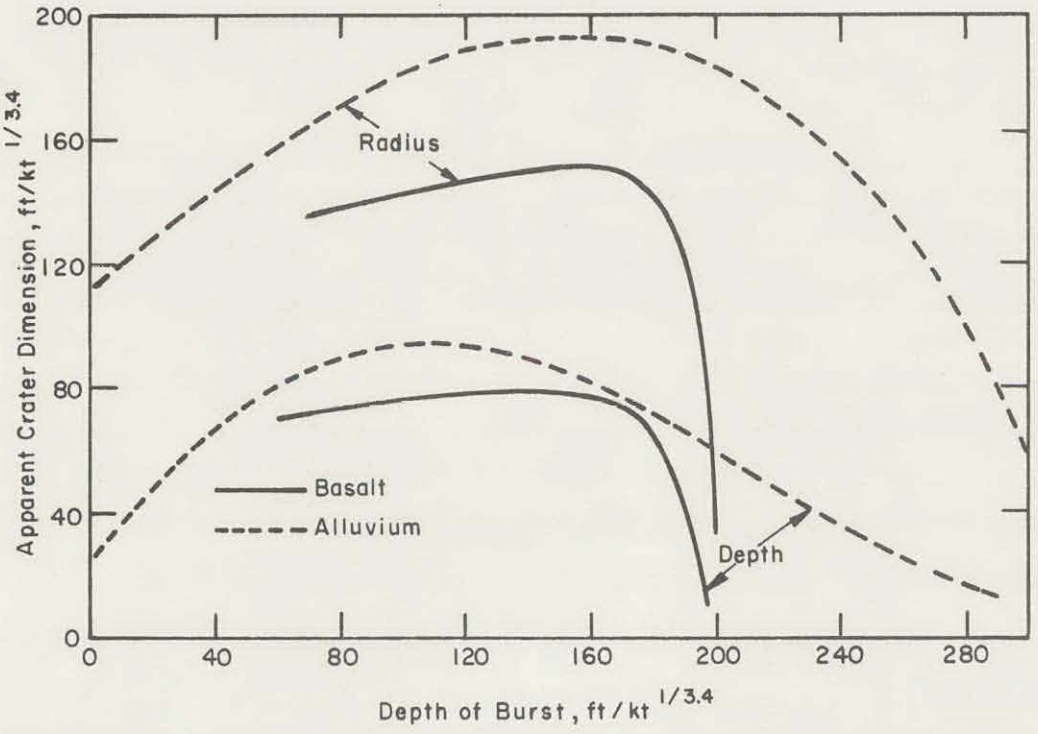

Figure 3.1 Cratering Curves.

used. Flight altitude was 600 feet above the ground resulting in a negative scale of 1 inch equals 100 feet. An area 1200 feet square was mapped. Figure 3.2 and 3.3 show the preshot and postshot aerial photography. Figures 3.4 and 2.5 show the preshot and postshot topographic map centered on Surface Ground Zero (SGZ).

3.2.2 Determination of Apparent Crater Dimensions and Maximum Missile Range (Reference 5).

a. Average Apparent Crater Radius, R_a. The average apparent crater radius was determined by: (1) establishing the line of intersection of the apparent crater with the preshot ground surface using the preshot and postshot topographic maps, (2) measuring the area within the line of intersection, and (3) computing the radius of a circle with the same area. (Figure 3.6 shows the crater nomenclature and notation used in this report.)

b. Apparent Crater Depth, D_a. The apparent crater depth was determined by measuring the distance from the deepest point of the crater to the

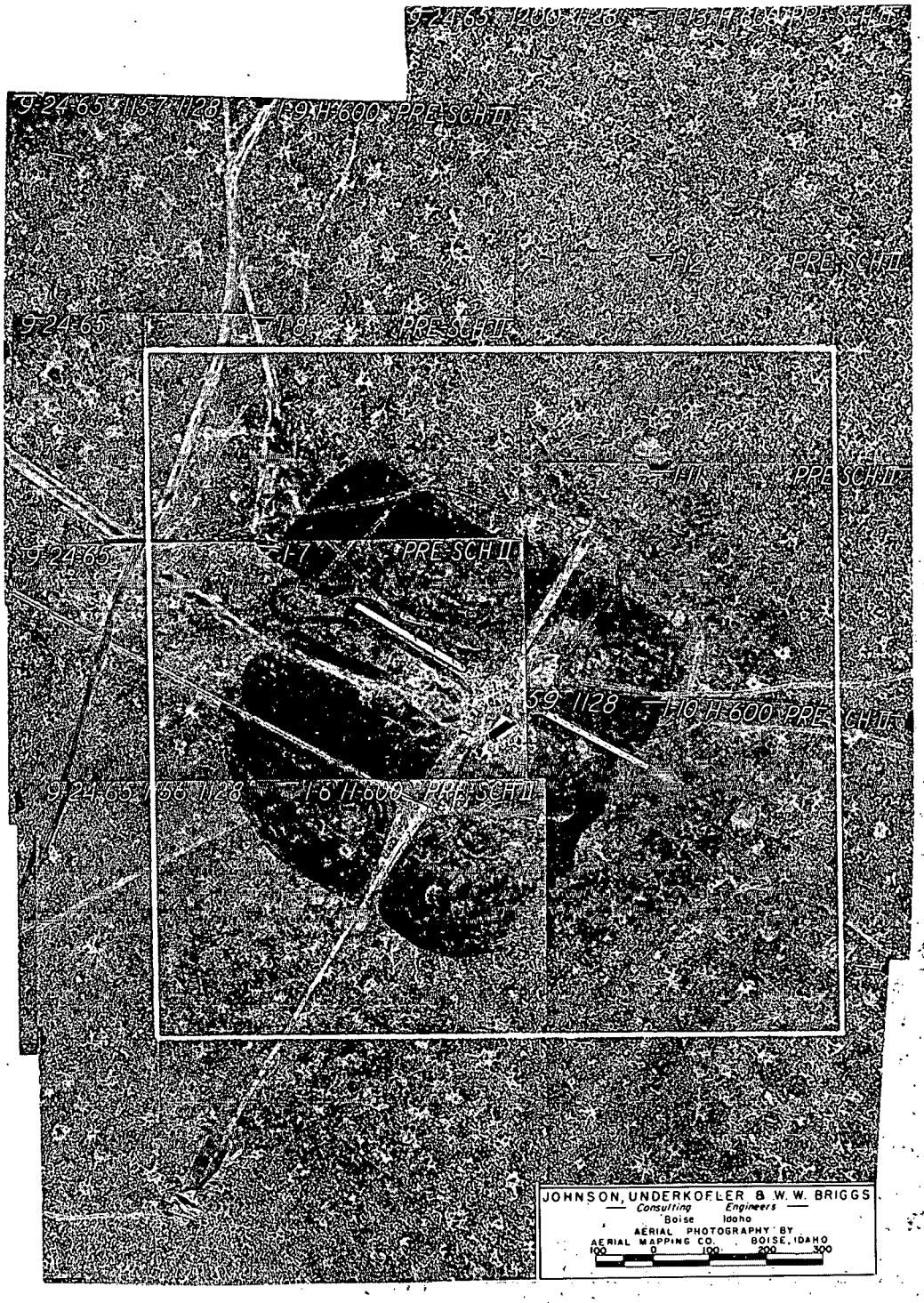

Figure 3.2 Pre-Schooner II Preshot Aerial Photography.

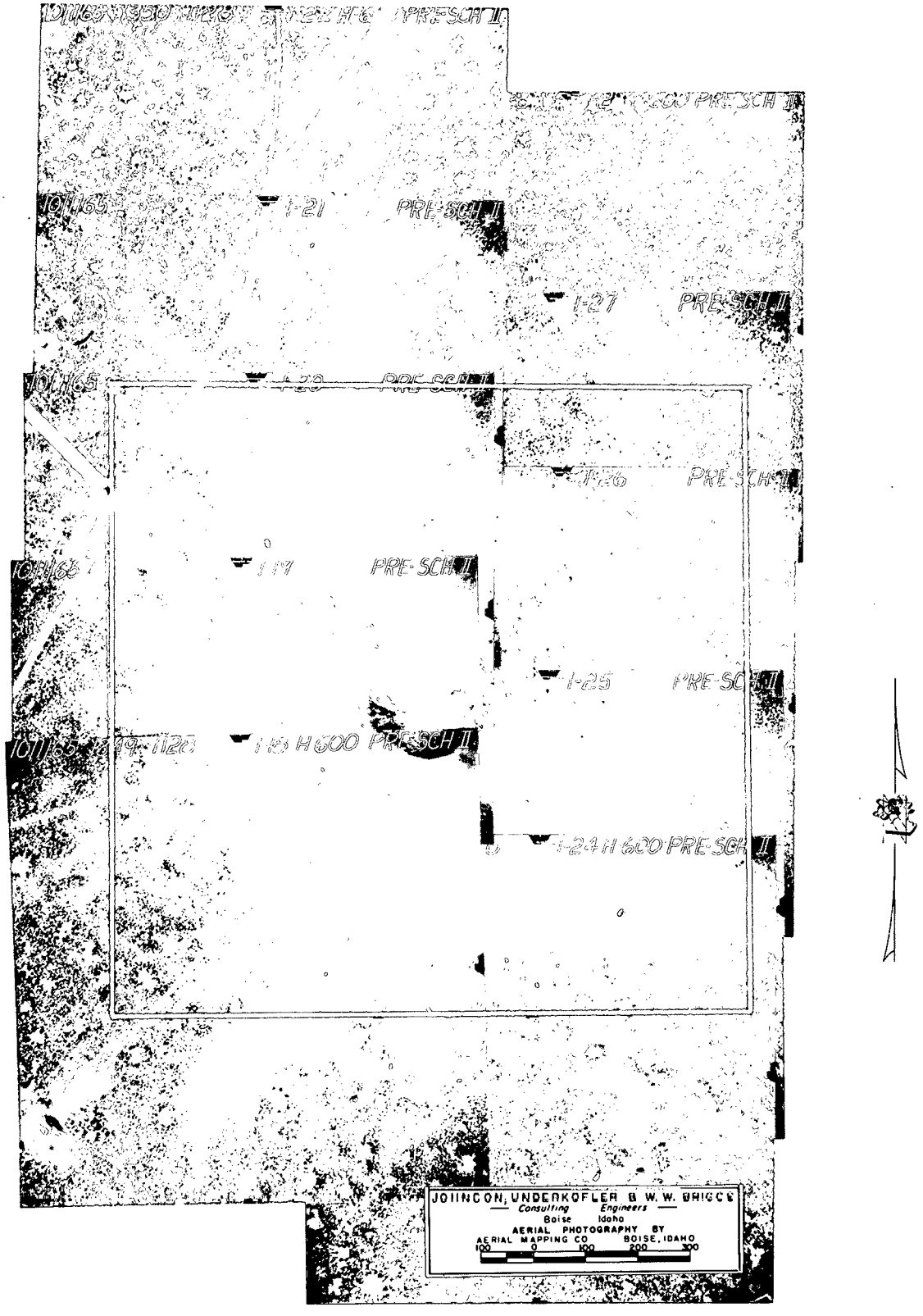

Figure 3.3 Prc-Schooner II Postshot Aerial Photography.

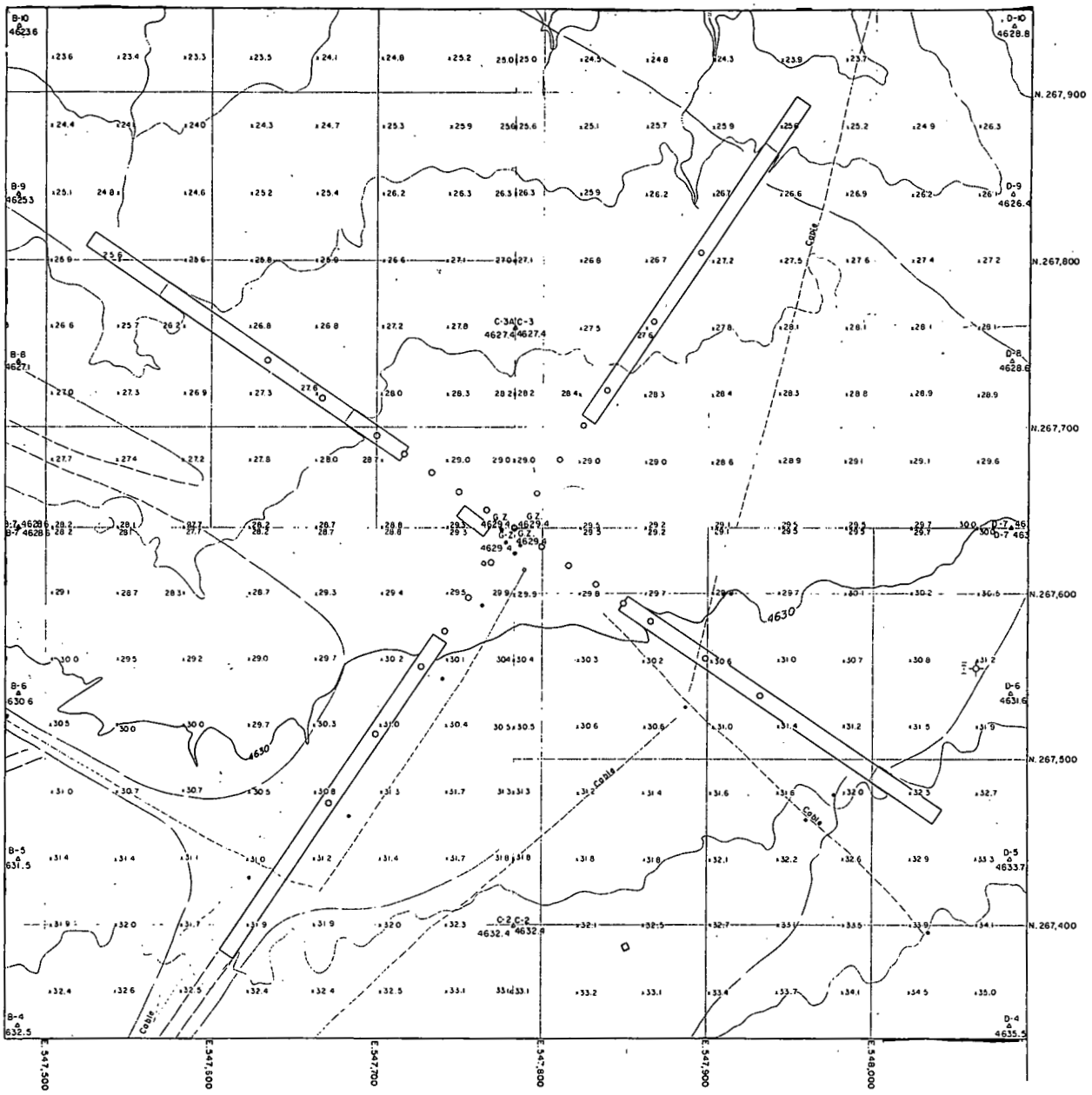

Figure 3.4 Pre-Schooner II Preshot Topographic Map.

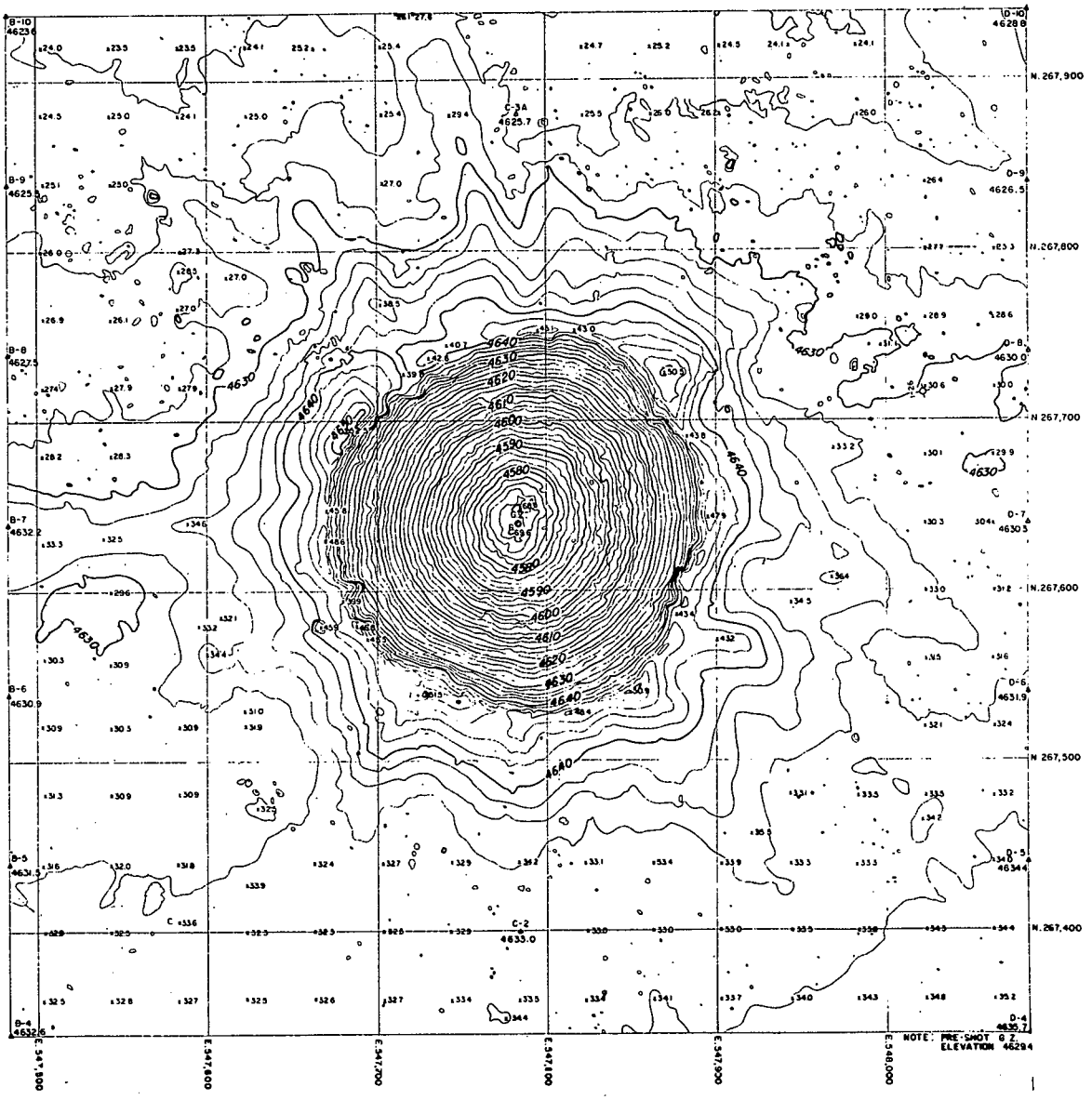

Figure 3.5 Pre-Schooner II Postshot Topographic Map.

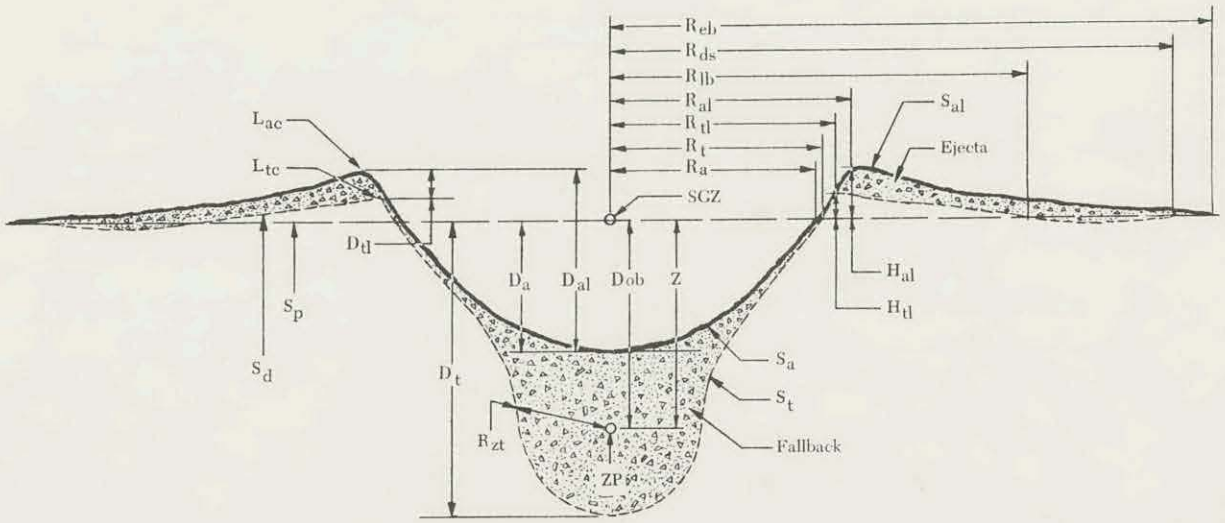

D_a . . . Maximum depth of apparent crater below preshot ground surface measured normal to the preshot ground surface.*

D_{al} . . . Depth of apparent crater below average apparent crater lip crest elevation.

Dob . . Normal depth of burst (measured normal to preshot ground surface).

D_t . . . Maximum depth of true crater below preshot ground surface.

D_{tl} . . . Depth of true crater lip crest below apparent crater lip crest.

Ejecta . Material above and or beyond the true crater and includes: (1) foldback; (2) breccia—ballastic trajectory; (3) dust—aerosol transport; etc.

Fallback. Material fallen inside the true crater and includes: (1) slide blocks; (2) breccia and stratified fallback —ballastic trajectory; (3) dust—aerosol transport; (4) talus; etc.

H_{al} . . . Apparent crater lip crest height above preshot ground surface.

H_{tl} . . . True crater lip crest height above preshot ground surface.

L_{ac} . . . Apparent crater lip crest.

L_{tc} . . . True crater lip crest.

R_a . . . Radius of apparent crater measured on the preshot ground surface.

Note: The radius measurements pertain only to single charge craters and represent average dimensions. If crater shape deviates substantially from circular, the direction of measurement must be specified. An average radius value can also be determined by dividing the plan area by π and taking the square root.

R_{al} . . . Radius of apparent lip crest to center.

R_{ds} . . . Outer radius of displaced surface.

R_{eb} . . . Radius of outer boundary of continuous ejecta.

R_{lb} . . . Outer radius of true lip boundary.

R_t . . . Radius of true crater measured on the preshot ground surface.

R_{tl} . . . Radius of true lip crest to center.

R_{zt} . . . Distance between the zero point and the true crater surface measured in any specified direction. When measured in a direction below the zero point is equivalent to lower cavity radius.

S_a . . . Apparent crater surface, e.g. rock-air or rubble-air interface.

S_{al} . . . Apparent lip surface.

SGZ . . Surface ground zero.

S_d . . . Displaced ground surface.

S_p . . . Preshot ground surface.

S_t . . . . True crater surface, e.g. rock-air or rock rubble interface.

V_a . . . Volume of apparent crater below preshot ground surface.

V_{al} . . . Volume of apparent crater below apparent lip crest.

V_t . . . Volume of true crater below preshot ground surface.

V_{tl} . . . Volume of true crater below true crater lip crest.

Z . . . . Vertical depth of burst (equivalent to Dob when crater is formed on a horizontal surface).

ZP . . . Zero Point—effective center of explosion energy.

Note: The following definitions apply to linear craters only. Linear crater refers to the excavation formed by overlapping crater effects resulting from a row of charges. All above terms applicable to single craters apply also to linear craters with the exception of the radius terms which are replaced by the width terms below.

W_a . . . Width of apparent linear crater measured on the preshot ground surface.

W_{al} . . Width of apparent lip crest measured across linear crater.

W_{ds} . . Width of displaced surface measured across linear crater.

W_{eb} . . Width of outer boundary of continuous ejecta measured across linear crater.

W_{lb} . . Width of true crater outer lip boundary measured across linear crater.

W_t . . . Width of true linear crater measured on the preshot ground surface.

W_{tl} . . . Width of true linear crater lip crest measured across crater.

*All distances, unless specified otherwise, are measured parallel or perpendicular to preshot ground surface.

Figure 3.6 Crater Nomenclature.

preshot ground surface along a line perpendicular to the preshot ground surface using the topographic maps.

c. Apparent Crater Volume, V_a. The apparent crater volume was determined by computing the volume bounded by the preshot ground surface and the surface of the apparent crater using an end area method applied to horizontal sections taken at 2-foot contour intervals.

d. Average Lip Crest Height, H_{al}. The average lip crest height was determined by: (1) outlining the lip crest on the postshot topographic map, (2) plotting the lip crest profile, (3) plotting the profile of the preshot ground surface directly beneath the lip crest outline, and (4) calculating the average lip height using a planimeter.

e. Average lip Crest Radius, R_{al}. The average lip crest radius was determined by: (1) measuring the area within the lip crest outline, and (2) computing the radius of a circle with the same area. This radius is the average lip crest radius.

f. Average Apparent Crater Profile. The average apparent crater profile was determined by: (1) computing the average radius of each contour below preshot ground surface, and (2) plotting the contour elevation versus the average radius.

g. Maximum Missile Range. The maximum missile range was determined by: (1) locating the most distant missiles along approximately 110 radials from GZ using normal field survey techniques, (2) plotting these missile locations on the postshot topographic map, and (3) measuring the distance from the furthest missile to SGZ. This distance is defined as the maximum missile range.

3.3 RESULTS

The apparent crater measurements and maximum missile range resulting from the detonation, as determined by the procedures outlined in Section 3.2, are given in Table 3.1 together with predictions based on scaling relationships (exponent of 1/3.4 and Buckboard Mesa basalt cratering data) and PUSH code calculations.

3.4 ANALYSIS AND INTERPRETATION

3.4.1 Apparent Crater Measurements. To compare the apparent crater measurement results of Pre-Schooner II to previous TNT and nuclear detonations, an energy equivalence relationship is used based on the assumptions that an energy equivalent yield of 1 ton releases 10^9 cal, 1 gm of TNT releases 1090 cal, and 1 gm of NM releases 1220 cal. The energy equivalent yield of the Pre-Schooner II detonation

TABLE 3.1 CRATER MEASUREMENTS

Measurement	Actual Measurement	Predicted Measurements	
		1/3.4 Scaling (Ref. 1)	PUSH code (Ref. 6)
	ft	ft	ft
Apparent Crater Radius, R_a	95.2	76±9	89
Apparent Crater Depth, D_a	60.7	41±5	62
Apparent Crater Volume, V_a	24,780[a]	--	--
Average Lip Crest Height, H_{al}	17.2	15±2	16.5
Average Lip Crest Radius, R_{al}	114	--	--
Maximum Missile Range	2,320	3100	--

[a]Cubic yards.

(charge weight of 85.5 tons of NM), therefore, is 94.6 tons (0.0946 kt). Table 3.2 shows the scaled values of depth of burst, apparent crater radius, and apparent crater depth for Pre-Schooner II.

TABLE 3.2 PRE-SCHOONER II SCALED APPARENT CRATER DIMENSIONS

Item	Dimension			
	ft	m	$ft/kt^{1/3.4}$	$m/kt^{1/3.4}$
Depth of Burst	71.1	21.67	142.2	43.34
Apparent Crater Radius	95.2	29.02	190.4	58.04
Apparent Crater Depth	60.7	18.50	121.4	37.00

Figures 3.7 and 3.8 show that the apparent crater dimensions (radius and depth) of the Pre-Schooner II crater were considerably larger than one would predict using a

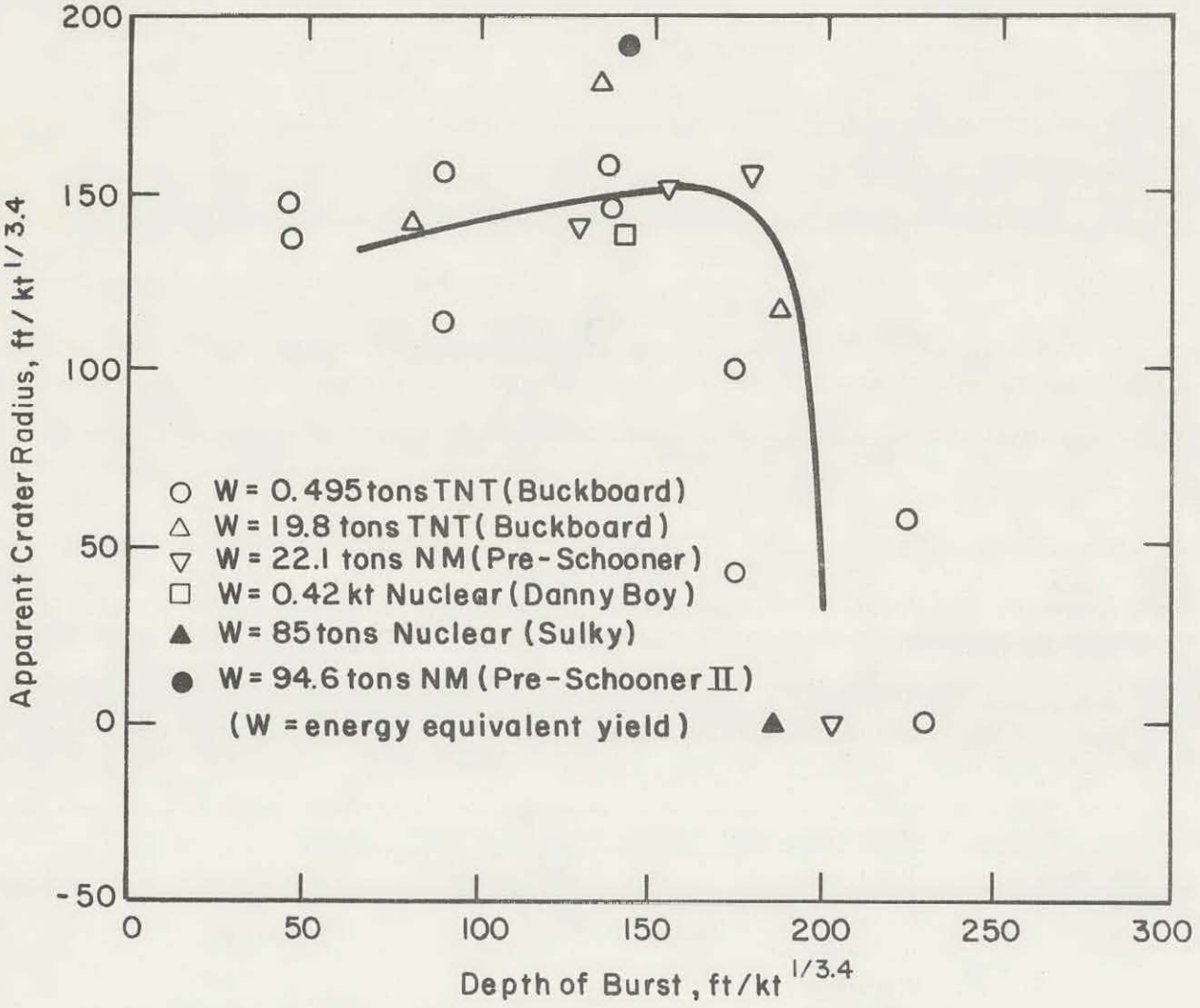

Figure 3.7 Apparent Crater Radius vs. Depth of Burst in Hard Rock.

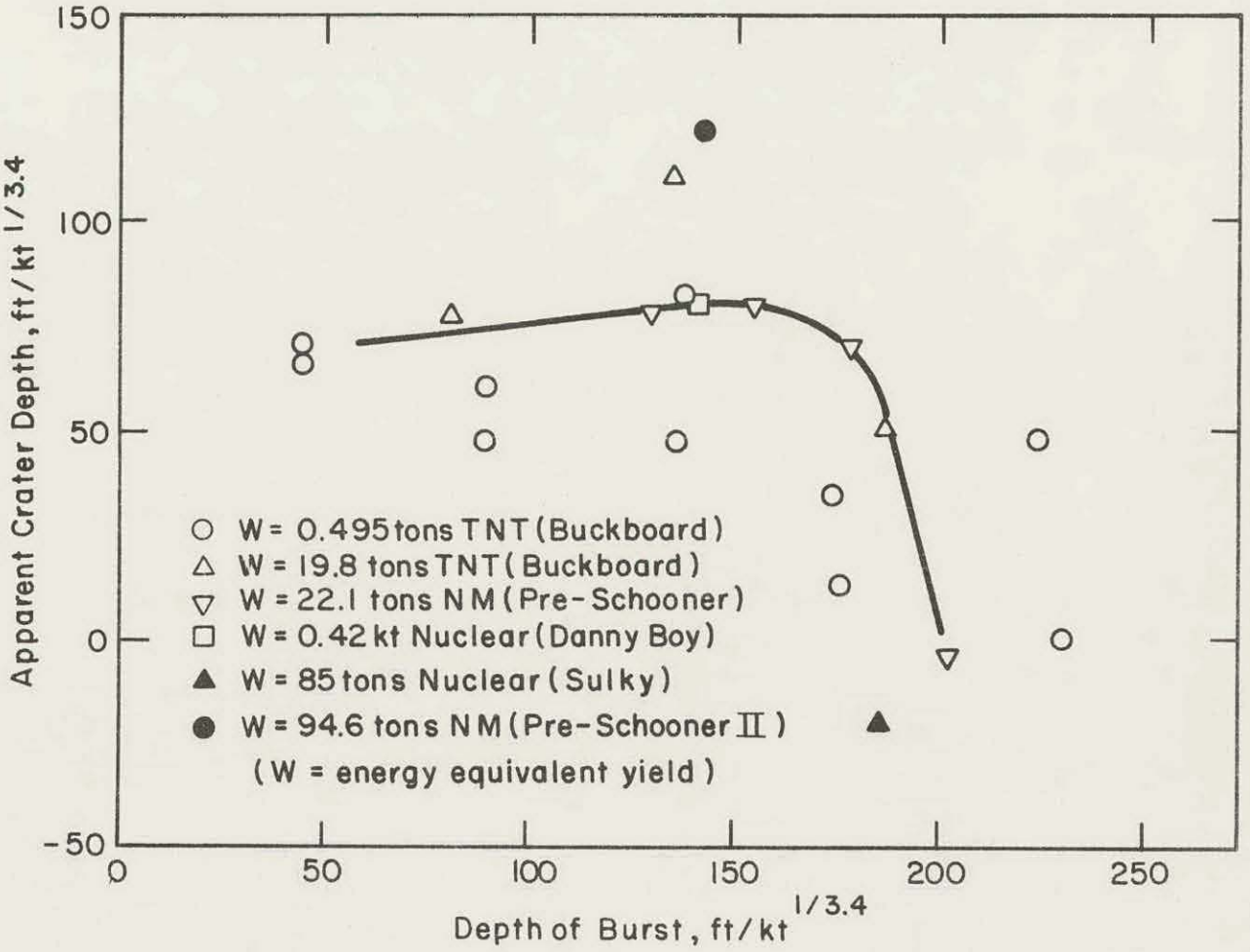

Figure 3.8 Apparent Crater Depth vs. Depth of Burst in Hard Rock.

scaling exponent of 1/3.4 and the results of previous detonations in the basaltic hard rock of Buckboard Mesa.

Figure 3.9 shows two profiles through the Pre-Schooner II and Danny Boy craters. It is of interest to note that the 94-ton Pre-Schooner II detonation in rhyolite produced a crater of approximately the same dimensions as that produced by the Danny Boy 420-ton nuclear detonation in basalt. An examination of the Pre-Schooner II crater

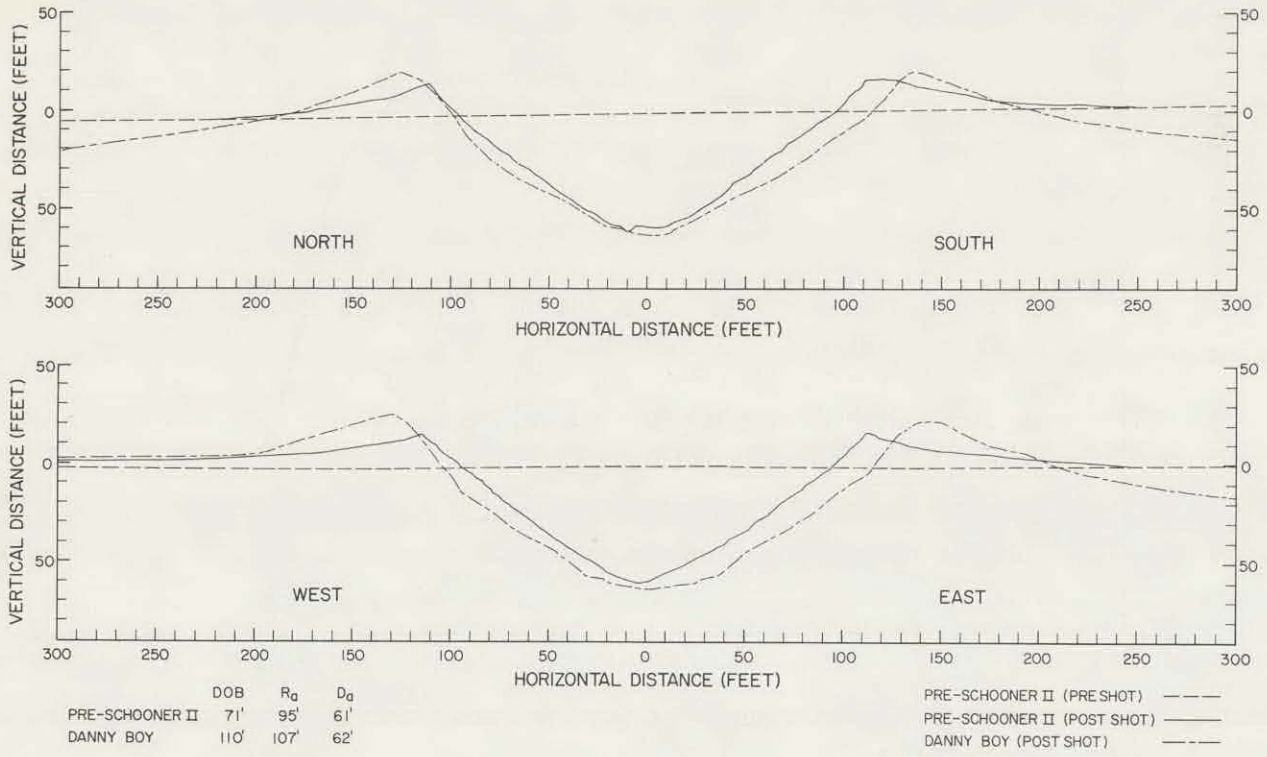

Figure 3.9 Pre-Schooner II and Danny Boy Crater Profiles.

indicates that the average size of the fallback and ejecta material is considerably smaller than that resulting from the detonations in basalt. This fact, in turn, would lead one to surmise that the bulking of the Pre-Schooner II material was less than the Buckboard Mesa basalt. The difference in bulking characteristics and the fact that the Pre-Schooner II material was more fractured and jointed and had a generally lower compressive strength than the Buckboard Mesa basalt account, in large measure, for the difference in cratering characteristics of the two media (Reference 7).

3.4.2 Apparent Crater Geometry. Figure 3.10 shows the average apparent crater profile for Pre-Schooner II. For comparison, the profile for a cone, a parabola, and a hyperbola are also shown on the figure. These geometric shapes were plotted

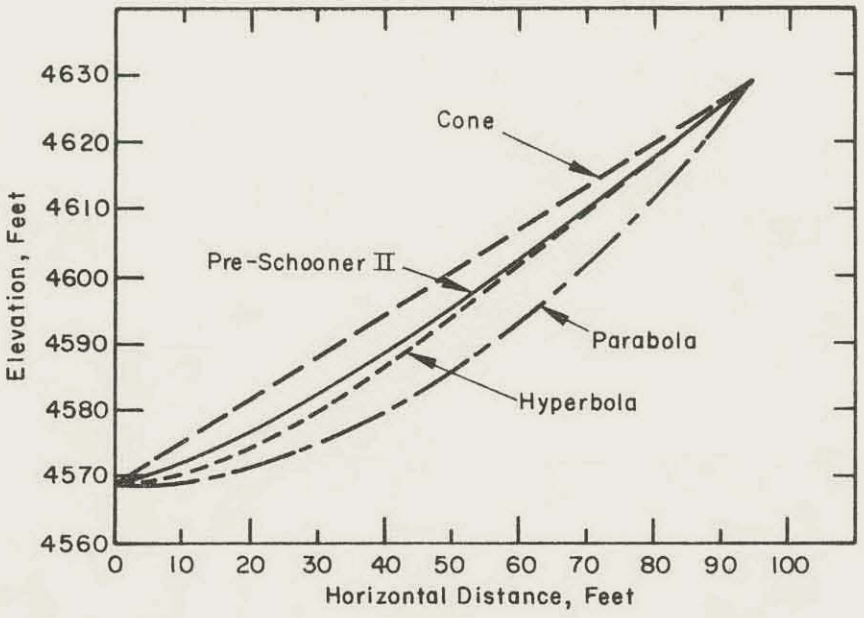

Figure 3.10 Pre-Schooner II Average Apparent Crater Profile.

with the restriction that they pass through the points R_a and D_a for the Pre-Schooner II crater. Since a third condition is required in order to plot only one hyperbola through any two given points, the slope of the hyperbola was made equal to the slope of the Pre-Schooner II average apparent crater profile at the preshot ground surface elevation. This constraining condition was selected on the basis of a recent analysis of the apparent crater profiles of twenty craters in alluvium and basalt (Reference 8). Figure 3.10 clearly indicates that the Pre-Schooner II average apparent crater profile is approximately hyperbolic.

3.4.3 Maximum Missile Range. Figure 3.11 shows the curves used to predict the maximum missile ranges of H.E. detonations (Reference 3). The maximum missile range of 2320 feet for Pre-Schooner II lies between the values of 2800 and 1780 feet for

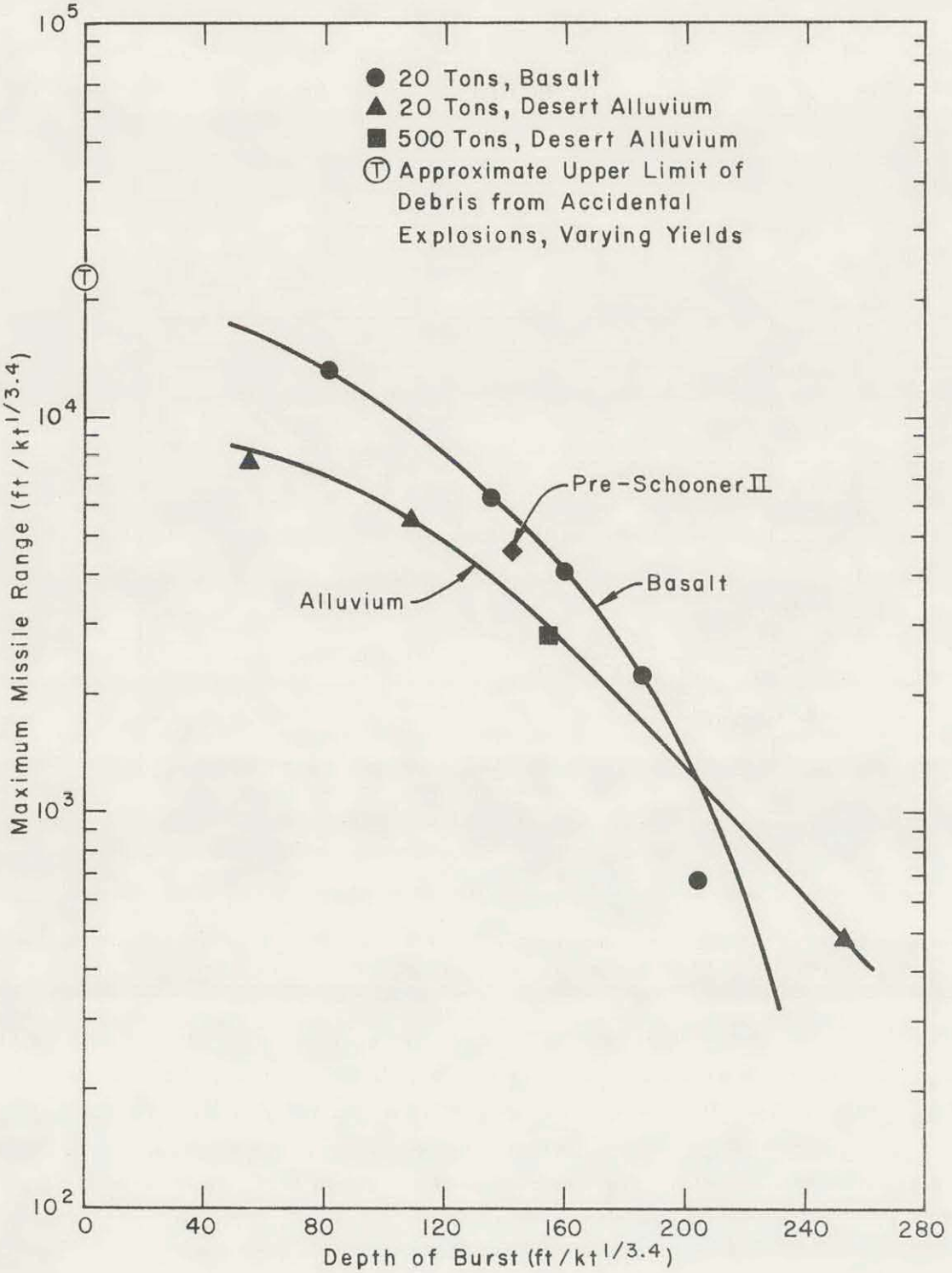

Figure 3.11 Maximum Missile Ranges in Basalt and Alluvium.

basalt and alluvium, respectively (for the same yield and depth of burst). The presence of vitrophyre breccia (6-inch-minus vitrophyre fragments in a porous orange matrix of glass shards) to a depth of 20 to 25 feet in the vicinity of SGZ may account for the difference between the maximum missile ranges for basalt and Pre-Schooner II.

3.5 CONCLUSIONS

The Pre-Schooner II detonation produced an apparent crater 27-1/2 percent wider and 53 percent deeper than that which would be predicted by the current basalt cratering curves (1/3.4 scaling exponent and a yield of 94.6 equivalent tons). This size is attributed, in large measure, to differences in bulking, fracture and joint patterns, and compressive strengths of the Pre-Schooner II rhyolite and Buckboard Mesa basalt.

The shape of the average apparent crater profile for Pre-Schooner II is approximately hyperbolic.

REFERENCES

1. "Technical Director's Operational Plan for Project Pre-Schooner II"; NCG, September 1965; U. S. Army Nuclear Cratering Group, Livermore, California.

2. M. D. Nordyke; "On Cratering, A Brief History, Analysis, and Theory of Cratering"; UCRL 6578, August 1961; Lawrence Radiation Laboratory, Livermore, California.

3. "Military Engineering with Nuclear Explosives (Coordination Draft)"; NCG, November 1964; U. S. Army Engineer Nuclear Cratering Group, Livermore, California.

4. M. D. Nordyke, et al; "Project Dugout Technical Director's Summary Report"; PNE-600F, June 1964; Lawrence Radiation Laboratory, Livermore, California.

5. F. Videon and J. Toman; "Single Charge Crater Measurements"; UOPKC 64-64, December 1964; U. S. Army Engineer Nuclear Cratering Group, Livermore, California.

6. R. Terhune; "PUSH V in Basalt and Pre-Schooner II Crater Predictions"; UOPKA 65-19, September 1965; Lawrence Radiation Laboratory, Livermore, California.

7. B. C. Hughes; "A Report of the Scope and Preliminary Results of Project Pre-Schooner II"; NCG rpt, November 1965; U. S. Army Engineer Nuclear Cratering Group, Livermore, California.

8. B. C. Hughes, R. H. Benfer, F. H. Foster; "Study of the Shape and Slope of Explosion-Produced Craters"; NCG/TM 65-8, November 1965; U. S. Army Engineer Cratering Group, Livermore, California.

CHAPTER 4

SURFACE MOTION STUDIES

4.1 INTRODUCTION

Detailed description of the ground surface motion resulting from a cratering detonation is desired as general diagnostic information concerning cratering physics. Surface motion measurements for the Scooter event (Reference 1) led to the development of a simple-two dimensional model of cratering for single-charge H. E. events in alluvium (References 2 and 3). Essentially the same model has been applied with varying success to the study of crater dimensions and surface motion for H. E. and N. E. events in hard, competent, chemically inert rock media.

The objectives of the Pre-Schooner II Surface Motion Studies Program were:

a. To provide surface motion observations for input into the theoretical cratering calculations program.

b. To aid in predicting the crater dimensions and surface motion of the planned Schooner 100-kt nuclear event.

To accomplish these objectives, the scope of the program included consideration of the following aspects of surface motion and crater formation:

a. Characteristic times such as the times of the onset of spall, peak spall velocity, onset of gas acceleration, and venting.

b. Variation of peak spall velocity with preshot distances of ground surface positions from the shot point.

c. Mound shape and size prior to venting.

d. Relative contributions to cratering by spall and gas acceleration as evidenced by the time histories of ground surface velocities.

A necessary subsidiary objective of the surface motion study effort was to evaluate the surface motion measurement and data analysis techniques. Recently, new techniques of data analysis have been developed to facilitate the handling of the large amount of data required for an adequate surface motion study (Reference 4).

4.2 EXPERIMENTAL PROCEDURES

The basic technique used to study the ground surface motion resulting from the Pre-Schooner II detonation consisted of:

a. Recording the surface motion by high-speed photography using carefully designed targets.

b. Analyzing the high-speed photography films by means of data processing techniques to determine displacement, velocity, and acceleration histories.

For Pre-Schooner II, two somewhat different experimental procedures were used to document the surface motion. These procedures, referred to as the falling-mass experiment and the surface target array experiment, are described in detail in the following paragraphs.

4.2.1 Falling-Mass Experiment. The falling-mass experiment was designed to determine accurately the motion of the surface GZ area at early times ($t < 150$ msec.). To accomplish this objective, Camera 7FTX (Table 4.1) was located in Camera Station No. 1, 1125 feet SW of GZ, to record the motion of a 16-× 4-foot graduated plywood

TABLE 4.1 SURFACE MOTION CAMERA CHARACTERISTICS

Camera No.	Type of Surface Motion Study	Nominal Speed	Type of Film	Field of View	
				Hor.	Vert.
		frames/sec		ft	ft
Camera Station No. 1 (1125 ft SW of GZ):					
773 PS	Visual Target	1000	MS Color	468	333
5 HSE	Visual Target	1000	MS Color	405	315
7 FTX	Falling Mass	4000	Bl & Wh	66.6	44.3
Camera Station No. 2 (3382 ft NW of GZ):					
717 PS1	Flare Target	1000	LSB	703	500
10 HSE	Flare Target	1000	LSB	487	375
22 HSE	Flare Target	3000	LSB	487	375
775 PS2	Visual Target	1000	MS Color	703	500
770 PS3	Visual Target	1000	MS Color	703	500

target mounted on a 6-inch O. D. pipe. The pipe which supported the target was emplaced in concrete to a depth of 5 feet at a location 7.1 feet west of GZ (Figure 4. 1). The plywood target was graduated with alternating black and white lines, 6 inches wide. A bowling ball, painted red, was suspended at the top of the target and released at the time of the detonation of the Pre-Schooner II event by means of a detonator inserted in

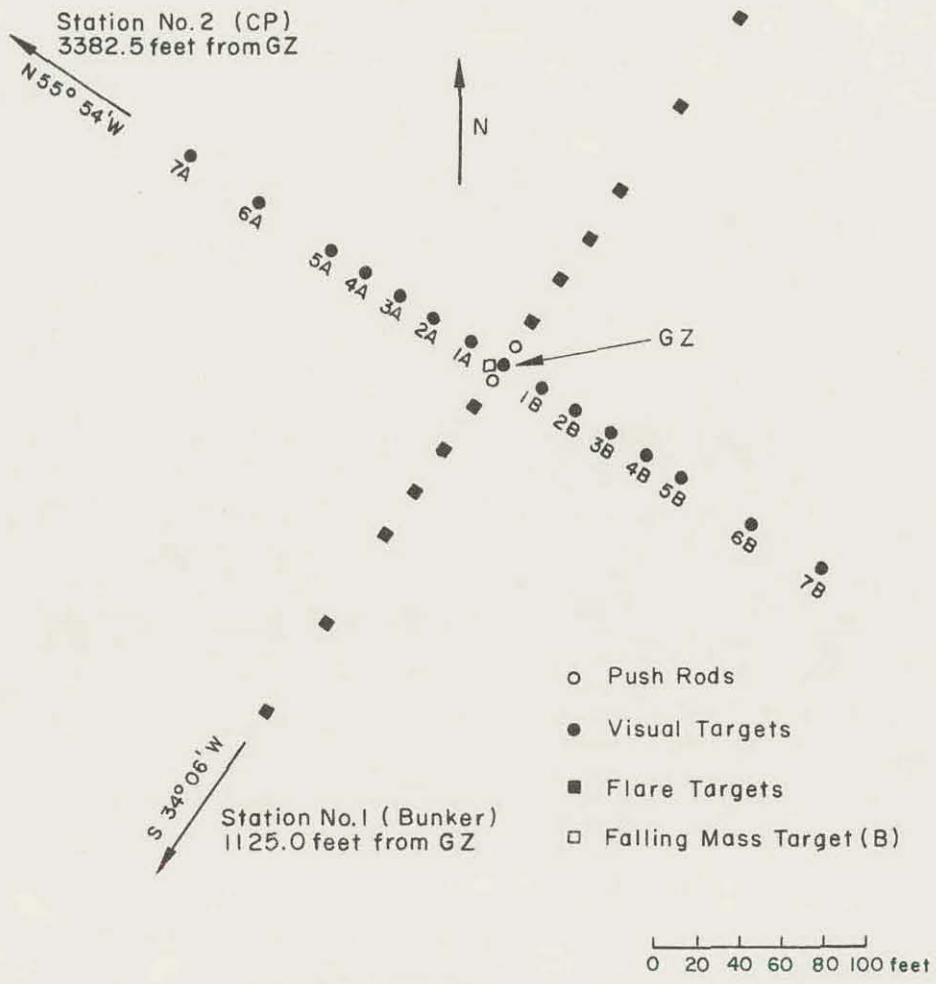

Figure 4. 1 Target Array.

the cord supporting the ball. The bowling ball served as a fixed reference point (in a free-fall accelerating cartesian coordinate system) for measurement of the displacement of the plywood target which moved with the rising ground surface.

The field of view of the falling-mass experiment camera (Table 4.1) was sufficiently wide to permit the detailed study of the early motion of the visual surface targets located 20 feet on either side of GZ.

4.2.2 Surface Target Array Experiment. In order to obtain detailed documentation of the surface motion over the entire mound produced by the Pre-Schooner II detonation, visual surface and flare surface targets were placed as shown in Figure 4.1. It was planned to record the displacement of these targets with high-speed motion picture cameras. The location and characteristics of these cameras are given in Table 4.1. Zero time was established for the cameras by an array of flash bulbs at GZ which were activated by a "zero fiducial" signal furnished by the fire control unit.

The visual surface targets consisted of 3-foot square red and white plywood panels mounted on 6-inch O.D. pipes which were emplaced in concrete to depths not less than 3 feet. The plywood panel for the GZ visual surface target was centered 4 feet above the ground surface. The panel centers of all the other visual targets were fixed at this same elevation.

The flare surface targets consisted of baritol flares contained in aluminum flare pots mounted on 6-inch O.D. pipes similar to those used to support the visual surface targets. The flares were designed to have a luminous intensity of 500,000 candle power.

4.2.3 Data Analysis. A microscopic digitizer was used to facilitate analysis of the surface motion films. The following procedure was used:

a. The film was placed on a platform under a microscope, and the platform was moved manually by means of vernier screws until a target was positioned under cross-hairs. By depressing a foot pedal, the film position coordinates were automatically punched on an IBM card. The accuracy of this method was found to be superior to that of either the Eyeball Flare Reading Technique or the Oscar Technique (Reference 5).

b. The raw digitized data were used as input to a 7094 computer code. The computer accomplished a coordinate transformation, independently smoothed the data positions, and computed the velocity and acceleration components of each target as a function of time (Reference 4).

In the falling-mass experiment, the reference coordinate system used from frame to frame was determined by a line parallel to the film edge passing through the center of the ball.

In the surface target array experiment, targets 7A and 7B (Figure 4.1) were used as position reference fiducials because no suitable reference points farther from

GZ were available. These targets moved during the crater formation period; therefore, some assumptions were required in order to justify their use as reference points. These assumptions are discussed in Section 4.4.2b.

4.3 PREDICTED RESULTS

Predictions of critical features of the surface motion resulting from the Pre-Schooner II detonation are summarized in Table 4.2. All predictions were based on the Pre-Schooner II design charge weight of 100 tons of nitromethane.

The SOC computer calculations were based on physical properties of the Pre-Schooner II medium as determined from laboratory testing of small core samples (Reference 6). The SOC calculations predicted that there would be no elastic precursor and that the peak spall velocity at GZ would be reached at about 1.3 msec after the onset of spall at GZ.

TABLE 4.2 PRE-SCHOONER II GZ SURFACE MOTION PREDICTIONS

Method of Calculation	V_s	V_{vl}	V_v	t_s	t_{sp}	t_g	t_{vl}	t_v
	ft/sec	ft/sec	ft/sec	msec	msec	msec	msec	msec
SOC code (Ref. 6)	250	--	--	8.7	10.0	--	--	--
PUSH V code (Ref. 7)	177	330	394	--	--	27.8	175	310
Empirical Equation for basalt (Ref. 8)	170	--	--	--	--	--	--	--

Definitions:

V_s = peak spall velocity at GZ

V_{vl} = GZ velocity at time t_{vl}

V_v = GZ velocity at time t_v

t_s = time of onset of spall velocity at GZ

t_{sp} = time of peak GZ spall velocity

t_g = time of onset of surface gas acceleration phase

t_{vl} = time of first visible venting

t_v = time of total vent

Modified data from the SOC calculations were used as input for the PUSH V gas acceleration code (Reference 7). Estimates of the times of venting were based on interpretation of the PUSH V code results.

The empirical peak spall velocity prediction shown in Table 4.2 was derived from the results of cratering detonations in basalt (Reference 8). This empirical equation is represented by the expression:

$$Vs = 6.41 \times 10^6 \left(\frac{R}{W^{1/3}}\right)^{-2.1}$$

in which,

R = the radial distance from the shot point to the free surface in feet

W = equivalent energy yield in kilotons

4.4 RESULTS AND DISCUSSION

4.4.1 Falling-Mass Experiment

a. Photography. The black and white high-speed film (4000 fr/sec) from Camera 7 FTX (Table 4.1) was scheduled for use to analyze the results of the falling-mass experiment. This film could not be used for this purpose, however, because the red bowling ball appeared white on the film and, consequently, was "lost" in the white stripes of the graduated target background. Fortunately, Camera 716 PS (which was a part of the camera complement for the Pre-Schooner II Subsurface Effects Program) recorded approximately the same picture in MS color as did Camera 7 FTX. The field of view for Camera 716 PS was 77 feet (horizontal) × 55 feet. The film from this camera, therefore, was used for the falling-mass surface motion study. Analysis of the timing marks on the film indicated that the framing speed was 902 ±4 frames per second. This speed is considerably slower than that desired to best describe the surface spall acceleration period. Since data were taken at every frame, the time interval between data points for surface motion analyses was h = 1.11 msec.

b. Motion of the Graduated Target. The graduated target had very little horizontal displacement or rotational motion. The falling-mass target for the Dugout event experienced significantly more rotational motion, yet readings on two edges of the target produced only slightly different results for vertical motion (Reference 5). Based on this observation, it is reasonable to assume that the rotational motion of the Pre-Schooner II graduated target would yield differences well within the errors of the technique. Readings were taken, therefore, at only one position on the graduated target. Repeated readings of the film resulted in an average reading error of ±0.03 feet.

Figures 4.2, 4.3, and 4.4 show smoothed displacement, velocity, and acceleration components in the vertical direction. It can readily be shown (Reference 4) that the normal smoothing operation using smoothing parameter, P, and time interval,

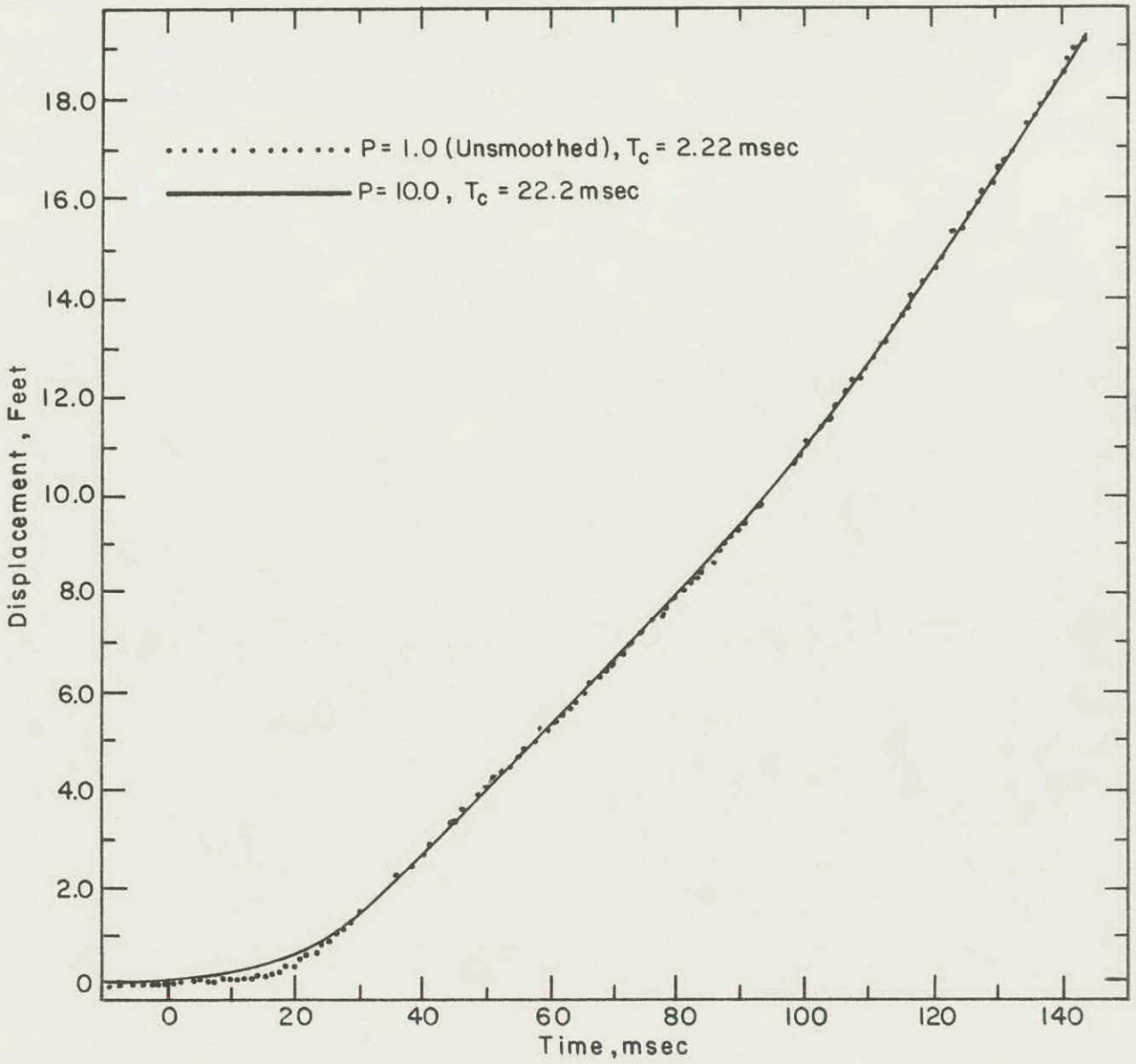

Figure 4.2 Vertical Component of Displacement of Graduated Target.

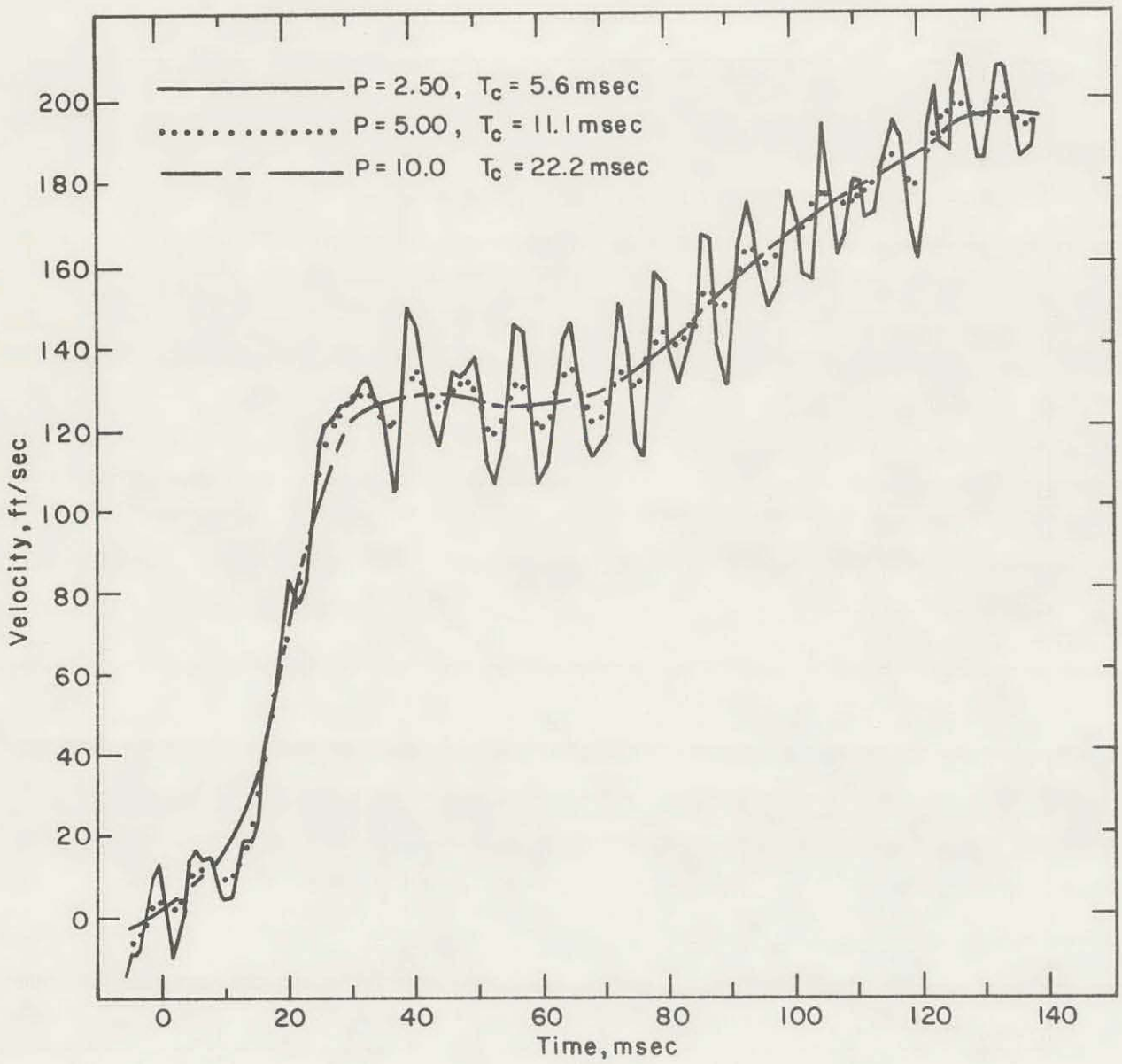

Figure 4.3 Vertical Component of Velocity of Graduated Target.

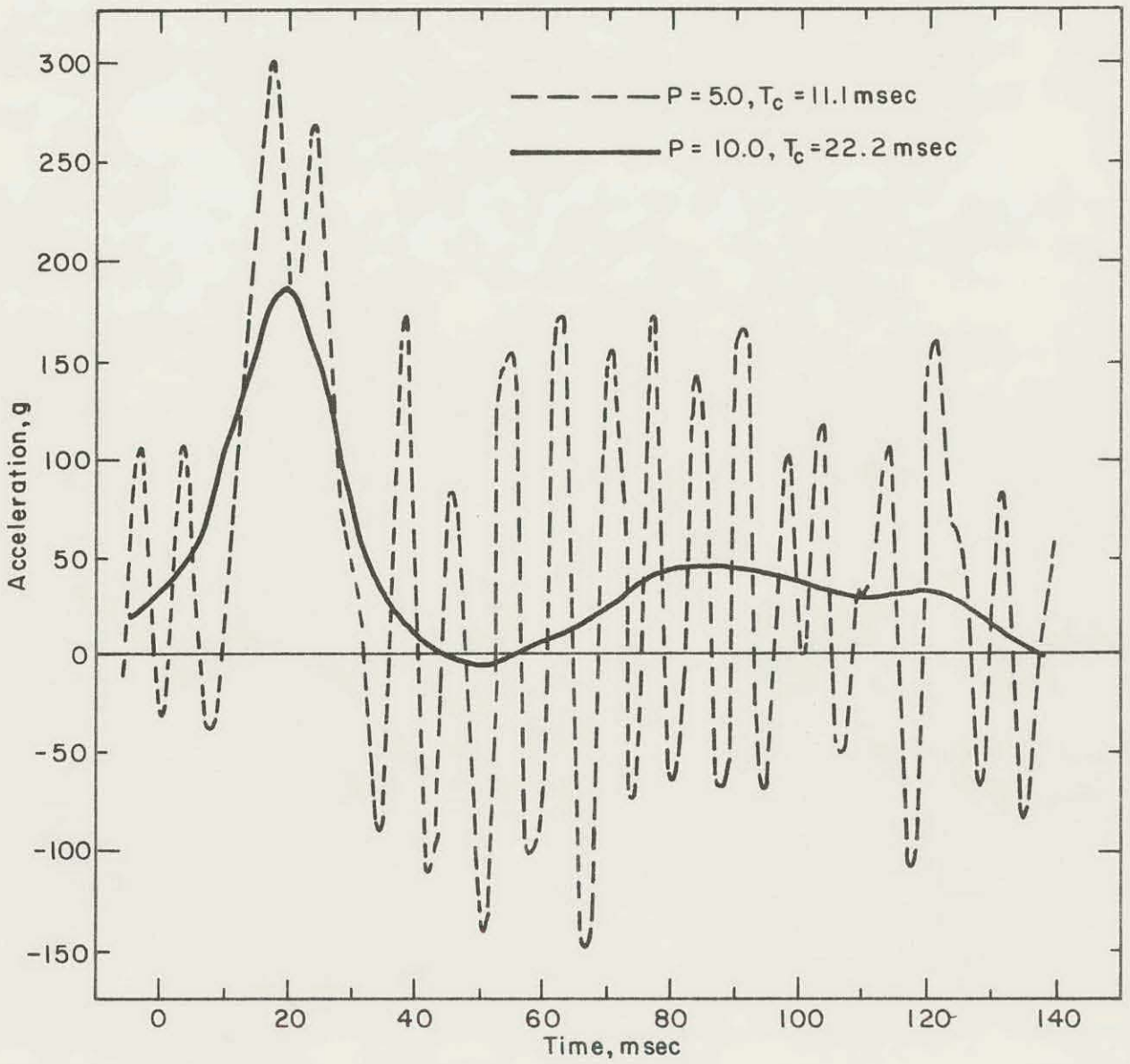

Figure 4.4 Vertical Component of Acceleration of Graduated Target.

h, between data points corresponds roughly to low pass filtering based on $T_c = 2Ph$, the minimum distance between peaks.

Figure 4.2 shows that the smoothing technique (which is necessary to reduce "reading error noise")[1] has its most pronounced effect on the desired signal (actual target motion) during the most critical period for study of surface spall (10-30 msec). Since this period contains the largest high frequency contributions to the signal, extreme care is necessary in applying any smoothing technique. Figure 4.3 compares the falling-mass target velocities for three different degrees of smoothing. It should be noted that while the reading error noise is reduced by increasing the smoothing from P = 2.5 to P = 5, the steep rise in velocity is affected to a much lesser degree. This suggests that most (but not necessarily all) of the significant wavelengths in the critical region for surface spall analysis are greater than 11.1 msec.

The following results are based on the P = 5 curve in Figure 4.3:

$t_s = 12 \pm 2$ msec (time of onset of spall velocity at GZ)

$V_s = 129 \pm 4$ ft/sec (peak spall velocity at GZ)

$t_{sp} = 27 \pm 4$ msec (time of peak spall)

$t_g = 68 \pm 5$ msec (time of onset of surface gas acceleration phase)

It should be further noted that although the times t_s and t_g are sensitive to the degree of smoothing, the peak spall velocity estimates would be only slightly different whether P = 2.5, 5, or 10 unless the peak spall velocity occurred as a very short duration peak (less than 5 msec) that for some reason quickly diminished to 129 ft/sec. While a feature such as the sharp peak described above is not a likely occurrence, it is possible that a short wavelength phenomenon such as an elastic precursor could be missed as a result of the relatively coarse time interval used between data points and the film reading error.

Comparison of Figures 4.2, 4.3, and 4.4 reveals the significant amplification of the higher frequencies which results from the differentiation process. Compared with the continuously recording wide-frequency-response accelerometers used in the Pre-Schooner II Subsurface Effects Program, the acceleration of the graduated target is much too fluctuating and the data time interval too large to produce meaningful results for comparison with early-time code predictions. Analysis of the graduated target is capable, however, of giving the lower-frequency late-time accelerations which the accelerometers would miss.

c. Motion of Visual Surface Targets near GZ. The field of view of the film from Camera 716 PS was sufficiently wide to permit detailed study of targets 1A

[1] "Reading error noise" refers to the fluctuating error in the ability to read the target positions and the resulting errors in computed velocities and accelerations.

and 1B (Figure 4.1) using the falling-mass technique. Vertical velocity components (smoothed using P = 5) of the graduated target and targets 1A and 1B are shown in Figure 4.5. Figure 4.6 shows shows the unsmoothed horizontal displacement and smoothed (P = 5) horizontal component of velocity of target 1B. This figure illustrates the scatter in the displacement data. It is noted that the initial swing of the target toward GZ occurred at about 18 msec. A torque was applied to the target such that the bottom of the target, which was emplaced in the ground, moved outward with the ground leaving the above-ground target mass behind the first 30 msec. Although the fact that the target motion is not exactly the same as the ground surface motion has an effect on early horizontal motion, horizontal velocity oscillations are not much larger than the vertical oscillations. This is a distinct improvement over observed target motions for previous cratering events. The rotation of the target has negligible effect on the vertical motion.

4.4.2 Surface Target Array Experiment

a. Photography. The film from Camera 773 PS (Table 4.1) was used to analyze the motion of the array of visual surface targets along the line 7A to 7B (Figure 4.1) As a result of the larger field of view, the reading errors for this analysis were larger than were those for the falling-mass experiment. With a reading error of ±0.18 feet, a fine data time interval was not considered to be warranted. Since no timing lights appeared on the film, the camera speed was inferred by comparing the displacements of targets 1A and 1B with the respective displacements on the falling-mass experiment film. The camera speed determined in this manner was 880 frames per second, and data were taken in three sets at intervals of 2, 4, and 8 frames (2.27, 4.54, 9.1 msec, respectively).

b. Effect of Using Nonstationary Reference Points. Since no better reference points were available for use in analyzing the visual surface target motion, targets 7A and 7B were used as position reference points (fiducial targets). These targets experienced some motion as a result of the Pre-Schooner II detonation, and, therefore, in order to use them as reference points it was assumed that: (1) the horizontal motion of these two targets was symmetrical about GZ, and (2) the vertical motion was comparable to horizontal motion. By using the first assumption, a coordinate transformation was made based on target 7A as the origin of coordinates. After computing the horizontal displacement of target 7B in any one frame, a new transformation of coordinates was made such that the new origin was midway between targets 7A and 7B. This origin moved vertically, however, from frame to frame with the mean actual vertical velocity component of targets 7A and 7B. The visual surface target motion was measured relative to this coordinate system.

Figure 4.7 indicates the amount of error introduced as a result of the above assumptions. This figure shows a plot of the horizontal displacement and velocity of

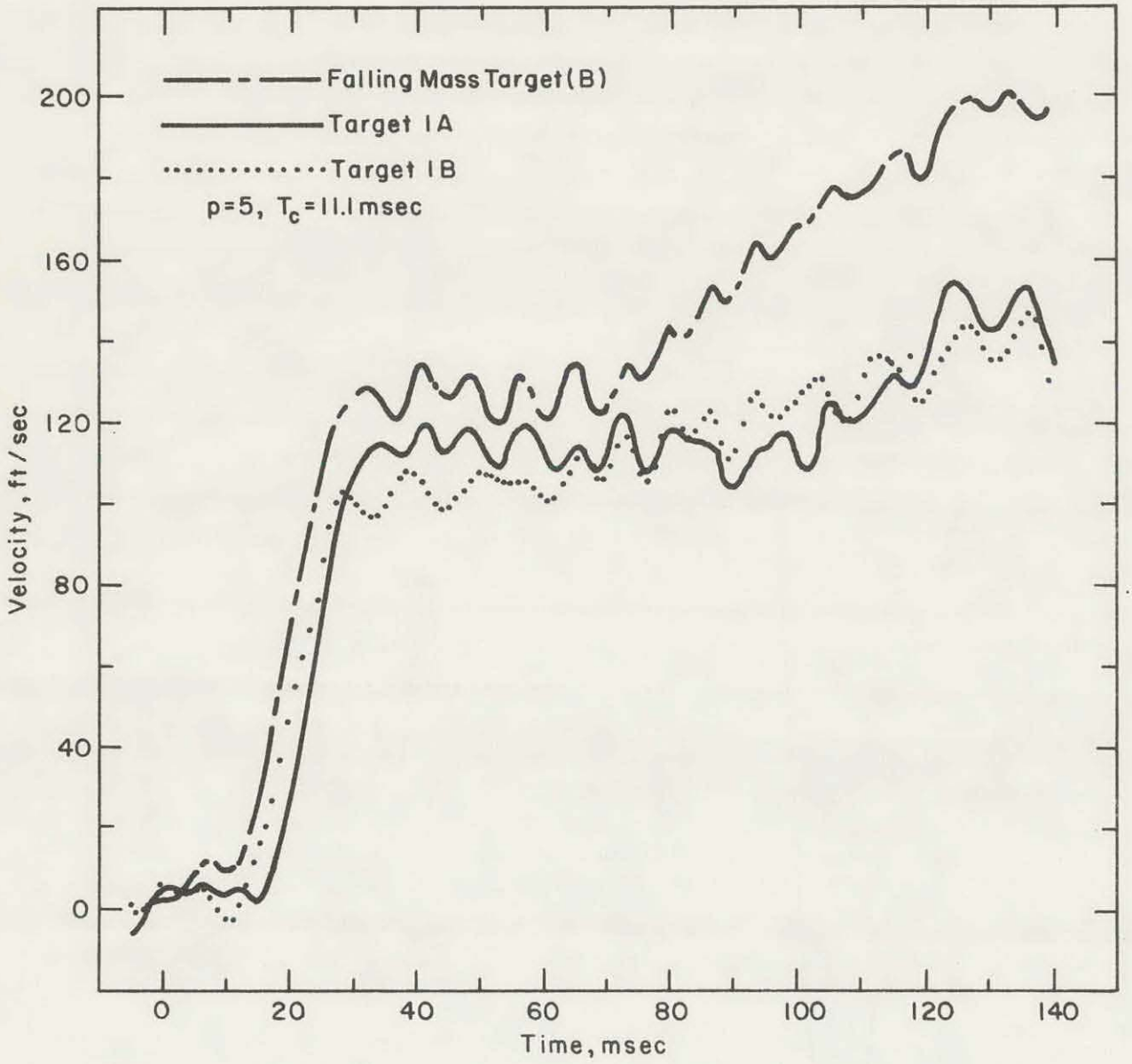

Figure 4.5 Vertical Component of Velocities of Target 1A, 1B, and Graduated Target.

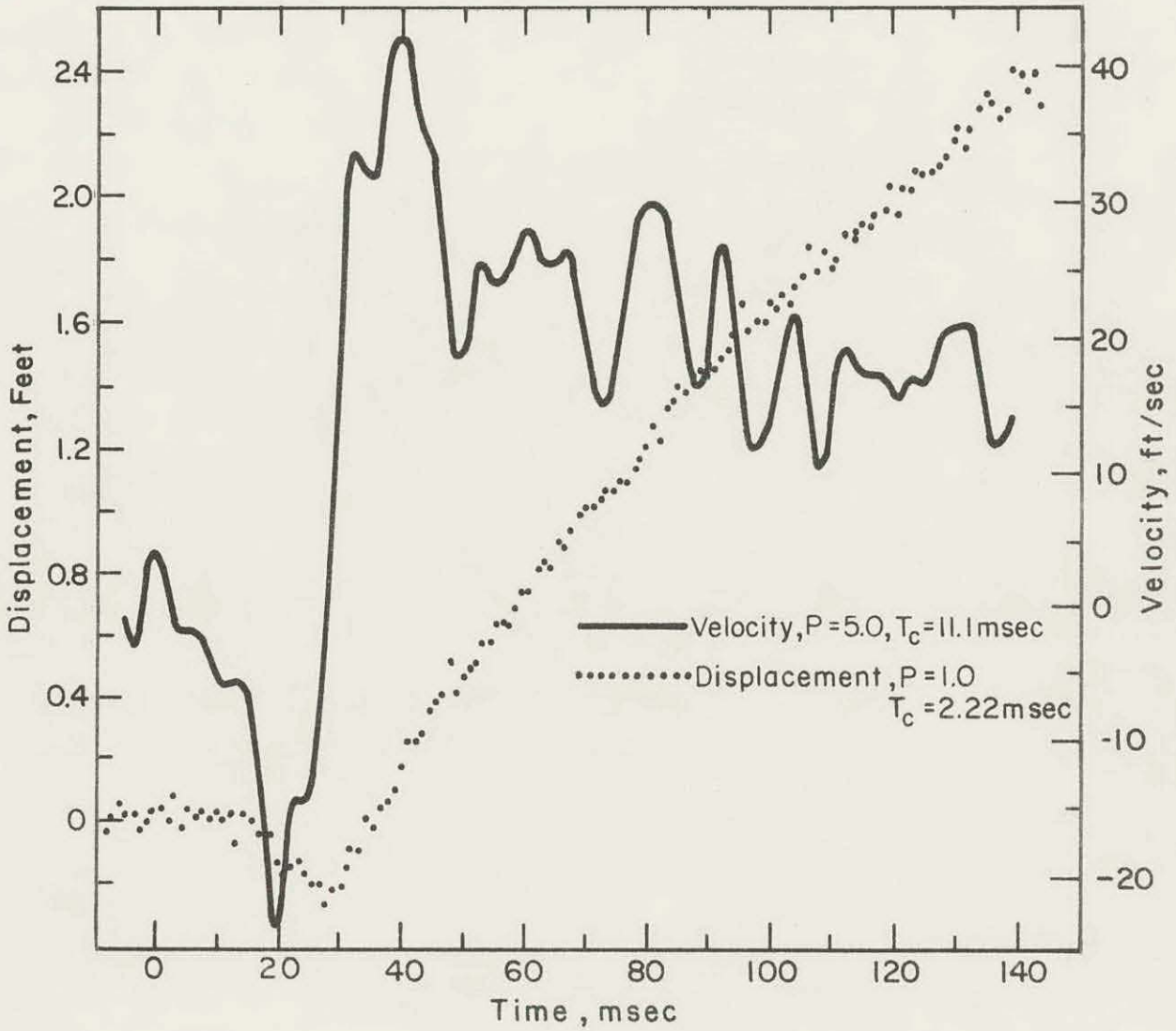

Figure 4.6 Horizontal Components of Displacement and Velocity of Target 1B.

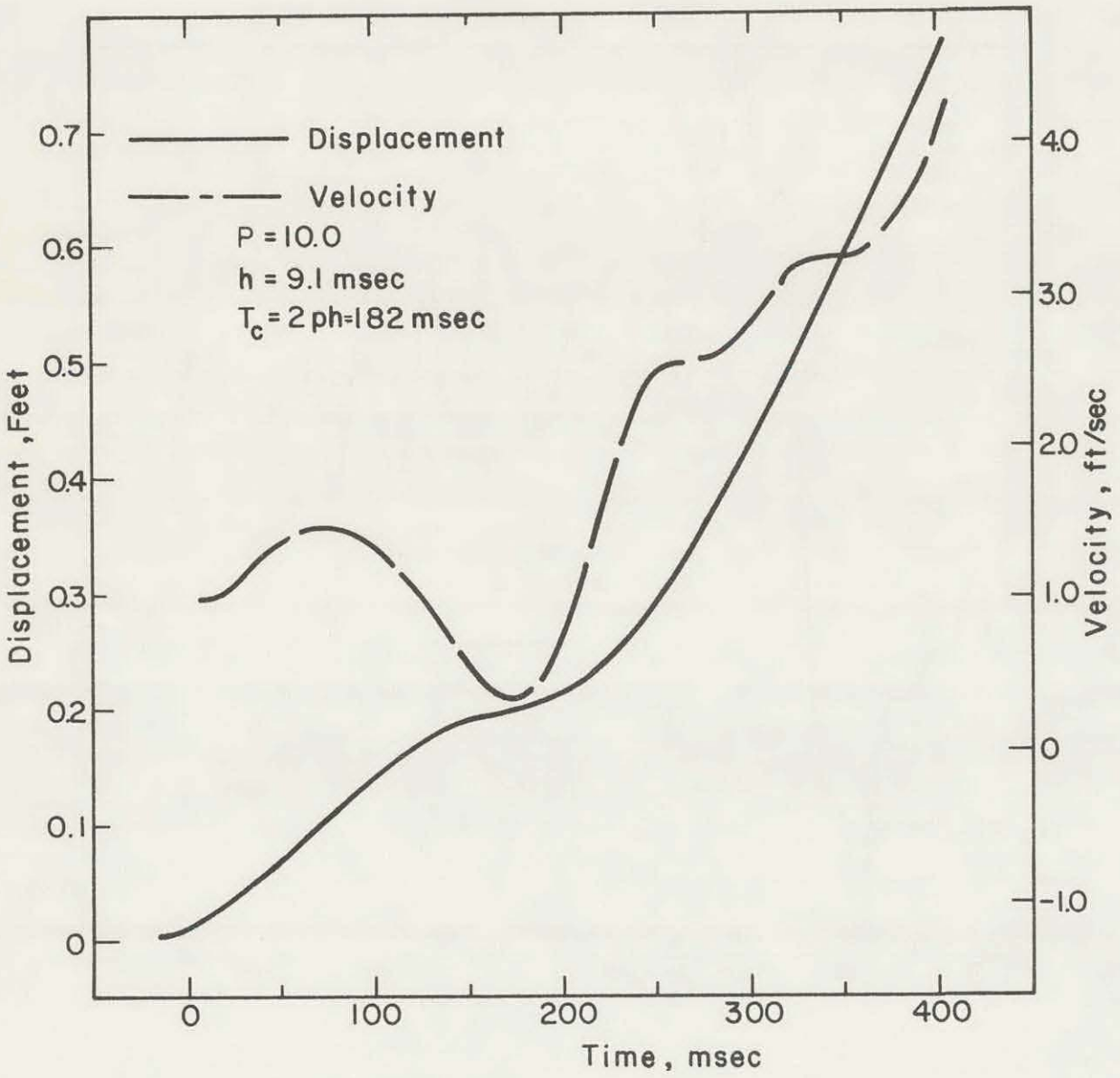

Figure 4.7 Horizontal Components of Displacement and Velocity. of Target 7B (Right Fiducial)

target 7B (smoothed such that T_c = 182 msec because of the large ratio of reading error noise velocity to actual velocity). It should be noted that for early times (t < 200 msec) the velocity is less than 1.5 ft/sec. Based on the assumption that vertical velocity is equal to horizontal velocity for these fiducial targets (which is not unreasonable), this error term must be added to the vertical velocities of the other targets. This correction procedure is significant only for the targets most distant from GZ. (The motion curves shown in Figure 4.7 also reveal the interesting phenomenon that for these targets which were located at a considerable distance from GZ, the motion is quite small until late times – 225 msec – and then begins to increase).

c. Visual Surface Target Motion. Figure 4.8 shows long-time vertical velocity components for all the visual surface targets. The data presented are based on a smoothing factor such that T_c = 45.4 msec. It is noted that a second phase rise in velocity (gas acceleration) is barely evident 60 feet from GZ and is questionable beyond that distance although the velocities tend to increase with late time for almost all targets. Table 4.3 gives a resume of diagnostic information for the visual target motions. The falling-mass film was used to analyze the motion of targets B, 1A, and 1B. For the other targets, the following data time interval and smoothing factor were used.

$$h = 2.27 \text{ msec}$$
$$P = 5$$
$$\therefore T_c = 22.7 \text{ msec}$$

The spall arrival times, t_s, are quite consistent for all the targets. A travel-time curve (plot of t_s versus distance R from the shot point to target) is reasonably well fitted by a straight line which indicates an average apparent shock wave velocity of 6250 ft/sec.

Figure 4.9 is a hodograph showing target trajectories for early times (prior to venting). From such a plot the directions of early target motion can be measured. It should be noted that the trajectories for some targets are not straight. This is due primarily to target rotation and, in small measure, to the acceleration of gravity as well as to the possibility that the ground actually may well be subjected to a more horizontal push at later times. Table 4.4 shows the initial directions of target motion θ_o and radial direction θ_r, both illustrated in Figure 4.9. The primary observation which can be made is that although θ_o increases with increasing values of θ_r, θ_o is invariably less than θ_r and this disparity increases as θ_r increases.

d. Flare Surface Target Motion. The first countdown for the Pre-Schooner II detonation was stopped at approximately 9 seconds prior to zero time because it appeared that some of the baritol flares (which were ignited at H-15 seconds) were not burning properly. Since reloading of the flare holders with baritol would have

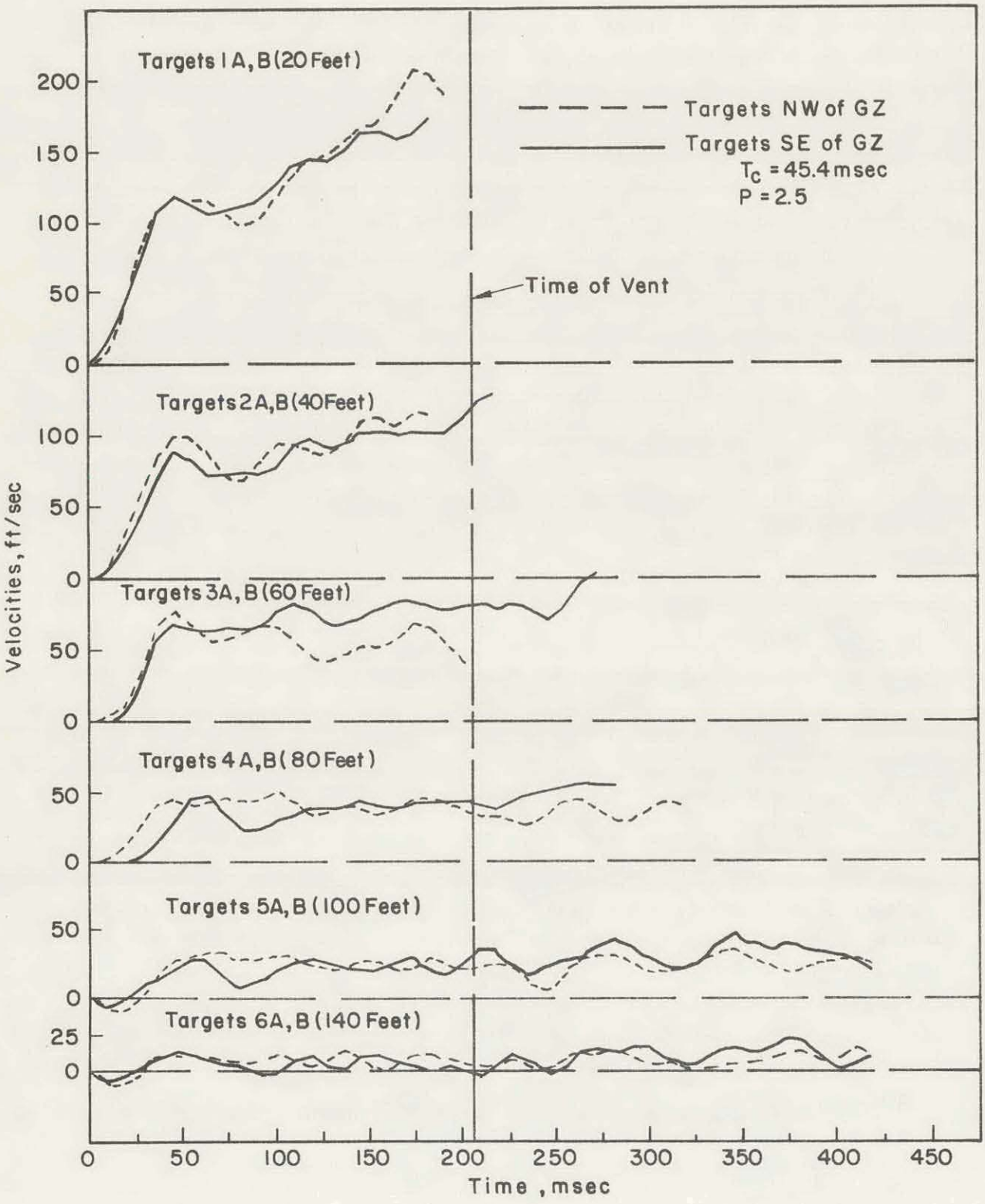

Figure 4.8 Vertical Components of Velocities of Visual Surface Targets.

TABLE 4.3 RESUME OF DIAGNOSTIC TARGET VELOCITIES AND CHARACTERISTIC TIMES

Target No.[a]	x	R	V_s	t_s	t_{sp}	V_{vl}	t_g
	ft	ft	ft/sec	msec	msec	ft/sec	msec
6A	140	158	12±5	27±4	37±15	8	--
5A	100	123	25±7	22±4	35±60	23	--
4A	80	107	44±4	17±3	41±6	35	87±12
3A	60	93	73±5	17±3	40±5	50	61±10
2A	40	81.5	94±6	14±2	40±5	115	78±10
1A	20	74	118±6	15±2	33±5	200	90±10
B	7	71.5	129±4	12±2	27±4	--	68±5
1B	20	74	103±6	13±2	28±5	170	69±10
2B	40	81.5	76±6	15±2	39±5	115	--
3B	60	93	65±5	16±3	38±6	80	--
4B	80	107	33±4	19±3	49±7	40	--
5B	100	123	21±5	21±4	60±15	24	--
6B	140	158	6±3	--	50±80	3	--

[a]Refer to Figure 4.1 for target locations.

x = distance from GZ to preshot target location

R = distance from shot point to preshot target location

V_s = peak vertical spall velocity

t_s = time of onset of vertical spall velocity

t_{sp} = time of peak vertical spall velocity

V_{vl} = vertical velocity at time of primary vent

t_g = time of onset of gas acceleration

B = graduated target

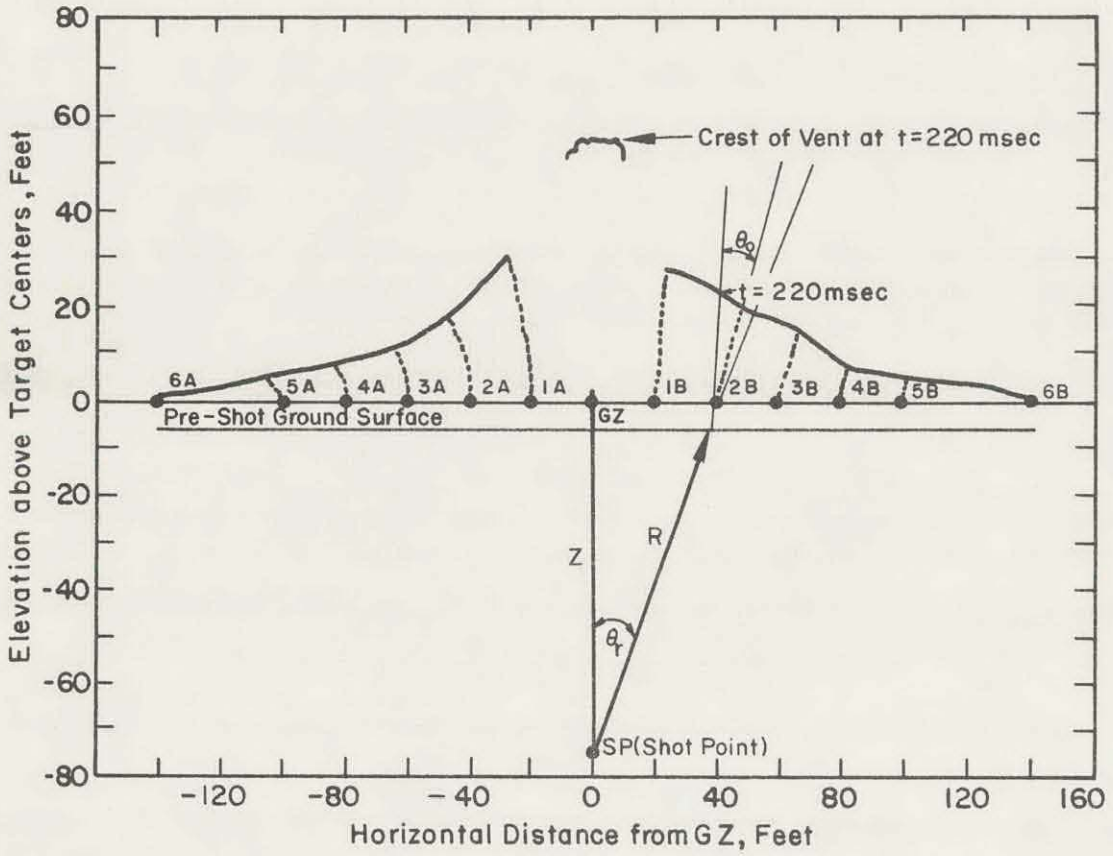

Figure 4.9 Hodograph of Visual Surface Target Trajectories.

required a time delay of several hours, and a delay of this length would have required that the detonation be rescheduled for the next day (due to inadequate lighting conditions for scientific photography), the Technical Director decided to proceed with a second countdown without the flares. As a result of this sequence of events, no surface flare motion study was possible for the Pre-Schooner II event.

4.4.3 Pertinent Cratering Formation Phenomena Observed from High-Speed Photography. In addition to providing detailed information on Pre-Schooner II surface motion, the high-speed motion picture films revealed several phenomena pertinent to the formation of the crater. Table 4.5 presents a chronological history of some of these phenomena. The height of the dome at the time of the primary vent was 23.4 feet and the width of the dome measured northwest to southwest was 215 feet. The vent grew to the width of the dome (215 feet) at the time of total breakup of the mound. The initial velocity of the venting gas was 1240 ft/sec, leveling off to 700 ft/sec between 300 and 400 msec.

TABLE 4.4 EARLY DIRECTION OF TARGET MOTION (θ_o)

Target No.	x	θ_r	θ_o
6A	140	63° 10'	49°
5A	100	54° 40'	47°
4A	80	48° 30'	40°
3A	60	40° 10'	18°
2A	40	29° 20'	20°
1A	20	14° 40'	10°
B	7	5° 40'	--
1B	20	14° 40'	8°
2B	40	29° 20'	25°
3B	60	40° 10'	28°
4B	80	48° 30'	26°
5B	100	54° 40'	32°
6B	140	63° 10'	34°
7	180	--	--

θ_o = angle between vertical and the early direction of target motion

θ_r = angle between vertical and the straight line connecting the shot point with the initial target position

θ_o and θ_r shown in Figure 4.9.

TABLE 4.5 CHRONOLOGY OF CRATERING FORMATION PHENOMENA

Time	Comments
msec	
0	Support cable on falling-ball experiment detonated
8.9	First motion of shallow push rod (see Section 5.3.6).
13.3	Bright flash appears to rise from the deep push rod hole; grows to about 10 feet in height (see Section 5.3.6).
158.9	Mound forms inner dome
204	Primary vent over GZ (vent grows to become total vent).
607	Mound appears to have completely broken up.

4.5 INTERPRETATIONS AND CONCLUSIONS

4.5.1 Comparison of Predicted and Observed Ground Zero Surface Motion

a. General. Although the graduated target for the falling-mass experiment was located 7.1 feet from GZ rather than at GZ, it is believed that the analysis of the motion of this target accurately represents the GZ surface motion. Table 4.6 is a compilation of the predicted GZ motion and the observed graduated target motion. A discussion of the predicted and observed GZ surface motion phenomena is presented in the following paragraphs.

TABLE 4.6 COMPILATION OF PREDICTED PRE-SCHOONER II GZ MOTION AND OBSERVED GRADUATED TARGET MOTION

Feature	Predicted Value		Observed Value
	SOC Code (Ref. 6)	PUSH V Code (Ref. 7)	
V_s, ft/sec	250	177	129±4
V_{vl}, ft/sec	--	330	210±20[a]
t_s, msec	8.7	--	12±2
t_{sp}, msec	10.0	--	27±4
t_g, msec	27.8	--	68±5
t_{vl}, msec	--	175	200±5

V_s = peak spall velocity at GZ

V_{vl} = velocity at time of primary vent (t_{vl}) at GZ

t_s = time of onset of spall velocity at GZ

t_{sp} = time of peak spall velocity at GZ

t_g = time of oneset of gas acceleration at GZ

t_{vl} = time of primary vent at GZ

[a]Motion of the graduated target was not analyzed for times later than 144 msec. The estimate of 210 ft/sec is based on the observed velocities of targets 1A and 1B at the time of primary venting.

b. Peak Spall Velocity. The peak spall velocity of 129 ft/sec, as determined from the falling-mass experiment, is considerably less than that predicted by the SOC calculation (250 ft/sec) and is somewhat below the empirical equation prediction of 170 ft/sec (Reference 8) and the estimated value of 177 ft/sec predicted in Reference 7. Part of the discrepancy between the predicted and observed peak spall velocities is due to the fact that the predictions were based on a charge weight of 100 tons of NM while the actual charge weight was approximately 85.5 tons. The low observed peak spall velocity suggests that the Pre-Schooner II medium was more compressible and/or of lower strength than was indicated by the values used as input into the SOC code (these values were based on strength and equation of state tests made on small core samples).

c. Peak Velocity Prior to Venting. The PUSH V calculation predicted a peak velocity prior to primary venting of 330 ft/sec as compared with the observed value of approximately 210 ft/sec. Since the input conditions for the PUSH V calculations were dependent on SOC code output, the PUSH V solution cannot be adequately evaluated. The time of primary venting was reasonably well estimated in Reference 7; however, the primary vent developed into a total vent more rapidly than was predicted.

d. Times of Onset of Spall Velocity and Peak Spall Velocity. The time of onset of spall, t_s = 12 msec, was approximately 3 msec later than was predicted by the SOC code. This difference may very likely be due to the coarse time interval used between data points and the data smoothing procedure used in analyzing the surface motion photography.

The slow velocity rise time from the time of onset of spall (t_s) to the time of peak spall velocity (t_{sp} = 27 msec) is believed to be significant relative to the 1.3 msec SOC prediction. This slow rise time phenomenon could be attributed to one or several of the following factors:

(1). A more compressible, lower-strength cratering medium than was inferred from laboratory measurements on small core samples.

(2). Sluggishness of the target (due to inertia and poor coupling with the ground).

(3). The coarse time interval used between data points in analyzing the target motion and the high reading error noise level.

For the reasons indicated in Section 4.4.1b, it is believed that Factor 3 as listed above did not have a significant effect on the rise time. Factor 2 is difficult to evaluate because the ground surface velocity was not measured directly. Considering the low spall velocity mentioned in Section 4.5.1b, Factor 1 probably had the most significant influence on the velocity rise time.

e. Onset Time for Surface Gas Acceleration. If the observed secondary rise in velocity at 68 msec has been correctly interpreted as the beginning of gas acceleration at the ground surface, this phenomenon occurred at a much later time than was predicted by the SOC code (27.8 msec). In the past, it has been estimated that the surface gas acceleration phase begins at a time given by the sum of the following wave travel times (Reference 3):

(1). Elastic wave travel time from the cavity to the surface through the consolidated medium.

(2) Rarefaction wave travel time through the crushed medium from the surface to the expanding cavity.

(3) Recompaction wave travel time through the crushed medium from the cavity to the surface.

The observed Pre-Schooner II time of onset of surface gas acceleration was later than the time predicted by a factor greater than two. A very probable source of the discrepancy between the observed and predicted values may be the equations of state of the consolidated and crushed Pre-Schooner II media used in the SOC calculations.

4.5.2 Decrease in the Vertical Velocity Components with Distance From GZ. The decrease of the peak vertical spall velocity component with distance from GZ is another diagnostic feature which can be compared with cratering model predictions. As indicated in Figure 4.9, the distance from the shot point to any surface target may be expressed as:

$R = Z/\cos\theta_r$ in which Z is the depth of burst.

If the peak vertical component of surface spall velocity is given by the expression

$V_s \propto R^{-n}$ in which n is a constant,

then, this velocity component may be written as a function of $\cos\theta_r$; i.e.,

$$V_s \propto (Z/\cos\theta_r)^{-n} \propto \cos^n\theta_r.$$

Figure 4.10 is a log-log plot of measured values of peak vertical component of spall velocity (V_s) versus $\cos\theta_r$ for the Pre-Schooner II visual surface target array. These data are reasonably well-fitted by a straight line with a slope of n = 3.0. The velocities plotted in Figure 4.10 have not been corrected for fiducial target movement; however, such a correction would decrease the value of the exponent, n, only slightly. Previous measurements and code predictions for cratering detonations in desert alluvium have resulted in exponents of $n \sim 3$ while the ground surface motion for the Pre-Schooner CHARLIE event in basalt was characterized by an exponent of $n \sim 6$ (Reference 7).

The reduction of the vertical component of velocity with increasing values of θ_r at the time of primary vent of the Pre-Schooner II detonation was studied using a plot similar to Figure 4.10. The exponent determined by a best straight line fit to the data was n = 3.6. This exponent indicates a slightly greater reduction in the effect of gas acceleration with increasing distance from GZ as compared to that of the spall phenomenon.

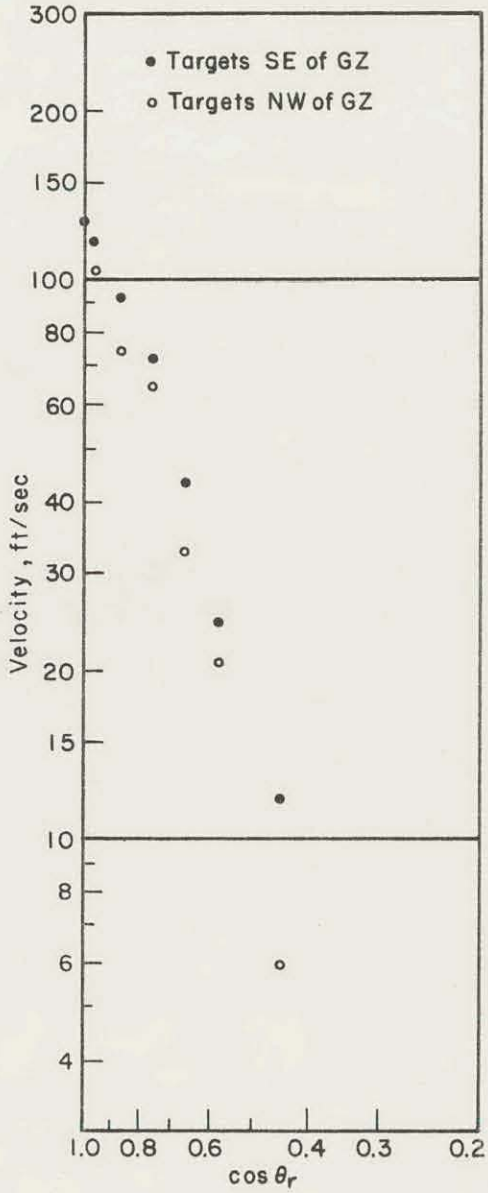

Figure 4.10 Vertical Component of Peak Spall Velocity versus Cos θ_r.

4.5.3 Early Directions of Motion. Although the picture is confused somewhat by target rotation, the estimates of the early directions of target motion deviated from the radial direction from shot point to target (Table 4.4). This deviation increased with increasing distance from GZ. In this connection, it is considered pertinent to note that the initial direction of ground motion used in the PUSH code models for gas acceleration is assumed to be radial.

4.5.4 Evaluation of Experimental Procedures. A portion of the Pre-Schooner II surface motion study effort was devoted to an evaluation of the surface motion experimental procedures which were used. Conclusions and recommendations based on this evaluation are as follows:

a. The close-in photography of the falling-mass experiment permits more accurate target position readings (and, consequently, considerably better early-time GZ surface motion) than is possible from the surface target array experiment.

b. The stripes on the graduated target were unnecessary and, in fact, added to the bowling ball position reading error. Lack of contrast between the red bowling ball and white target strips rendered black and white photography unsatisfactory for data analysis of the falling-mass

experiment. It is recommended that in future falling-mass experiments the graduated target be replaced by a target of the same shape painted black except for two painted white crosses which can be used as reference points. The crosses should be so located that no portion of either one becomes obscured by the falling-mass during the vertical motion of the target.

c. Improved design of the graduated target support and bracing of the plywood panel to the support resulted in much smaller horizontal target motion than that experienced during previous cratering events.

d. The Pre-Schooner II surface motion targets were designed with lower centers of mass than were those for previous events and, as a result, evidenced less rotational oscillation.

e. The data analysis techniques used for the Pre-Schooner II surface motion study reduced the data processing time sufficiently to permit the study of the motion of many visual targets within a reasonable time frame.

f. The relatively coarse time interval between data points used for the analyses of the Pre-Schooner II falling-mass experiment (necessitated by the low framing rate – 902 fr/sec – of the camera) reduced, to some extent, the effectiveness of the falling-mass experiment.

Reference 9 discusses the problem of choosing the optimum time interval between data points so as to minimize: (1) reading errors, (2) distortion of the true target motion, and (3) the data analysis effort.

REFERENCES

1. S. A. Feegenbaum and P. L. Wegkamp; "Photographic Earth Motion Study Scooter Event"; Final Report No. L-510, 1961, Edgerton, Germeshausen, and Grier, Inc., Las Vegas, Nevada.

2. J. B. Knox and R. W. Terhune; "Cratering Physics Concepts Derived From an Analysis of Ground Surface Motion; "UCID-4669, 1963; Lawrence Radiation Laboratory, Livermore, California.

3. J. B. Knox and R. W. Terhune; "Calculation of Explosion Produced Craters – H. E. Sources"; UCRL-7738 Rev. I, 1964; Lawrence Radiation Laboratory, Livermore, California.

4. R. W. Terhune, R. L. Fulton, and J. B. Knox; "Reduction of Photographic Surface-Motion Data by Digital Computer"; UCRL-14155, 1965; Lawrence Radiation Laboratory, Livermore, California.

5. R. W. Terhune; "Project Dugout, Surface Motion Studies"; PNE-603, to be published; Lawrence Radiation Laboratory, Livermore, California.

6. T. Butkovich; "Pre-Schooner II Pre-Shot SOC Calculation"; UOPKA 65-18, 1965; Lawrence Radiation Laboratory, Livermore, California.

7. R. W. Terhune; "Push V in Basalt and Pre-Schooner II Crater Predictions"; UOPKA 65-19, 1965; Lawrence Radiation Laboratory, Livermore, California.

8. L. Vortman; "Project Buckboard"; SC 4675(RR), 1960; Sandia Corporation, Albuquerque, New Mexico.

9. K. L. Larner; "Project Pre-Schooner II, Surface Motion Studies"; PNE 513F, to be published; U. S. Army Engineer Nuclear Cratering Group, Livermore, California.

CHAPTER 5

SUBSURFACE EFFECTS MEASUREMENTS

5.1 INTRODUCTION

The scope of the Pre-Schooner II Subsurface Effects Technical Program included the following four separate areas of measurements:

a. Measurement of early subsurface stress wave phenomena using stress transducers, ferroelectric switches, slifer systems, and accelerometers.

b. Measurement of late cavity pressure using pressure transducers and fluid coupling with the cavity.

c. Observation of late vertical subsurface ground motion using push rods.

d. Measurement of the temperature of the cavity gas at time of venting by determination of luminosity.

This chapter describes the experimental procedure and the preliminary results of the Subsurface Effects Technical Program. The reliability of the data obtained are also discussed. Although some of the data may be corrected in the final report (Reference 1), the preliminary results presented in this chapter are believed to be substantially correct.

5.2 EXPERIMENTAL PROCEDURES (Reference 2)

5.2.1 Subsurface Stress Wave Measurements

a. Instrumentation Layout. The subsurface stress wave phenomena program included measurements of the stress history from the Pre-Schooner II detonation in the horizontal direction in the relatively uniform felsite rock, and the stress history in the vertical direction through the layered structure consisting of the felsite, the vitrophyre and vitrophyre breccia, the residual soil overburden, and the surface of the earth. Figure 5.1 shows the layout of the stress wave instrumentation, and Figure 5.2 shows a plan view of the instrument hole locations. These instrument holes were approximately 10 inches in diameter and were cased for the first 10 feet from the surface. The instruments were grouted in place with a grout mixture designed to match the density and compressibility of the felsite by the U. S. Army Corps of Engineers Waterways Experiment Station. All of the holes were grouted up to the surface except the accelerometer hole, I-3, in which the upper surface of the grout was 9 feet below the surface of the ground.

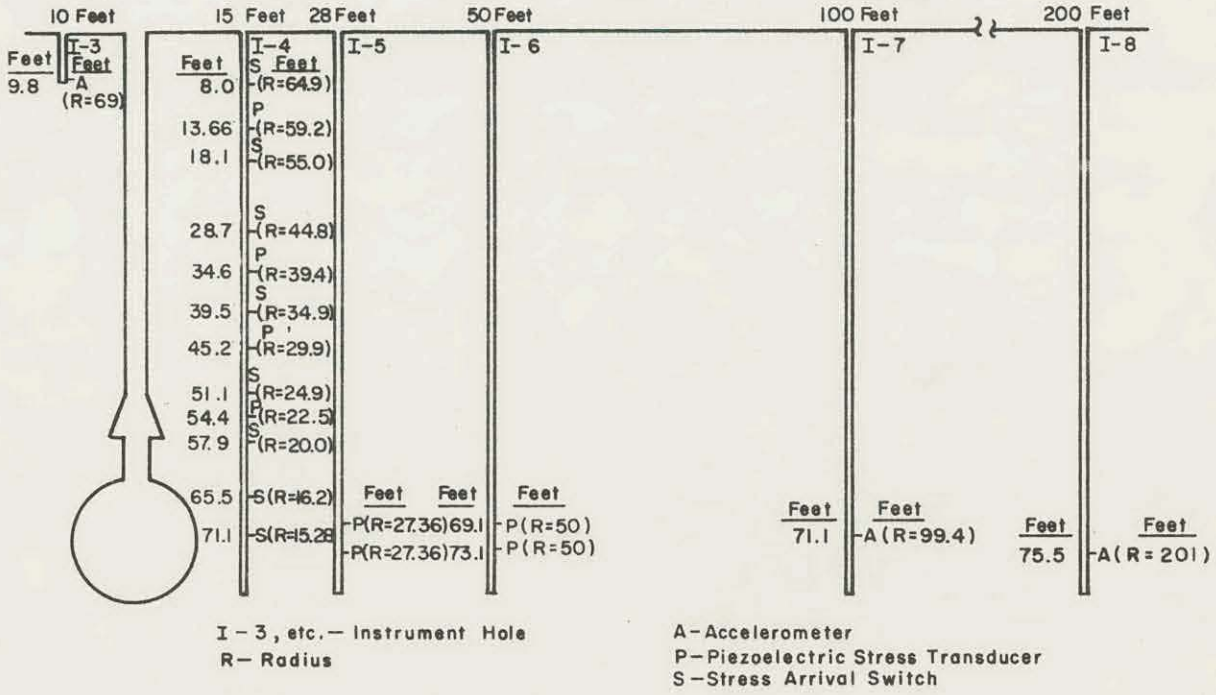

Figure 5.1 Subsurface Effects Instrumentation Layout.

b. Radial Stress History Instrumentation. To measure the radial stress history in the horizontal direction, two tourmaline stress transducers were installed in both hole I-5 and hole I-6 (28 and 50 feet from GZ, respectively) at shot depth (Figure 5.1).

To measure the radial stress history in the vertical direction, single piezoelectric crystal transducers were placed in hole I-4 (15 feet from GZ) at distances of 22.5, 29.9, 39.4, and 59.2 feet from the center of the detonation (Figure 5.1).

c. Shock Arrival Time Instrumentation. Instrumentation to measure shock arrival time in the vertical direction included ferroelectric switches and a conventional slifer system.

The ferroelectric switches (located in hole I-4) consisted of ferroelectric elements which would be quickly driven into saturation by the arrival of the stress wave. The signal from each switch was impressed on an RC circuit with a relatively short time constant so that four arrival time switch systems could be connected in parallel and recorded on a single recording channel.

The conventional slifer system, which extended downward toward the detonation point in hole I-4 along with other stress wave instrumentation, involved an oscillator with a shorted cable which served as part of the frequency-determining circuit of the slifer system. The basic operating principle of the slifer system is as follows: (1) as the outgoing wave crushes and shorts the cable progressively it changes the frequency of oscillation, and (2) this oscillation frequency, in turn, serves as a monitor of the position of the shock front. The slifer cable used in Pre-Schooner II was 3/8-inch Heliax H-3.

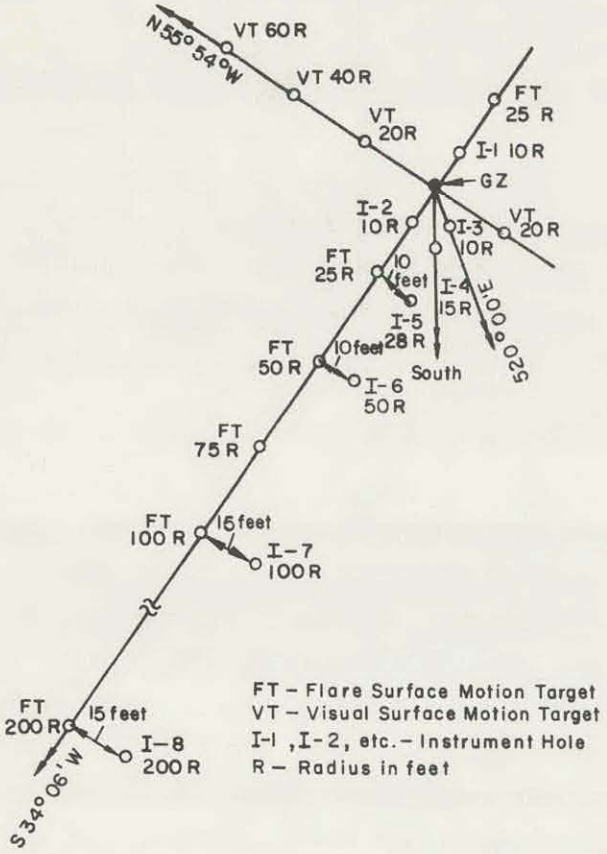

Figure 5.2 Location of Holes for Subsurface Instrumentation for Pre-Schooner II.

d. Subsurface Spall Instrumentation. The subsurface spall phenomena which occurred during the Pre-Schooner II crater formation was recorded by means of a dual-mode slifer system. This system was designed so that it would oscillate in either the short-circuit or the open-circuit condition. The frequencies involved were widely separated so that the mode of oscillation could be identified. This dual-mode slifer system extended down into hole I-4 to shot level.

e. Acceleration Instrumentation. An accelerometer, oriented to measure the vertical component of acceleration from the detonation, was placed in hole I-3 near the upper surface of the vitrophyre approximately 9 feet below the surface of the ground. In addition, accelerometers oriented to measure both the horizontal and vertical components of acceleration at the shot horizon, were placed in holes I-7 and I-8 (100 and 200 feet from the detonation point, respectively).

5.2.2 Cavity Pressure Measurements

a. General Discussion. In the mechanics of cratering, part of the momentum imparted to the material above the charge location is given by the outgoing stress wave while the remainder is produced by

the longer lasting pressure of the cavity gas. Since this second phase is of major importance in the cratering mechanics, information on the history of the cavity gas pressure is needed.

Up to this time, successful measurements of cavity gas pressure have not been made because instruments have not been built to withstand the high stresses and accelerations involved in the early phases of cavity expansion. In Project Pre-Schooner II, an effort was made to measure this pressure by locating the pressure transducers far from the explosion center, and by transmitting the pressure from the cavity to the transducers through a fluid-filled pipe. Success of this method would then depend upon the survival of this fluid column during the cavity expansion.

It was desired to measure only the relatively low pressures at relatively late times in the cavity, so that sensitive pressure transducers were required. In order to protect these transducers against destruction by the early shock and high pressure, a throttling system was devised so that the early surge of pressure would not reach these transducers. Over a longer time scale, however, these transducers should measure cavity pressure with good accuracy.

b. Description of Cavity Pressure Measuring System. Two somewhat independent systems were used to measure cavity pressure so that the results could be checked against each other. In each system a fluid-filled steel pressure tube, 2-1/4 inches O. D. and 1-1/4 inches I. D., extended from above the surface of the ground down to within about 8 feet 9 inches of the NM cavity, as is shown in Figure 5. 3. In order to avoid closure of these steel pipes at the lower ends by the high-intensity stress wave from the explosion moving out through the rock material, PVC plastic pipes 8 feet 5 inches long were used at the lower ends, so that these pipes would be shattered by the ground shock but would not be sealed shut.

One of the pipes was filled with a high-viscosity silicone oil, while glycerine was used in the other system. Since the velocity of sound in glycerine is greater than that in the silicone oil, the pressure signal in the glycerine-filled system should arrive earlier, giving a check on the proper behavior of the system.

The PVC plastic pipe at the lower end of the glycerine system was filled with Dow MS-80-25, which would explode when the shock from the main explosion reached it and in this way maintain an open channel from the shot cavity to the steel pressure pipe. In the other system the PVC pipe, as well as the steel pipe above it, was filled with Dow Corning 200 silicone fluid which had a viscosity of 1000 centistokes.

A tourmaline pressure transducer was located in the fluid near the upper end of each pipe. Above these transducers an orifice led into a second chamber, where a second tourmaline transducer was located, and from each second chamber another

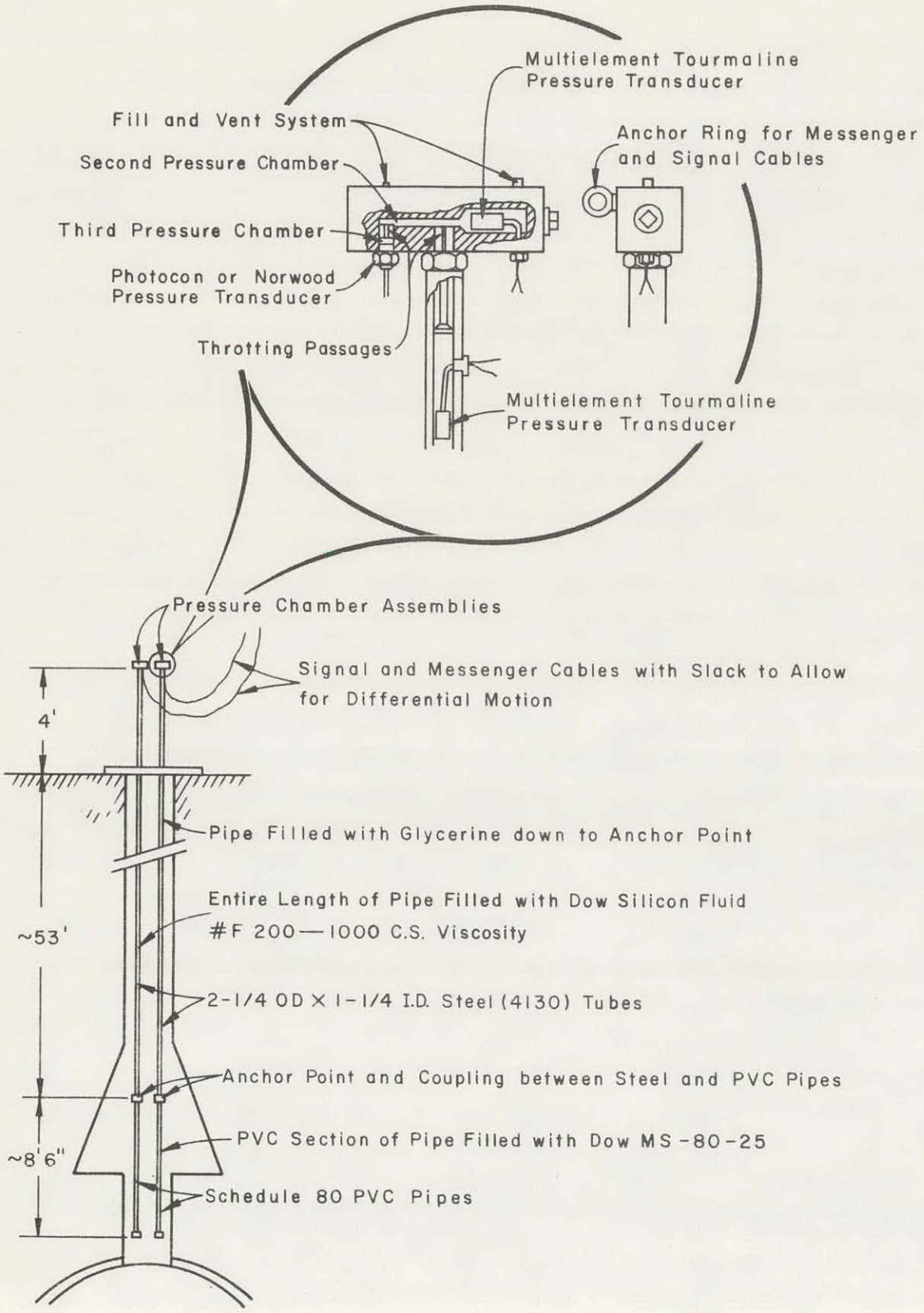

Figure 5.3 Cavity Pressure Measuring System.

orifice led into a small third chamber. In this third chamber a Norwood bridge-type pressure transducer was used in the silicone system, while a Photocon varying-capacitance pressure gauge was used in the glycerine system. (The word "orifice" is here meant as a small-diameter tube with length much greater than its inside diameter.)

c. Fluid Pressure Transmission. When the cavity gas pressure is suddenly applied at the lower end of the fluid pipes, a pressure disturbance will begin to move up the fluid at a shock velocity somewhat higher than the sound velocity of the fluid. The fluid itself behind the shock will be given a mass flow velocity obtained from the equation $P = \rho uv$, which relates pressure, density, and shock and particle velocities. This stress wave will be attenuated as it moves upward because of the drag between the viscous fluid and the pipe wall. An approximate analysis shows that the attenuation constant for the energy carried by this stress wave should be of the order of $4n/\rho r^2 c$ per unit length, where n is viscosity, ρ is fluid density, r is pipe radius, and c is fluid sound velocity.

The pertinent properties of the Dow Corning 200 silicone fluid include a density of 0.955 gm/cm^3, a viscosity of 1000 centistokes or 9.55 poise at 20° C, and a compressibility of 10 percent for 20,000 psi, which converts to a bulk modulus, K, of 1.38×10^{10} $dynes/cm^2$. Corresponding values for glycerine are a density of 1.260 gm/cm^3, a viscosity of 780 centipoise at 20° C, and a compressibility of 2.2×10^{-5} per bar at one bar, which converts to a bulk modulus of 4.55×10^{10} $dynes/cm^2$.

These fluids are quite compressible in comparison with steel so that the fluid pressure pulse as constrained by the walls of the pipe will be essentially in one-dimensional motion. Consequently, the sound velocities will be $(K/\rho)^{1/2}$, giving velocities of 1.20×10^5 cm/sec for the silicone oil and 1.90×10^5 cm/sec for the glycerine.

At a fluid viscosity of the order of 10 poise, the attenuation factor, $4n/\rho r^2 c$, over the fluid pipe length is of the order of 0.2 nepers; i. e., $\varepsilon^{+0.2}$, which is relatively small. In both glycerine and the silicone oil, however, the viscosity increases greatly with pressure, as is shown in Figure 5.4. For viscosities greater than about 100 poise the energy attenuation factor will be greater than ε^2 and the amplitude attenuation factor will be greater than ε so that the fluid will not effectively transmit a fluid pressure pulse at sound velocity. From Figure 5.4 this viscosity is reached at a pressure of about 1.5 kbars in the silicone oil and 5 kbars in the glycerine. This viscosity variation will thus serve as a limiting factor with respect to the early peak pressures that will arrive at the upper ends of the pipes.

The flow rate through a tube is calculated from the Hagen-Poiseuille law:

$$\text{Flow rate} = \frac{\pi r^4 (p_1 - p_2)}{8 l \eta},$$

where $p_1 - p_2$ is the pressure differential from one end of the tube to the other, r is tube radius, and l is tube length. This flow rate is countered by the pressure buildup in the chamber beyond, which is dependent upon the compressibility of the fluid and the volume of the chamber. This leads to a time constant of buildup of pressure in the chamber,

$$t_c = \frac{8 l V}{\pi r^4 K},$$

where V is volume of the chamber and K is bulk modulus of the fluid.

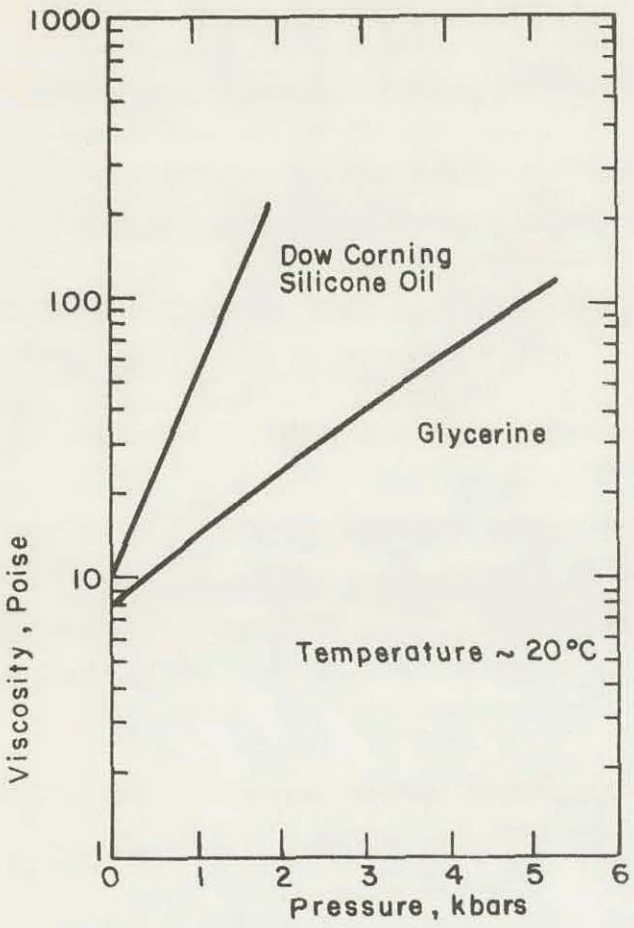

Figure 5.4 Viscosity of Glycerine and Dow Silicone Fluid #F-200, 1000 cs.

The secondary orifice and the third chamber should not have had an appreciable effect on the pressure in the second chamber because of the large difference in orifice diameter.

A check on Reynolds number for the flow through these throttling tubes shows that the flow must have been laminar, so that the foregoing analysis is valid.

The upper 40 inches of the glycerine-containing pipe was filled with the silicone oil so that all fluid flow in the throttling system was silicone oil flow.

d. Predicted Pressures at Transducers. The pressure pulse at the top of the fluid pipes will be delayed by the travel time of the pulse up the fluid. In the silicone-filled pipe the pressure pulse will at first be carried along by the ground stress wave out to 15 feet in about 1 msec. The time to traverse the remaining 60 feet will be (60)(30.48)/120 = 15.2 msec, which gives a pressure arrival time of 16.2 msec.

In the glycerine-filled pipe the shock will travel out of the NM and through the Dow MS-80-25 in about 1.2 msec. The glycerine travel time will be $(53\frac{2}{3})$ $(30.48)/190 = 8.6$ msec, and the 40 inches of silicone oil will delay the signal 0.8 msec more, totalling 10.6 msec.

The dimensions and calculated time constants of the four orifice systems are given in Table 5.1. The pressure in the second chamber is calculated by numerically integrating the relation $dP/dt = (P_1 - P_2)/t_c$, from a given P_1 history. The pressure history in the third chamber is obtained by repeating this process, using the previously calculated pressure history P_2.

The pressure history, P_1, is assumed to be that as obtained from SOC machine calculations, but limited in peak pressure to 1.5 kbars in the silicone oil and to 5 kbars in the glycerine, and delayed 16.2 msec in the silicone oil pipe and 10.6 msec in the glycerine pipe.

Figure 5.5 gives the resulting synthesized pressures. It is observed that these throttling systems do attenuate the early high pressure pulse and, also, that at late times the pressures in the three locations become equalized.

TABLE 5.1 PARAMETERS OF CAVITY PRESSURE THROTTLING SYSTEMS

	Glycerine-filled Pipe	Silicone Oil-filled Pipe
Diameter of First Orifice, in.	0.0670	0.0995
Length of First Orifice, in.	2.25	2.25
Volume of Second Chamber, in^3	9.17	9.17
Calculated Time Constant, msec	10.6	7.11
Observed Time Constant, msec	11	10.75
Diameter of Second Orifice, in.	0.020	0.031
Length of Second Orifice, in.	1.06	1.06
Volume of Third Chamber, in^3	0.1965	0.256
Calculated Time Constant, sec.	13.45	12.3
Observed Time Constant, sec	7	11

5.2.3 Subsurface Motion Measurement Experimental Procedure. In order to observe the late vertical motion of subsurface material at two different points, two push rods were installed which extended vertically from these subsurface points up through the surface of the ground. The lower ends of these rods were anchored into the medium so that the vertical motion of the anchor points would be indicated by the

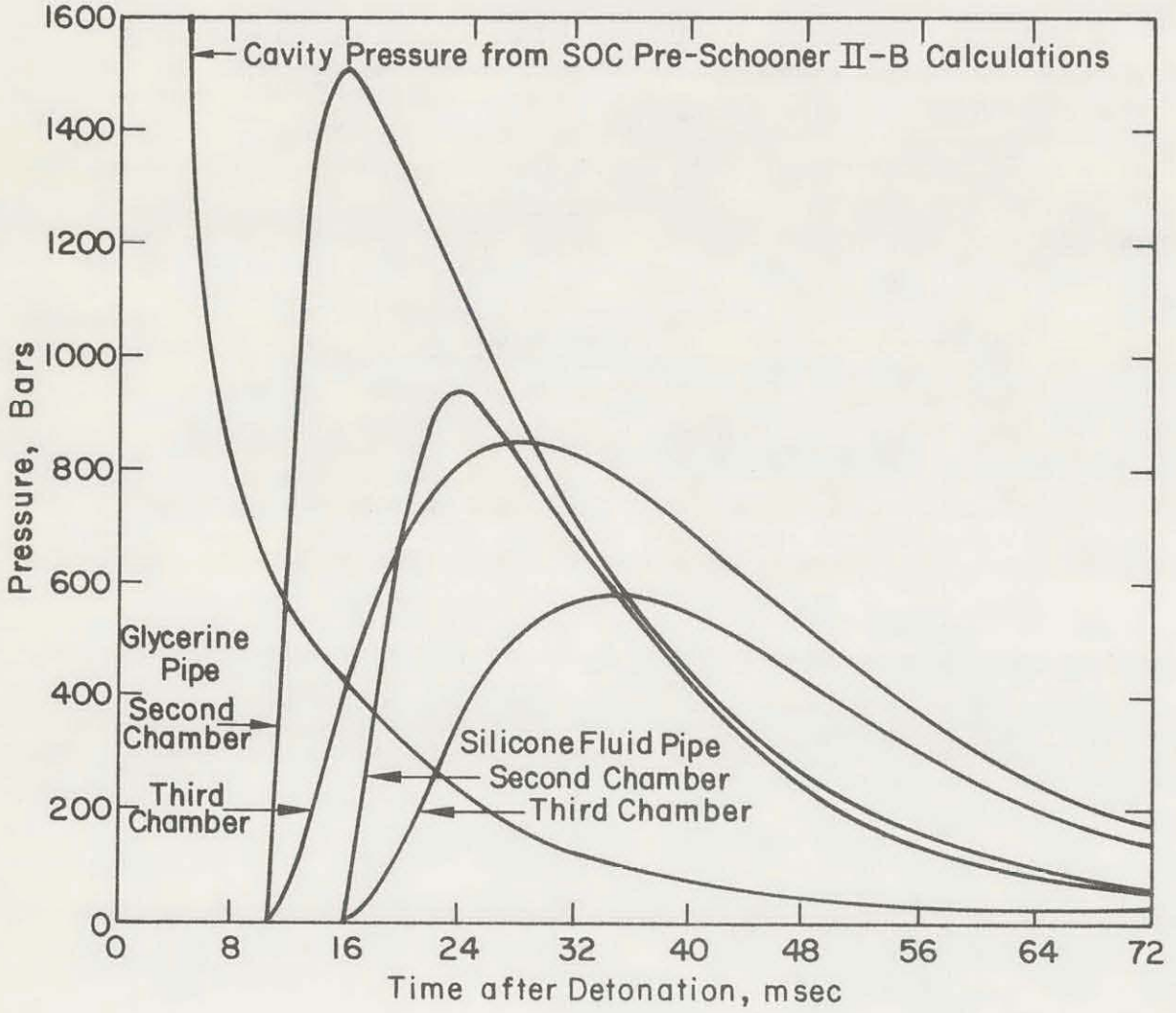

Figure 5.5 Predicted Pressures at Cavity Pressure Transducers.

vertical motion of the exposed upper ends of the rods. These rods were installed close to the shot hole (Figure 5.6), 10 feet on either side, to minimize lateral motion.

Each push rod assembly consisted of a 3-inch-diameter solid steel rod with an expansion anchor on the bottom end and a flare at the top. It had been intended to expand the anchors into under-reamed hole sections 24 inches in diameter, but because of difficulties encountered in under-reaming, the anchors were expanded to the final diameter of the under-reamed sections of about 15 inches. The anchor point in hole I-1 was 49 feet 1 inch below grade and that in hole I-2 was 28 feet 10 inches below grade. The rods themselves were coated with grease all the way to the surface during installation to promote easier sliding of the rod through the grout and rock during cavity expansion. Both holes were grouted up to the surface.

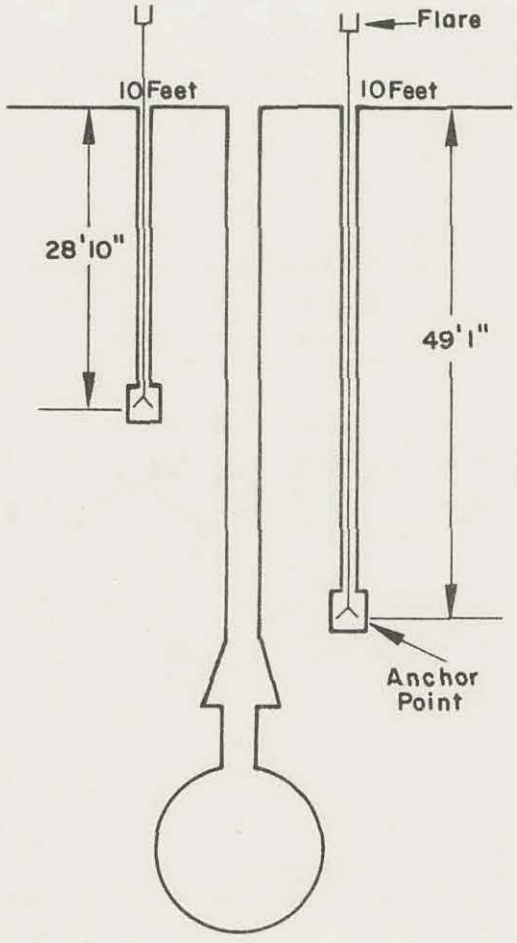

Figure 5.6 Push Rod System Geometry.

5.2.4 Method for Measurement of Temperature of Venting Gas. An effort was made on Pre-Schooner II to determine by a photographic technique the temperature of the gas vented during the cratering. In a cratering event the vented gas carries with it a suspension of solid particles, and these particles radiate approximately in a black-body spectrum. At a high enough temperature this suspension will become luminous, and photographic determination of the intensity of this emitted light will give an indication of the temperature of the suspension.

For a NM cratering event, at vent time the temperature of the burned gases should have dropped to a point where the suspension no longer emits visible light. Consequently, on Pre-Schooner II, photography was accomplished with infrared sensitive film so that lower temperatures could be measured.

Motion picture exposures were made with two different cameras located at the CP photographic station 3380 feet from GZ. One camera, operating at 1000 frames per second, was used with high-speed infrared 16-mm film with a Wratten W87 filter, while the other camera, operating at 100 frames per second, was used with Eastman 5210 infrared film with the same type filter.

5.3 RESULTS AND DISCUSSIONS (Reference 2)

5.3.1 Stress Wave Measurements in Horizontal Direction

a. Radial Stress Histories. The observed stress histories for the four tourmaline stress transducers in the horizontal array are given in Figure 5.7. The

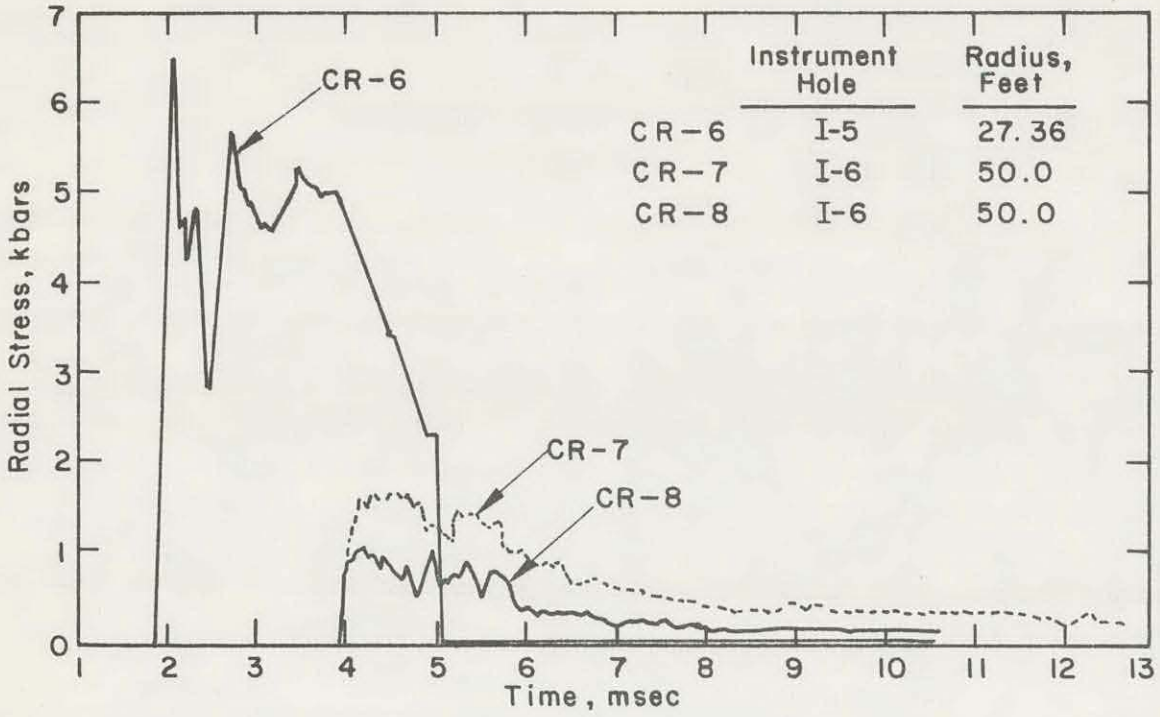

Figure 5.7 Observed Radial Stress Histories in Horizontal Array.

lower transducer, located 27.36 feet from the shot point, indicated a shorted signal soon after the stress wave arrived, while early failure did not occur for the other transducers.

The measured peak stress is compared with the results of the SOC machine prediction calculation Pre-Schooner II-D in Figure 5.8. The SOC calculation

was made for an energy release of 100 tons of NM, while the actual weight of NM detonated was 85.5 tons. When a correction is made for this difference in designed versus actual charge weight by translating the SOC curve in the direction of smaller radius by a factor of $(100/85.5)^{1/3}$, the agreement is seen to be quite good for two of the three experimental points.

The measured stress 50 feet from shot point and 69 feet below the surface is much lower than that from the transducer 4 feet deeper. It is believed that this is an actual stress difference and not an experimental error. Such a discrepancy might conceivably have arisen from the presence of porous rock in the vicinity of the upper transducer which would result in lower stresses in that area.

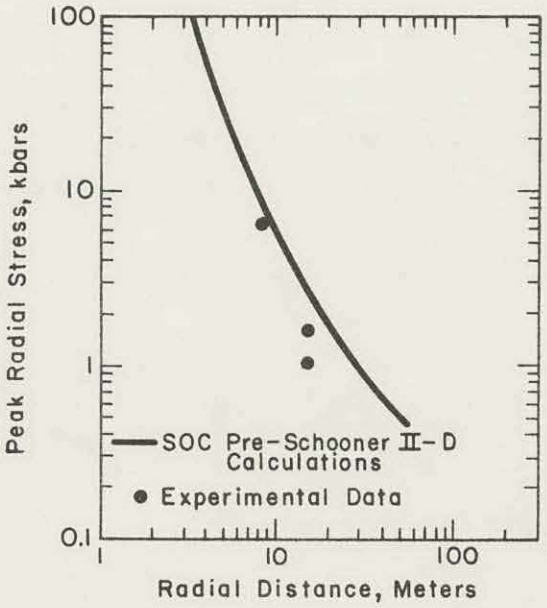

Figure 5.8 Comparison of Experimental with Computed Peak Radial Stress in Horizontal Direction.

The emergence of the elastic precursor from the stress wave is shown in Figure 5.9. It is observed that this elastic component has an amplitude of the order of a kbar but that the medium was probably not homogeneous enough to permit a more precise determination of a maximum wave amplitude.

b. Shock Arrival Time Measurements. Shock arrival time in the horizontal direction was determined from the observed signal arrival times at: (1) the four tourmaline stress transducers in holes I-5 and I-6, (2) the lowest ferroelectric switch in hole I-4, and (3) the accelerometers in holes I-7 and I-8. Table 5.2 presents a tabulation of shock time of arrival in the horizontal direction.

A graphical presentation of the data is given in Figure 5.10 together with the SOC Pre-Schooner II prediction calculation curve. It is pertinent to note the close agreement between the SOC predicted curve and the results.

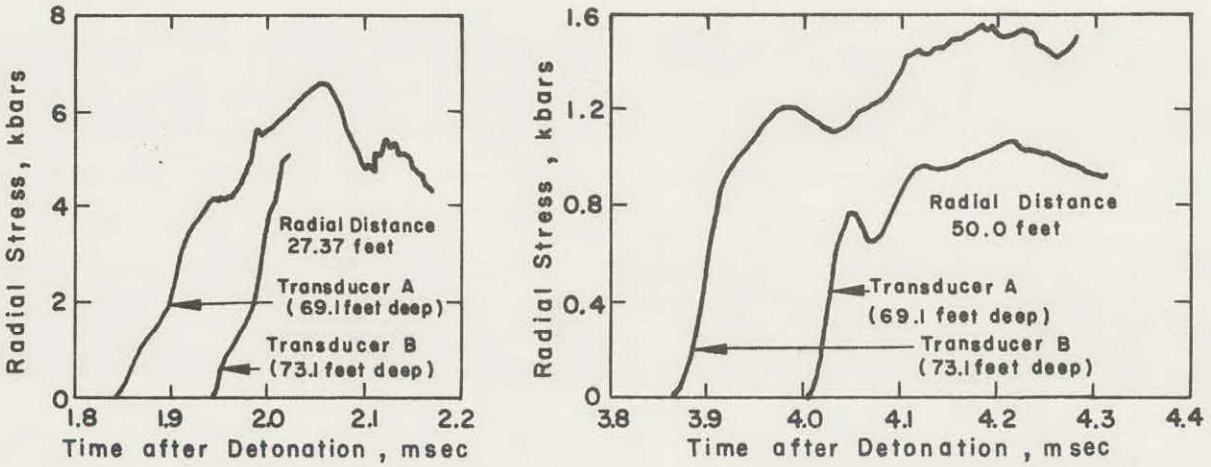

Figure 5.9 Observed Leading Edges of Stress Waves in Horizontal Array.

TABLE 5.2 GROUND STRESS TIME OF ARRIVAL IN HORIZONTAL DIRECTION

Gage Type	Instrument Hole	Gage Radius	Time of Arrival
		ft	msec
Tourmaline Pressure History	I-5	27.36	--
Tourmaline Pressure History	I-5	27.36	1.84
Tourmaline Pressure History	I-6	50.00	3.85
Tourmaline Pressure History	I-6	50.00	3.96
Vertical Accelerometer	I-7	99.4	9.5
Radial Accelerometer	I-7	99.4	9.5
Vertical Accelerometer	I-8	201.00	21.0
Radial Accelerometer	I-8	201.00	21.0

5.3.2 Stress Wave Measurements in Vertical Direction

a. Radial Stress Histories. The observed stress histories for the vertical array of piezoelectric transducers are given in Figure 5.11. These histories show the degradation of the stress front as the stress wave moves outward and the emergence of the elastic precursor. The stress wave broadens as it moves out but when it approaches the surface the rarefaction wave from the surface relieves the stress and by so doing limits the width of this stress wave.

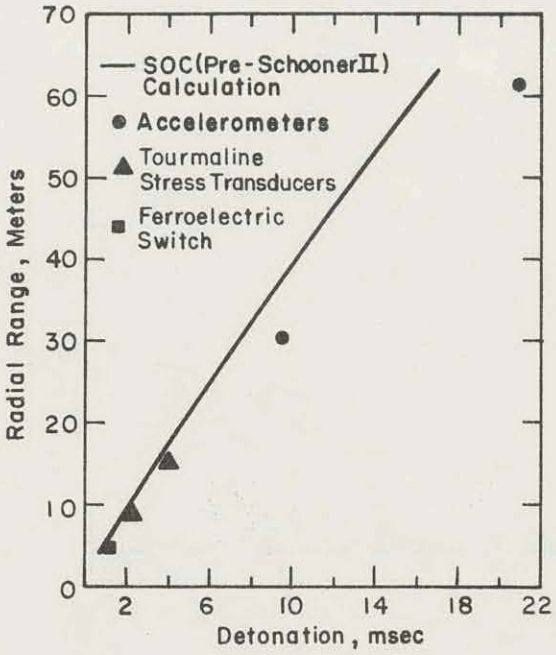

Figure 5.10 Signal Arrival Times in Horizontal Array.

The transducer 59.2 feet from the explosion center was located 13.66 feet below the surface of the ground. Stress wave velocity in this region was quite low, probably of the order of 5000 ft/sec. Consequently, the unloading wave should begin to arrive some 5 msec after incidence of the stress wave. The observed width is in rough agreement with this estimate.

The transducer 39.4 feet from the explosion center was located 34.6 feet below the surface of the ground. In this case, stress unloading should occur at (2) (34.6)/6 = 12 msec after the onset of the stress wave. This unloading wave should have been considerably attenuated by energy loss in compaction and by radial divergence, however, so that is would not have been expected to unload the incident stress wave completely. It is not clear whether the observed signal indicates this effect. Other data show that a spall occurred at about 16 msec 26 feet below the surface of the ground. This spall ruptured the signal cable at this time, while leaving intact the signal cable to the transducer 13.66 feet deep.

The measured peak stresses are compared with the SOC Pre-Schooner II-B calculation in Figure 5.12. The measured points fall considerably below the SOC curve

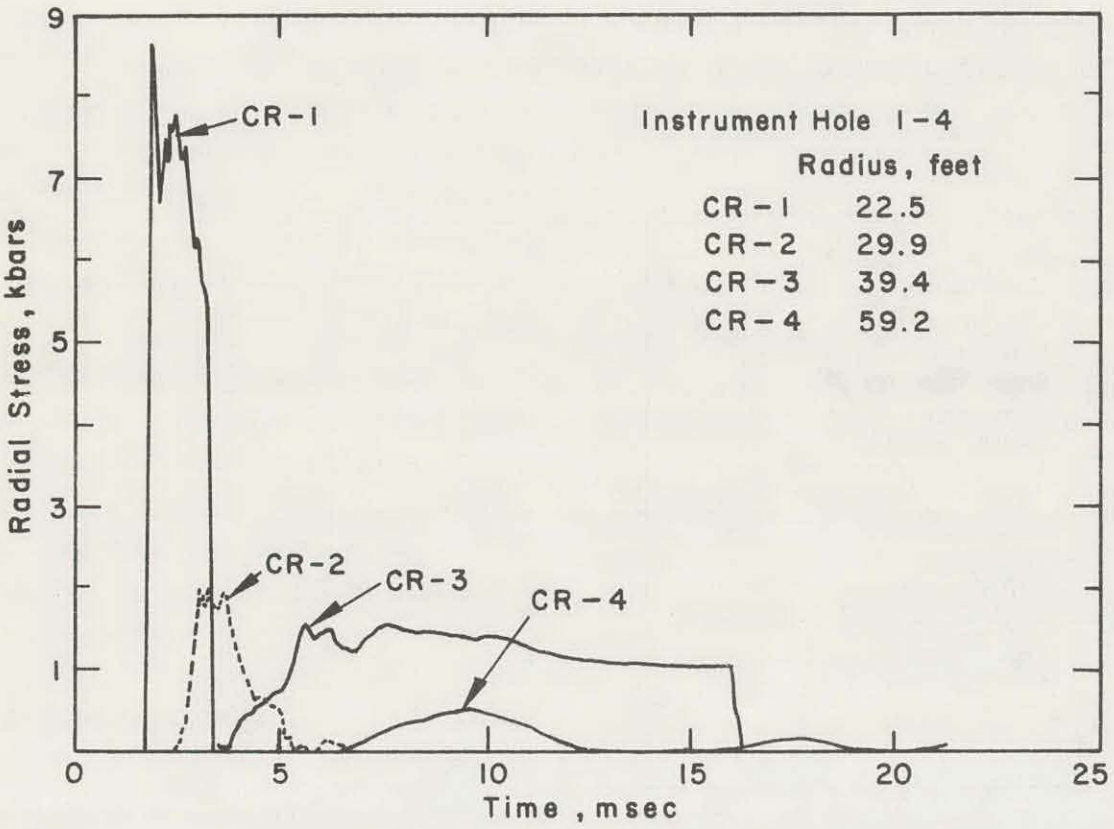

Figure 5.11 Observed Radial Stress Histories in Vertical Array.

and, in addition, show considerable scatter. It is believed that the scatter in the experimental points is caused by the heterogeneous nature of the medium above shot depth and that the experimental curve falls below the calculated curve because the medium was more porous and compressible than had been assumed for the SOC calculations.

The emergence of the eleastic precursor from the stress wave moving in the vertical direction is shown in Figure 5.13. This phenomenon seems to be more irregular than in the horizontal direction and is probably also caused by the presence of friable zones and layers above shot depth.

b. Shock Arrival Time Measurements. The close-in ferroelectric switches showed only a sudden single pulse, while those farther out showed the arrival of both the elastic and the inelastic components as distorted by the differentiating effect of the mixer circuit.

The arrival times of the elastic precursors in the vertical direction are given in Table 5.3, and are plotted in Figure 5.14, along with other arrival time data. There is a rather wide scatter in the experimental points. It is believed that this scatter was caused by the heterogeneous nature of the medium.

The curve developed from the conventional slifer system data is also plotted in Figure 5.14. This slifer curve agrees with the other points at small radii. Farther from the shot point, however, the observed slifer arrival time was later than that from the other transducers because the crushing of this cable required a higher stress level than was required to give a signal on the other transducers.

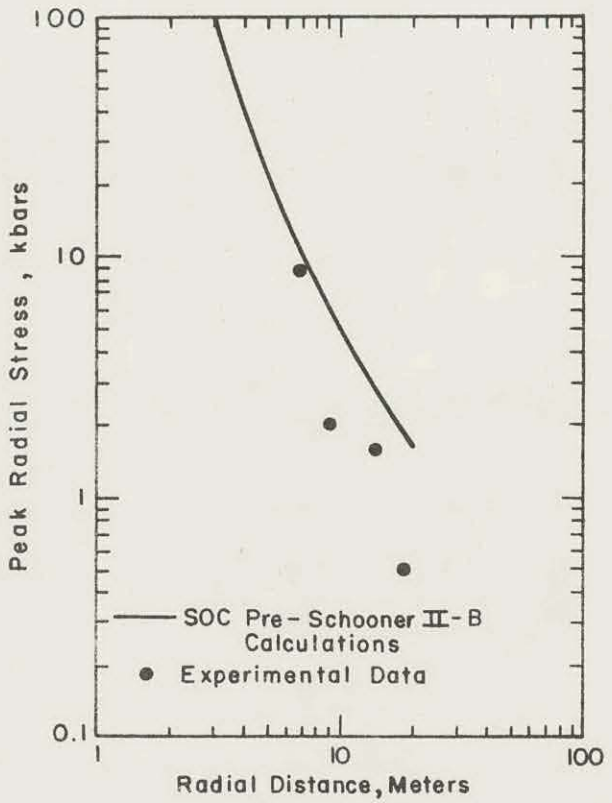

Figure 5.12 Comparison of Experimental with Computed Peak Radial Stress in Vertical Direction.

The slifer curve was smoothed out to the radius of about 30 feet, while beyond this radius the curve became jagged. This condition implies that the rock and the grout around the cable failed in a fine-grained manner out to 30 feet, where the radial stress had dropped to 2 or 3 kbars, but farther out where the stress was lower the medium failed in much larger chunks.

5.3.3 Subsurface Spall Measurements. Figure 5.15 presents the experimental results of the dual-mode slifer system located in hole I-4. This system did not oscillate at all times. The periods of nonoscillation may have been caused by imperfect shorting of the cable.

It may be noted from Figure 5.15 that a subsurface spall occurred approximately 26 feet below the surface at 18 msec after shot time. This same spall probably caused the cable failure on the tourmaline transducer 34.6 feet below the surface at 16 msec, while no such failure was observed on the next higher tourmaline transducer 13.66 feet below the surface, which was above the separation zone.

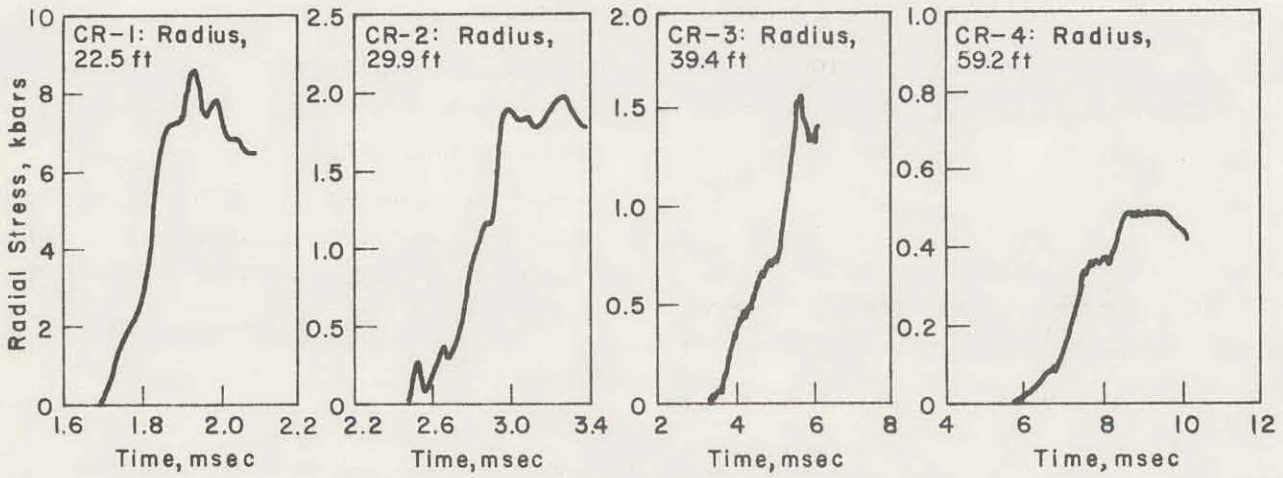

Figure 5.13 Observed Leading Edges of Stress Wave in Vertical Array.

TABLE 5.3 GROUND STRESS TIME OF ARRIVAL IN VERTICAL DIRECTION
Instrument Hole I-4

Gage Type	Gage Radius	Time of Arrival
	ft	msec
Ferroelectric Switch	15.28	0.912
Ferroelectric Switch	16.2	1.01
Ferroelectric Switch	20.0	1.48
Tourmaline Pressure Profile	22.5	1.71
Ferroelectric Switch	24.9	2.03
Tourmaline Pressure Profile	29.9	2.45
Ferroelectric Switch	34.9	3.09
Tourmaline Pressure Profile	39.4	3.46
Ferroelectric Switch	44.8	3.67
Ferroelectric Switch	55.0	5.23
Tourmaline Pressure Profile	59.2	5.61
Ferroelectric Switch	64.9	(?)
Vertical Accelerometer[a]	69.0	6.9

[a]Contained in Instrument Hole I-3.

At 95 msec after shot time the slifer cable became shorted at a point 12 feet below the surface. This shorting is probably due to late earth motion and is probably not of particular significance.

5.3.4 Acceleration Measurements. The vertical acceleration observed at the accelerometer located in hole I-3, 9.8 feet below the surface of the ground, is shown in Figure 5.16. This curve indicates the presence of a low amplitude precursor and a later arrival of the main stress wave which is in rough agreement with the stress history as measured with the tourmaline transducer 13.66 feet below the surface (only some 4 feet deeper). Only positive accelerations are observed, as should be the case for an accelerometer so near the free surface in a medium without significant tensile strength.

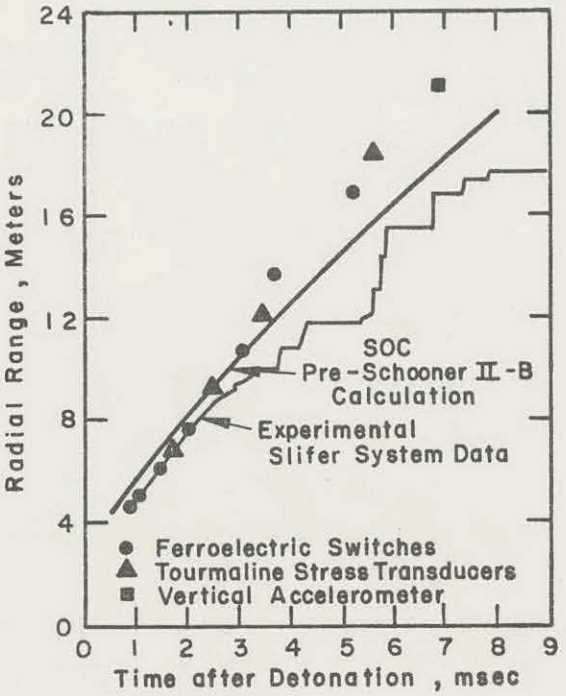

Figure 5.14 Signal Arrival Times in Vertical Direction.

The accelerometers located at shot horizon in hole I-7, 99.4 feet from the detonation point, gave only a stress arrival time and possibly the beginning of the acceleration curve which is not presented in this report.

The accelerometers located at shot horizon in hole I-8, 201 feet from the detonation point, gave signals as presented in Figure 5.17. These systems gave improbable results soon after the beginning of the negative half of the cycle. The vertical accelerometer seems to have measured a small component of the horizontal acceleration with no evidence of an independent vertical acceleration.

5.3.5 Cavity Pressure Experimental Results. Pressure signals were obtained from the Photocon transducer and the upper tourmaline transducer in the glycerine pipe system and from the Norwood transducer and the upper tourmaline transducer in the silicone oil pipe system. Both tourmaline crystal transducers located near the tops of the pipes but beneath the first orifices gave only signal arrival times before failure.

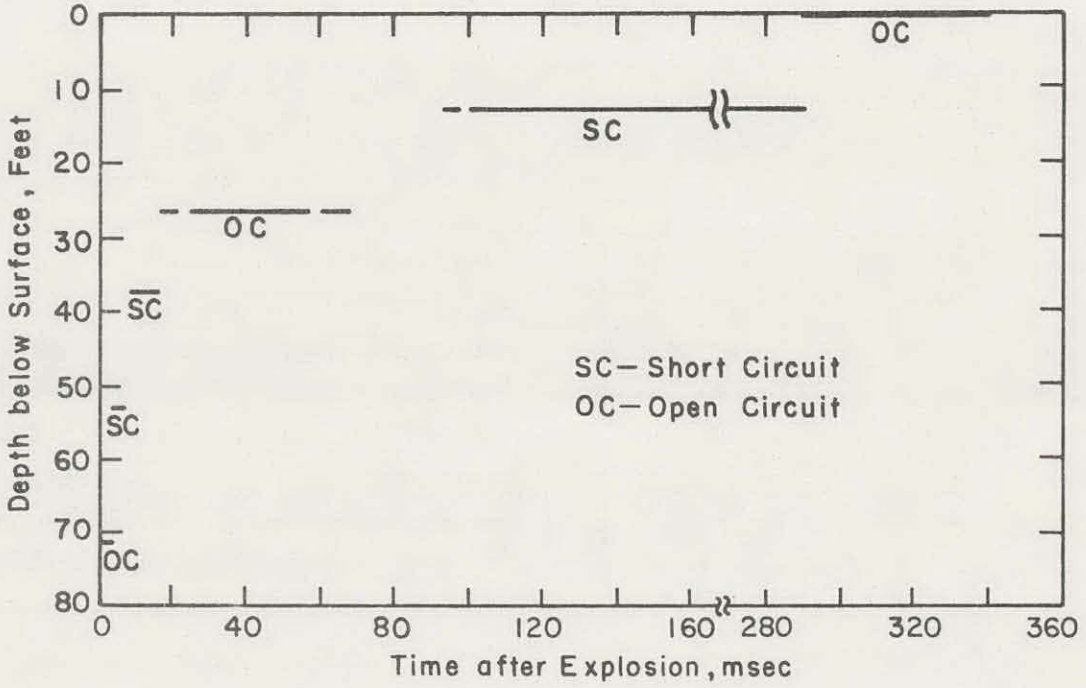

Figure 5.15 Results from Dual-Mode Slifer Showing Times of Cable Failure.

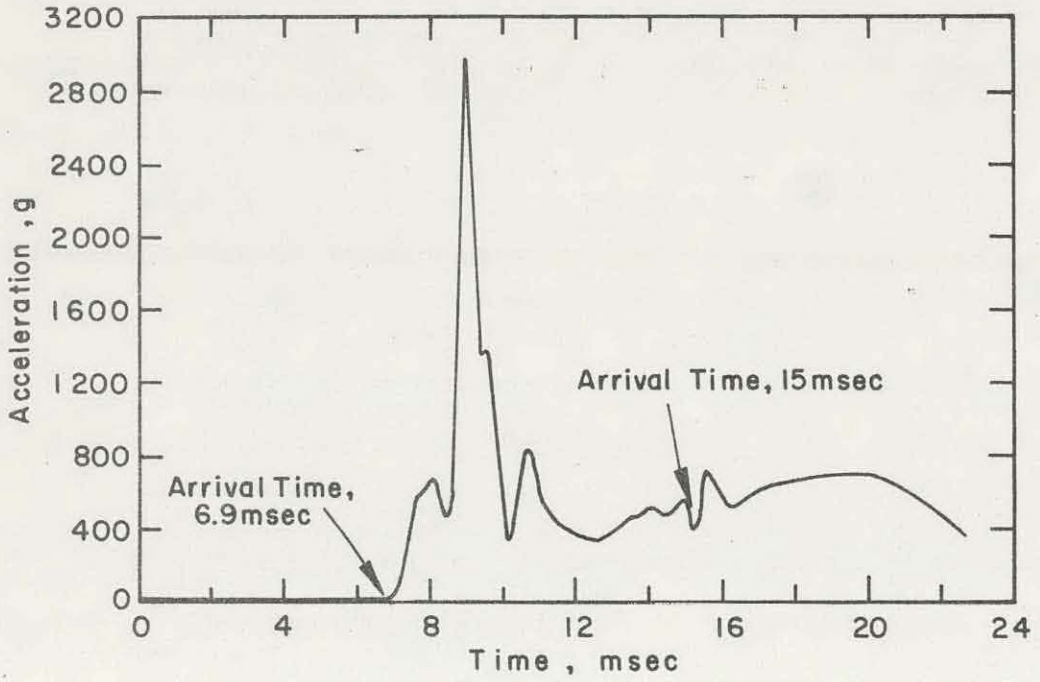

Figure 5.16 Observed Vertical Acceleration in Hole I-3, 9.8 Feet Below Surface of Ground.

The signals from the Photocon gauge and the tourmaline transducer in the second chamber of the glycerine pipe system are given in Figure 5.18. Also presented in this figure are the pressures in the second chamber, as calculated from the Photocon signal using a time constant of 11 msec, and the pressure at the upper end of the pipe, as calculated from the tourmaline signal using a time constant of 7 msec. These time constants were determined from the rate of decay of the signal after the pressure in the preceding chamber had apparently dropped essentially to zero. The observed and the synthesized signals in the second chamber agree quite well.

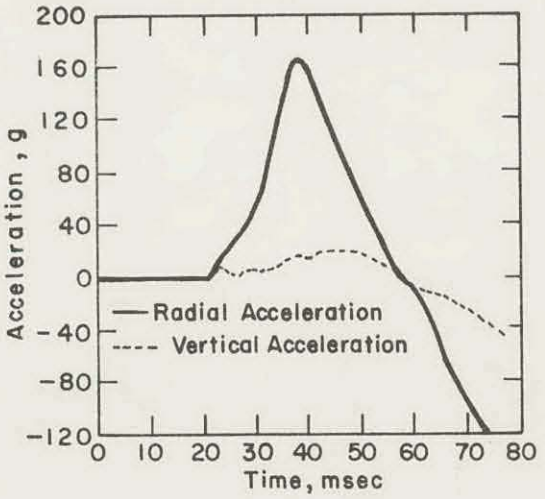

Figure 5.17 Observed Acceleration 201 Feet from Shot Point at Shot Depth.

The pressure in the third chamber of the silicone oil system as measured with the Norwood gauge is given in Figure 5.19, along with the pressure derived from this one in the second chamber and at the top of the silicone oil pipe, using time constants of 10.75 and 11 msec for the second and first orifices, respectively. The signal from the tourmaline transducer in the second chamber was defective and is not presented in this report.

The results obtained are fairly self-consistent and indicate that the peak pressure at the top of the glycerine pipe was of the order of 2000 bars while that at the top of the silicone oil pipe was of the order of 1500 bars. Loss of pressure in the glycerine pipe occurred at 16 to 18 msec after shot time and at some 20 to 23 msec after shot time in the silicone oil pipe.

Field examination of the pipes after the shot showed that the pipes had been badly buckled by end thrust and had probably been broken by this type of motion and possibly by subsurface spall rather than by internal pressure. Early pipe failure, with loss of pressure into the surrounding rock, seems to be the reasonable explanation for the observed results.

The original purpose of this phase of the program had been to measure cavity pressure at very late times. This goal was not achieved because of the pipe failure. It is concluded that more massive, larger diameter pressure pipes should have been used.

The pressures as read over the abbreviated time interval agree quite well with those predicted. The measurements are dependent upon the values chosen for the

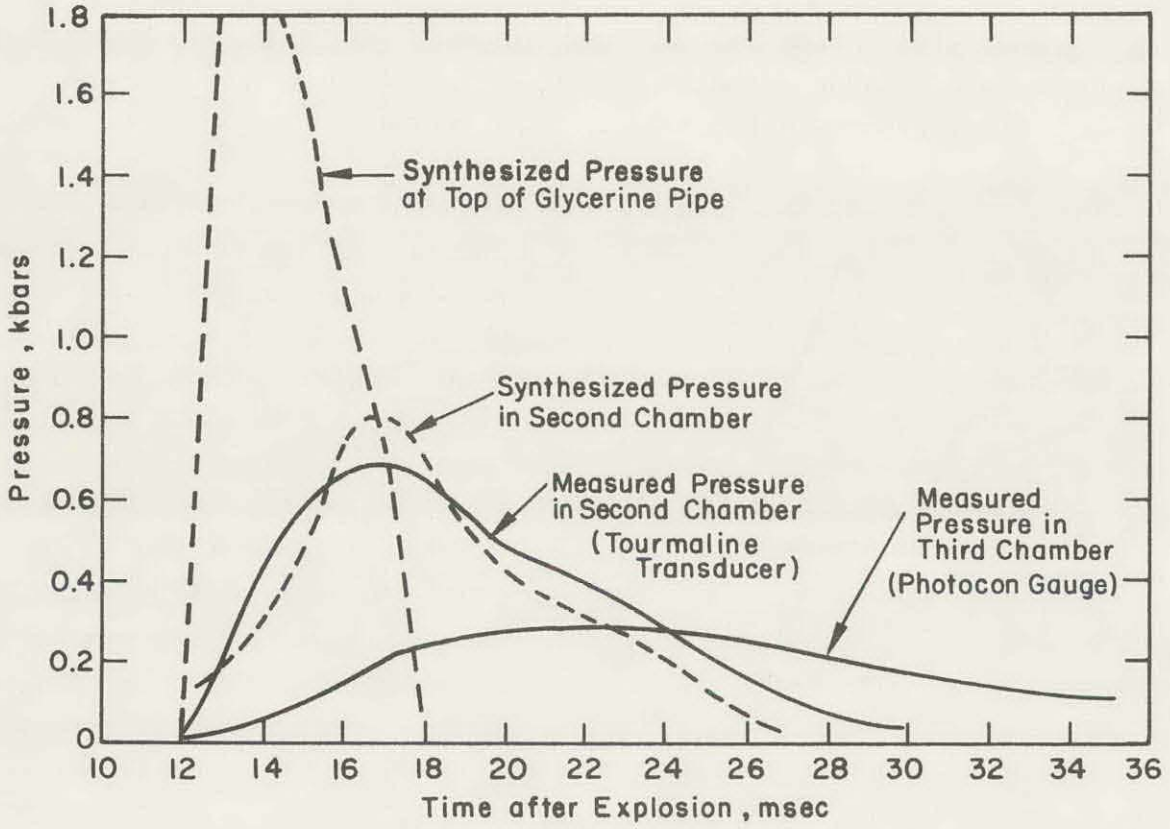

Figure 5.18 Pressures in Glycerine Pipe System.

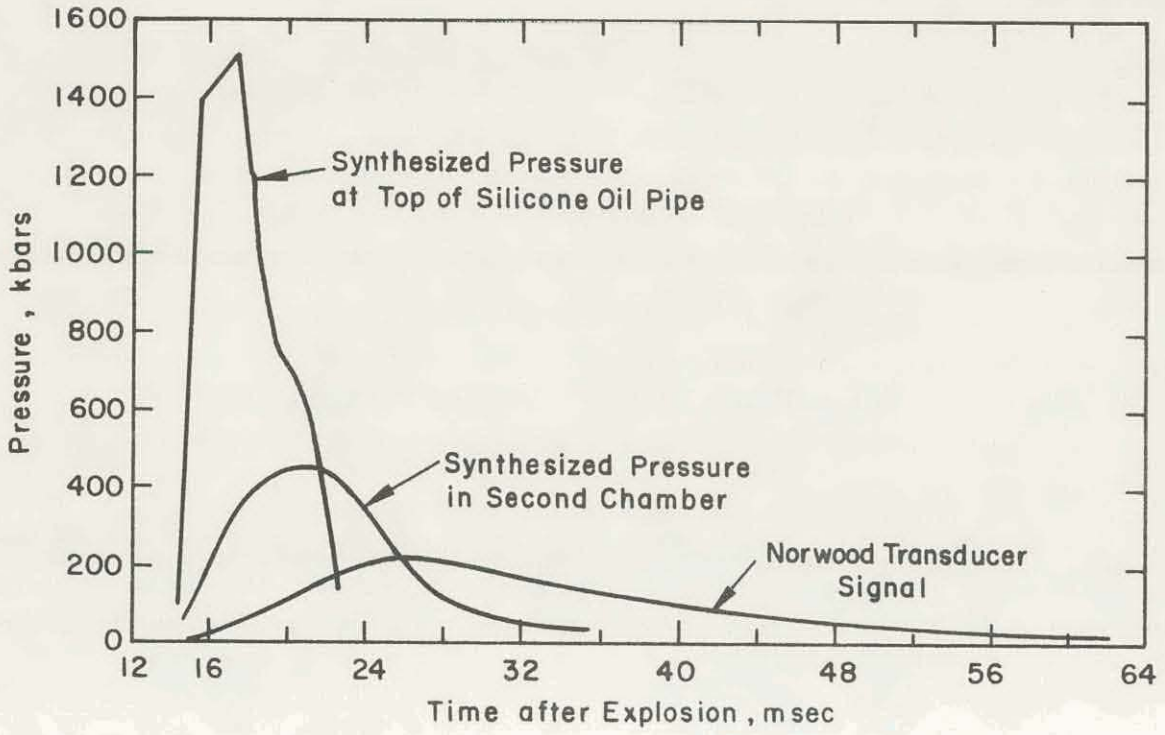

Figure 5.19 Pressures in Silicone Oil Pipe System.

time constants over such a short time interval. Over the longer time interval that measurements were being attempted (several time constants long) the transient effect involving the time constants would have been unimportant. Assuming linear systems, the area under the pressure-time curve for each transducer of a pipe system should be the same. The signals obtained give self-consistent results in this regard.

Signal arrival times are given in Table 5.4 and are compared with the predicted times. The arrival times for the glycerine pipe are in good agreement but in the

TABLE 5.4 CAVITY PRESSURE SYSTEM SIGNAL ARRIVAL TIMES

	Glycerine-filled Pipe	Silicone Oil-filled Pipe
	msec	msec
Predicted	10.6	16.2
Observed:		
Upper end of pipe (tourmaline)	10.7	13.3
Second chamber (tourmaline)	11.5	14.4
Third chamber (Photocon and Norwood)	11.7	14.6

silicone oil pipe the observed signals arrived considerably earlier than predicted. Presumably at higher pressures the pulse velocity in the silicone oil increases considerably.

5.3.6 Subsurface Motion Measurement Results. The flares mounted at the top of the push rods were not used during the Pre-Schooner II detonation, but other motion picture records show that the top ends of the push rods moved earlier and faster than the ground surface. These top ends did not move as fast as they should have, however, if they were to indicate true motion of the anchor points.

The 30-foot rod assembly was found and inspected after the shot. The fact that this rod was rather badly buckled indicated that it probably did not slide upward smoothly through the rock. This buckling may have been caused or accentuated by the irregular nature of the medium in which voids may have been closed by lateral motion of the rock.

The 10-foot section of casing originally located at the top of this push rod hole, along with the grout inside it, remained attached to the push rod. The push rod had

moved through it a total of only some 3 feet before the casing was carried along with the rod. The fact that only portions of the 50-foot push rod system were found indicate that the system failed at an early time.

It is concluded that the motion of the upper ends of the rods did not correspond with the motion of the lower ends. The rods were too small in diameter to withstand the buckling and other lateral forces present.

5.3.7 Planned Procedure for Measurement of Venting Gas Temperature. It is planned to calibrate the infrared sensitive film used during the Pre-Schooner II detonation to obtain venting gas temperature measurements by exposing equivalent film to a tungsten ribbon filament of various known temperatures. This calibration work has not been completed to date, nor has the temperature experiment shot film been developed. The results of this portion of the technical program will be included in the final report (Reference 1).

REFERENCES

1. M. Heusinkveld and R. Marks; "Pre-Schooner II Subsurface Effects Measurements"; PNE 515F, to be published; Lawrence Radiation Laboratory, Livermore, California.

2. M. Heusinkveld and R. Marks; "Subsurface Effects Measurements on Pre-Schooner II"; UOPKB 65-79, October 29, 1965; Lawrence Radiation Laboratory, Livermore, California.

CHAPTER 6

GROUND SHOCK MEASUREMENTS

6.1 INTRODUCTION

The Operational Safety Division of the Nevada Operations Office, U. S. Atomic Energy Commission, sponsored the Pre-Schooner II Ground Shock Measurements Program. The primary purpose of the program was to collect ground motion data which could be used to facilitate more accurate ground motion predictions for the proposed 100 kt Schooner nuclear cratering experiment. Eight seismic instrument stations were located at various distances from SGZ for the following purposes: (1) to provide a measure of the level of ground motion resulting from the Pre-Schooner II detonation, and (2) to evaluate the effects of the thick alluvium blanket in the Snake River Valley on the amplitude of the ground motion.

Roland F. Beers, Inc., was designated by the Nevada Operations Office as the responsible agency for development of the ground shock measurements technical plan and analysis and interpretation of the results. The U. S. Coast and Geodetic Survey (USC&GS) conducted the ground shock measurements program in the field.

This chapter presents the results of an initial examination, made by Roland F. Beers, Inc., of the USC&GS ground motion recordings for the Pre-Schooner II experiment (Reference 1). The scope of this initial examination included: (1) analysis of the recordings to determine peak motions, and (2) plotting of the peak motions versus distance for comparison with predictions. No corrections are included in this chapter for motions with frequencies in the portion of the spectrum where instrument response varies with frequency. This correction as well as the derivation of acceleration and displacement from the velocity records and the derivation of velocity from the acceleration and displacement records will be included in the final report (Reference 2).

6.2 EXPERIMENTAL PROCEDURES

A total of eight recording stations were operated by USC&GS during the Pre-Schooner II experiment. The stations were located on two lines: one to the east and the other to the north.

The line to the east consisted of six stations: the closest at a distance of 2400 meters; the most distant in Twin Falls at a distance of 94.5 km. Strong-motion accelerographs, recording three components of acceleration and displacement, were

used at the two closest stations (Stations 1E and 2E). The four other stations on this line consisted of NC-21 velocity meters, each station recording three components of particle velocity.

Only two recording stations were used on the north line. The closest station (7N) was located 13 km from GZ and the distant station was placed in the town of Bruneau, about 57 km to the northwest. At each station, three components of particle velocity were recorded with NC-21 velocity meters.

The locations of all stations are shown on Figure 6.1. USC&GS also placed three-component, long-period Electro-Tech displacement meters at Stations 4E and 5E (in addition to the NC-21 velocity meters).

6.3 RESULTS

Good records were obtained at all six of the stations instrumented with the NC-21 velocity meters. At the strong-motion accelerograph stations, all three components of acceleration were recorded. However, at Station 1E, only the vertical and transverse components of displacement were recorded and at Station 2E, only radial and transverse components were recorded. No readable motions were recorded on the Electro-Tech long-period displacement meters.

Tables 6.1 through 6.3 list the peak surface motions and slant distances from GZ for each station. Peak motions are given for each component and for the resultant vector which was determined by analyzing the three components simultaneously in order to determine the absolute value of peak motion. Where only two components were recorded, a resultant vector was still computed as an approximation of the value that would be obtained had all three components been recorded.

The peak resultant vector of particle acceleration plotted versus slant distance is shown on Figure 6.2 along with the preshot prediction line. With only two data points, it is not possible to evaluate the rate of attenuation of the acceleration. However, the general level of observed motion agrees very well with the prediction line. The vertical, radial, and transverse components of acceleration were also plotted versus slant distances and are shown on Figures 6.3 through 6.5, respectively.

The peak resultant vector of displacement is plotted versus slant distance on Figure 6.6. The prediction line is also shown for comparison. As with the acceleration data, only two measurements of displacement are available and no conclusion can be made about the rate of attenuation.

The level of motion is higher than predicted by a factor of about 3 at Station 1E and about 1.5 at Station 2E. In Figure 6.7 the transverse component of displacement is plotted versus slant distance. Graphs for vertical and radial displacement are not included because only one value was obtained for each of these components.

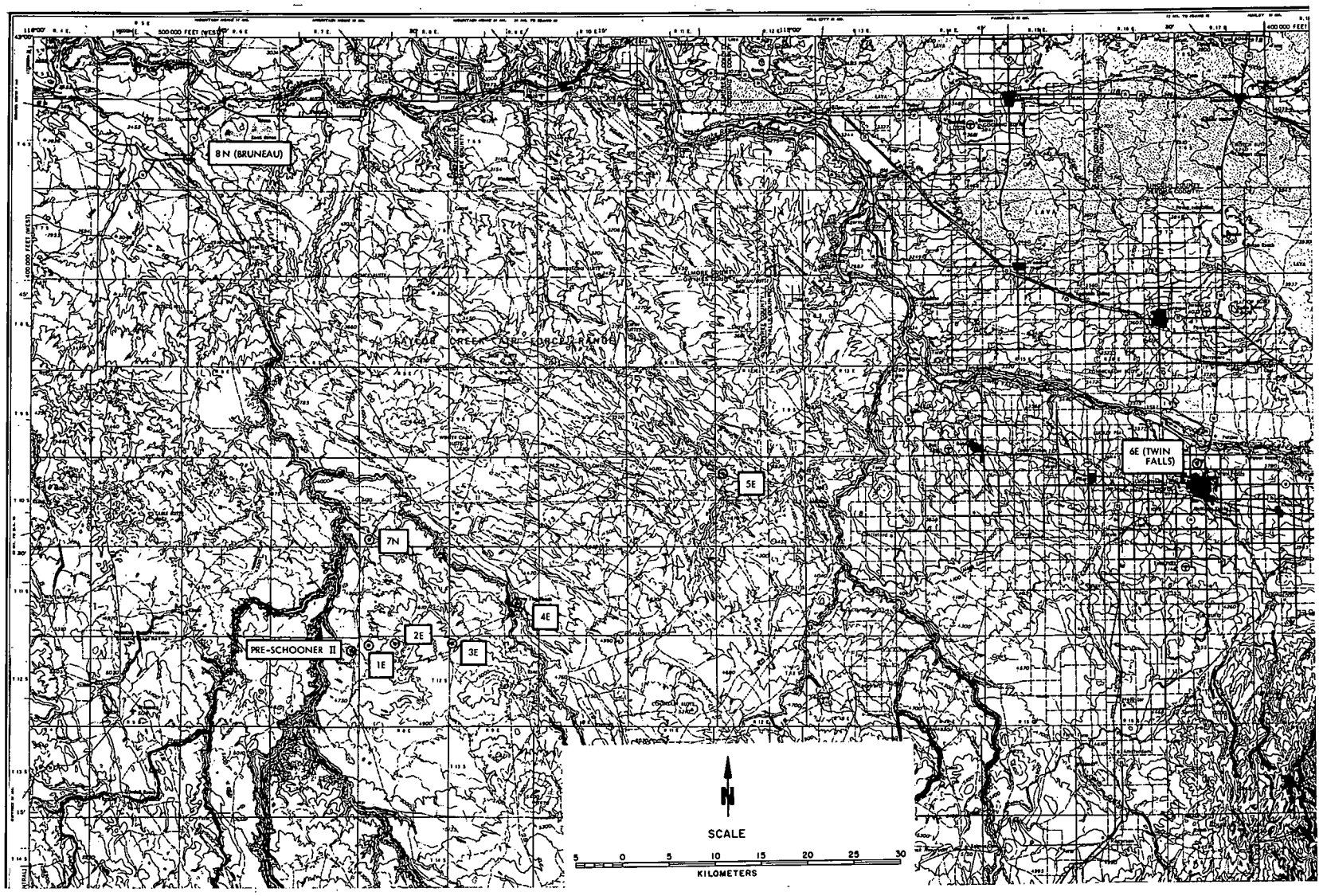

Figure 6.1 Seismic Instrument Station Location Map.

TABLE 6.1 PEAK SURFACE PARTICLE ACCELERATION

Station	Slant Distance	Bearing from GZ	Acceleration			
			Vertical	Radial	Transverse	Resultant Vector
	meters		g	g	g	g
1E	2400	N79° E	0.0108	0.0127	0.00643	0.0133
2E	4720	N79° E	0.00348	0.00597	0.00413	0.00699

TABLE 6.2 PEAK SURFACE PARTICLE DISPLACEMENT

Station	Slant Distance	Bearing from GZ	Displacement			
			Vertical	Radial	Transverse	Resultant Vector
	meters		cm	cm	cm	cm
1E	2400	N79° E	0.119	--	0.0120	0.120
2E	4720	N79° E	--	0.0171	0.0116	0.0184
4E	18890	N72° E	--	--	--	--
5E	44650	N64° E	--	--	--	--

TABLE 6.3 PEAK SURFACE PARTICLE VELOCITY

Station	Slant Distance	Bearing from GZ	Velocity			
			Vertical	Radial	Transverse	Resultant Vector
	meters		cm/sec	cm/sec	cm/sec	cm/sec
3E	10700	N82° E	0.0940	0.0841	0.111	0.124
4E	18890	N72° E	0.0338	0.0220	0.0275	0.0400
5E	44650	N64° E	0.00346	0.00250	0.00202	0.00351
6E[a]	94500	N77° E	0.000693	0.00167	0.000547	0.00171
7N	13000	N7° E	0.0279	0.0316	0.0359	0.0379
8N[a]	56800	N19°W	0.00574	0.00638	0.0106	0.0117

[a]Station 6E in Twin Falls and Station 8N in Bruneau are both on alluvium; all the other stations are on hardrock.

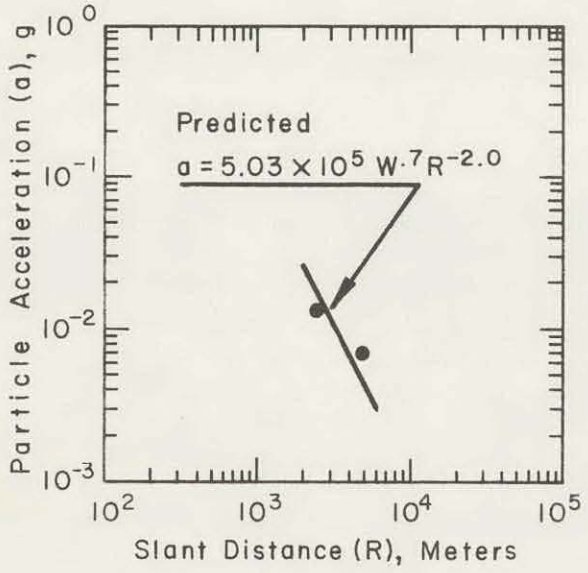

Figure 6.2 Resultant Vector of Peak Surface Particle Acceleration versus Slant Distance (94.6 tons Energy Equivalent Yield).

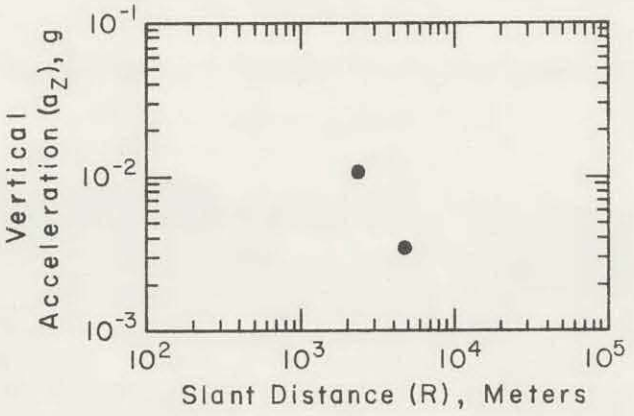

Figure 6.3 Vertical Component of Peak Surface Particle Acceleration versus Slant Distance (94.6 tons Energy Equivalent Yield).

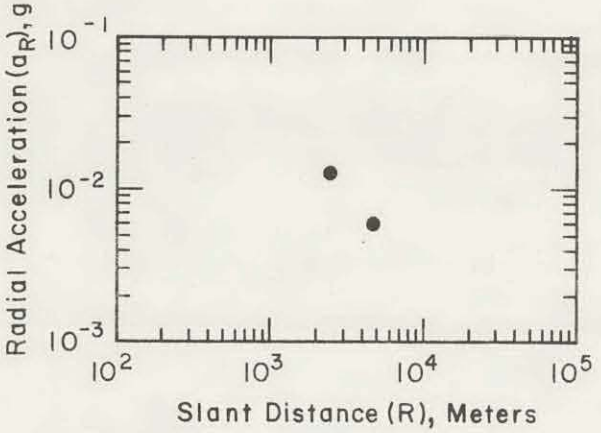

Figure 6.4 Radial Component of Peak Surface Particle Acceleration versus Slant Range (94.6 tons Energy Equivalent Yield).

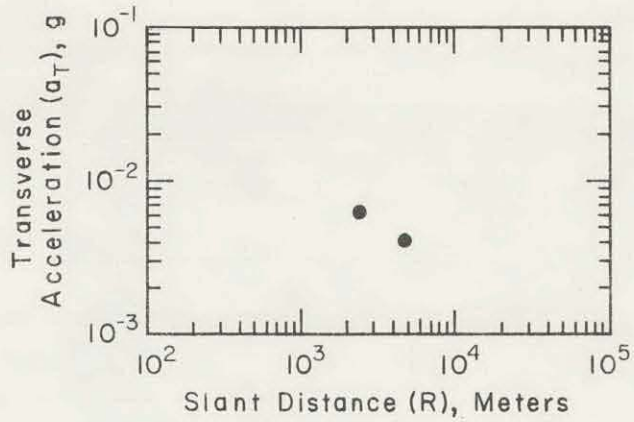

Figure 6.5 Transverse Component of Peak Surface Particle Acceleration versus Slant Distance (94.6 tons Energy Equivalent Yield).

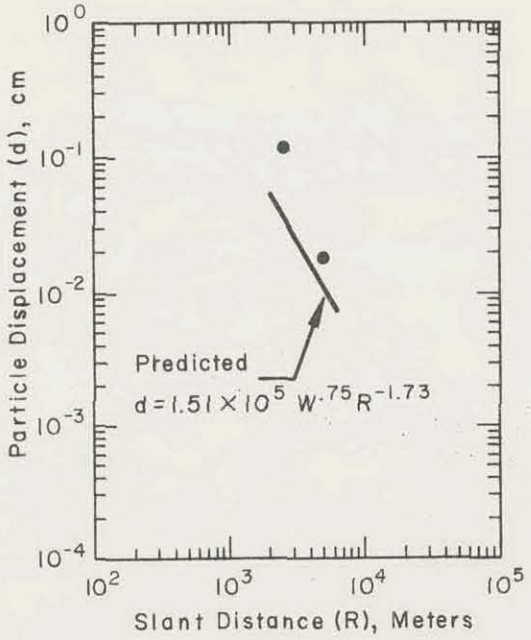

Figure 6.6 Resultant Vector of Peak Particle Displacement versus Slant Distance (94.6 tons Energy Equivalent Yield).

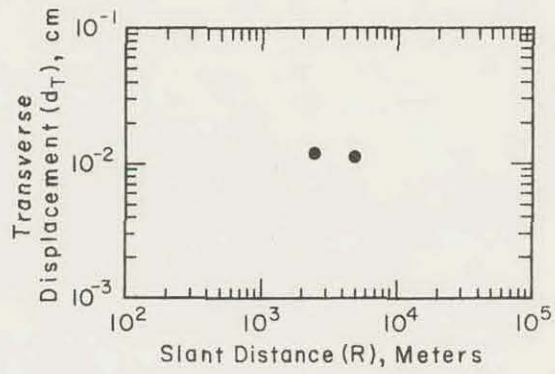

Figure 6.7 Transverse Component of Peak Surface Particle Displacement versus Slant Distance (94.6 tons Energy Equivalent Yield).

Figure 6.8 shows the peak resultant vector of particle velocity versus slant distance in comparison with the prediction lines. The closest four velocity stations were located on hardrock, either basalt or the Idavada formation, while the two most distant were located in Bruneau and Twin Falls on the thick alluvium of the Snake River Valley. Two prediction lines are shown, therefore; one for the hardrock stations and one for the alluvium. The data measured on hardrock show a rate of attenuation that is greater than predicted. However, a firm conclusion about the rate of attenuation is not justified with only four data points. The level of motion at all four stations was higher than predicted by a factor ranging from about 1.7 to 4. With only two stations on alluvium, no conclusion can be reached concerning the rate of attenuation. The observed motion at Twin Falls Station (6E)

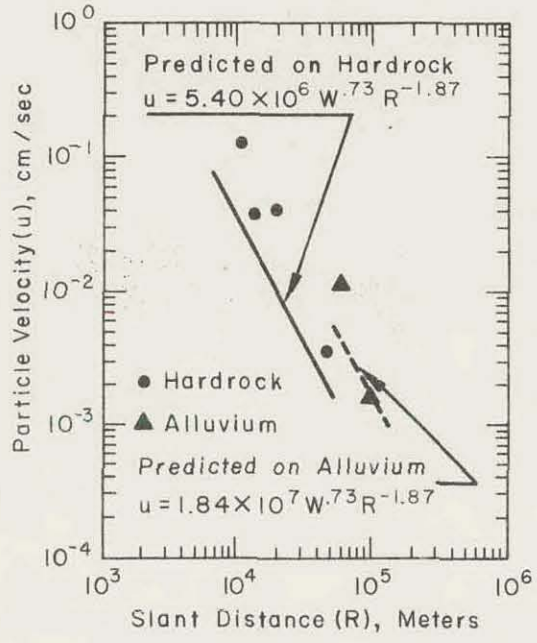

Figure 6.8 Resultant Vector of Peak Surface Particle Velocity versus Slant Distance (94.6 tons Energy Equivalent Yield).

falls exactly on the prediction line, while the motion at Bruneau (Station 8N) is approximately two and a half times the predicted value. The vertical, radial, and transverse components of particle velocity are shown versus slant distance in Figures 6.9, 6.10, and 6.11, respectively.

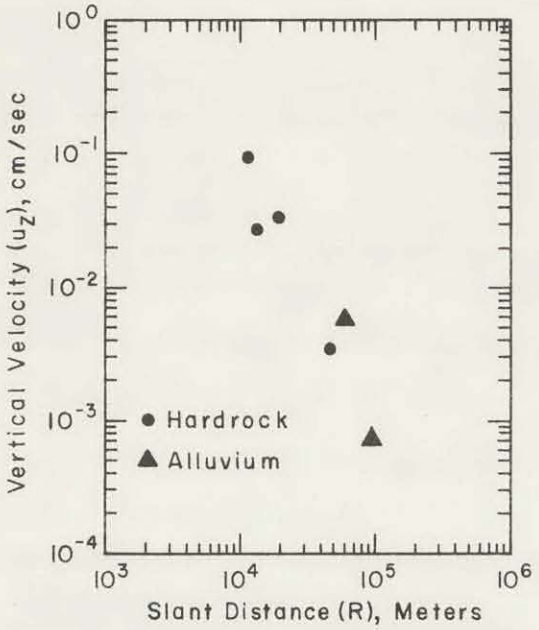

Figure 6.9 Vertical Component of Peak Surface Particle Velocity versus Slant Distance (94.6 tons Energy Equivalent Yield).

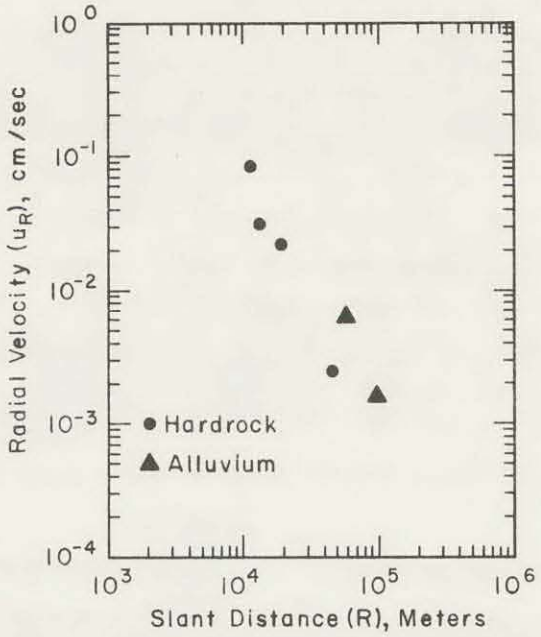

Figure 6.10 Radial Component of Peak Surface Particle Velocity versus Slant Distance (94.6 tons Energy Equivalent Yield).

6.4 CONCLUSIONS

Usable data were obtained at all eight stations. These data will be helpful in the future for making predictions for the Schooner event.

The two stations which recorded acceleration provided data which agree quite well with predictions. The observed displacements and velocities were higher than predicted.

Additional processing to correct for frequency response characteristics of the instruments and to derive accelerations, displacements, and velocities at each station will provide considerably more information. At the completion of the pro-

processing, more meaningful conclusions can be drawn, particularly concerning the significance of these results on the predicting capability for the Schooner event.

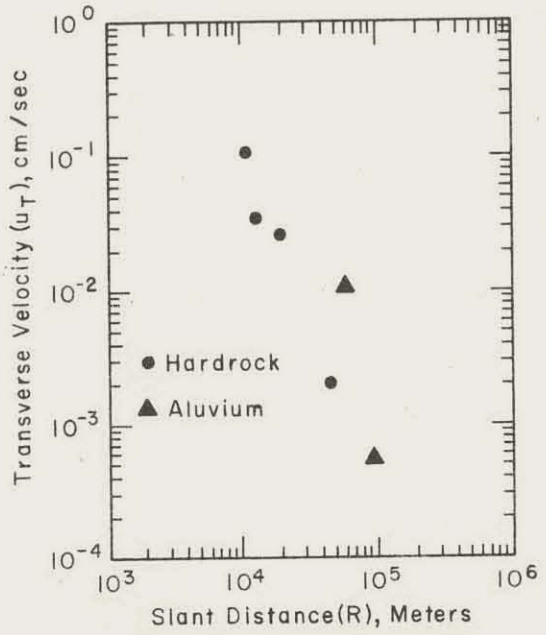

Figure 6.11 Transverse Component of Peak Surface Particle Velocity versus Slant Distance (94.6 tons Energy Equivalent Yield).

REFERENCES

1. Roland F. Beers, Inc.; "Interim Report, Pre-Schooner II"; NVO-116, October 29, 1965; Alexanderia, Virginia.

2. Roland F. Beers, Inc.; "Pre-Schooner II Ground Shock Measurements"; PNE 514F, to be published; Alexandria, Virginia.

CHAPTER 7

CLOUD DEVELOPMENT STUDIES

7.1 INTRODUCTION

Previous experience has shown that the clouds produced by high yield, high explosive cratering events are reasonably accurate models of the clouds produced by nuclear cratering events (References 1, 2, and 3). For this reason, a comprehensive program was included on Project Pre-Schooner II (1) to document the development of the base surge cloud and the main cloud resulting from the detonation, and (2) to track the cloud for a short time as it dispersed downwind.

7.2 EXPERIMENTAL PROCEDURES

Three methods (cloud photography, a laser-radar system, and a fluorescent particle tracer technique) were used on Pre-Schooner II to accomplish the objectives of the Cloud Development Studies Program. Detailed information concerning these cloud documentation techniques are presented in the following paragraphs.

7.2.1 Cloud Photography. The objective of the cloud photography program was to document, as completely as possible, the early growth of the cloud up to stabilization time. The elements required for this program included: (1) cloud camera stations, (2) a target array, and (3) meteorological data collection.

a. Camera Complement. The cloud photography system for Pre-Schooner II consisted of three camera stations. Figure 7.1 shows the positions of the two ground stations relative to GZ and the anticipated cloud path. As is indicated in the figure, one station was located at the Pre-Schooner II Control Point (CP) and the other at the laser station. The third cloud camera station consisted of a helicopter flying above and slightly to the south of GZ. Table 7.1 presents a summary of pertinent data concerning the characteristics of the cloud cameras located at each station.

The cameras in Camera Station No. 2 (located at the CP) were started by a signal from the firing control console at a preset time. The cameras in Camera Station No. 3 (located at the laser station) were started manually and the starting time recorded. This starting time data together with the camera framing speed permitted the determination of a time for each frame referenced to zero time for the detonation. Zero time on the helicopter film was determined by a fiducial signal at GZ.

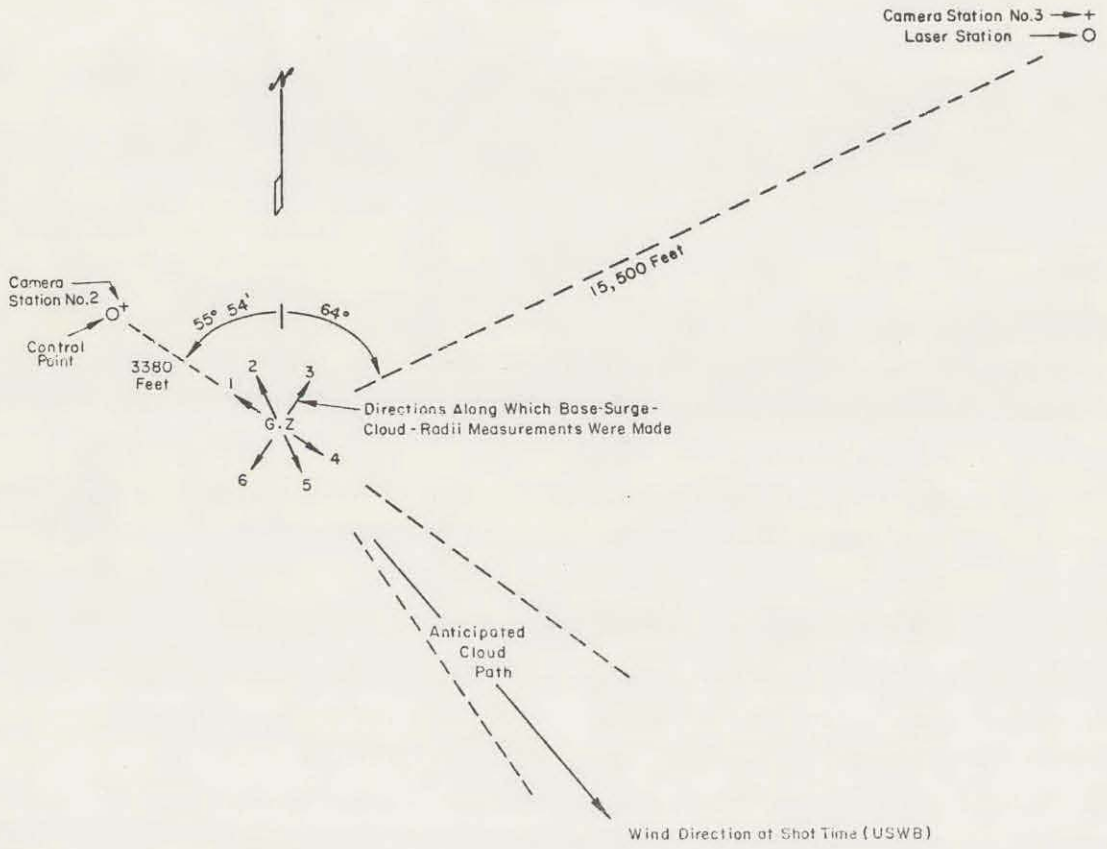

Figure 7.1 Cloud Camera Station Locations.

TABLE 7.1 CLOUD CAMERA CHARACTERISTICS

Station	Camera	Speed	Field of View	
			Vertical	Horizontal
			ft	ft
Camera Station No. 2 (located at CP)	CL 70	10 frames/min	1840	2455
	H 70	20 frames/sec	2257	2525
	Maurer	10 frames/min	5073	5073
Camera Station No. 3 (located at Laser Station)	DL 70	10 frames/min	8432	11253
	M	12-1/2 frames/sec	11346	15314
Helicopter Camera Station	Mil	48 frames/sec	--	--

b. Target Array. To provide points of reference for the photography, an array of bright red targets were placed on the surface at intervals of 500 feet in two

orthogonal rows through GZ extending out to 2000 feet from GZ. The CP was in line with one of the rows. Each target consisted of a horizontal section which was placed on the ground and a vertical section. This type of target design facilitated use of the targets as reference points for both the ground camera stations and the aerial (helicopter) camera station.

c. Meteorological Data. Radiosonde data were obtained at the time of the Pre-Schooner II detonation by the U. S. Weather Bureau (USWB) (Reference 4). The radiosonde balloon was released from the CP area at H + 1 min. Detailed temperature lapse rate data up to ~1500 feet were taken. The data were used to correct the maximum crosswind base surge radius to that which would have been produced in a neutral atmosphere. Other meteorological data recorded by USWB included wind speed and direction, pressure, and temperature up to 108,000 feet MSL.

7.2.2 Laser-Radar System. The laser-radar system was operated at the Pre-Schooner II site prior to and during the actual detonation (1) to determine the ability of the laser-radar system to record the presence of the cloud after standard photographic methods are no longer effective, and (2) to obtain estimates of distances to the cloud and the dimensions of the cloud at times later than H + 10 minutes. It was envisioned that the experience gained during Pre-Schooner II in the operation of the laser-radar system could be used to develop a laser-radar technique to measure the relative concentration of debris along a path through the cloud corresponding to the laser beam path. The location of the laser station is shown in Figure 7.1.

The laser-radar system used during Pre-Schooner II is illustrated in Figure 7.2 (Reference 5). It consists of a fixed stand upon which rests a rotating table, which in turn supports a receiving telescope which may be mechanically elevated or depressed. Mounted on this receiving scope is a housing, which supports a laser package consisting of a gas laser used for alignment purposes, a Xenon flash tube, and a ruby laser. In front of this laser box is a collinating telescope. In the center of the housing is a slot for a still camera and to one side of this is mounted a viewing or sighting telescope.

The sequence of operations of the laser system is as follows:

(1) The ruby laser is pulsed with the Xenon flash tube (power to the Xenon tube comes from a capacitor bank), and a beam of light is sent out through the collinating telescope to the cloud.

(2) The return signal which results from scatter of this beam of light by the cloud and the general atmosphere is filtered and then picked up by a photomultiplier tube.

(3) The electronic signal from the photomultiplier tube is transmitted to an oscilloscope on which it is displayed on a time scale referenced to the ruby laser pulse time.

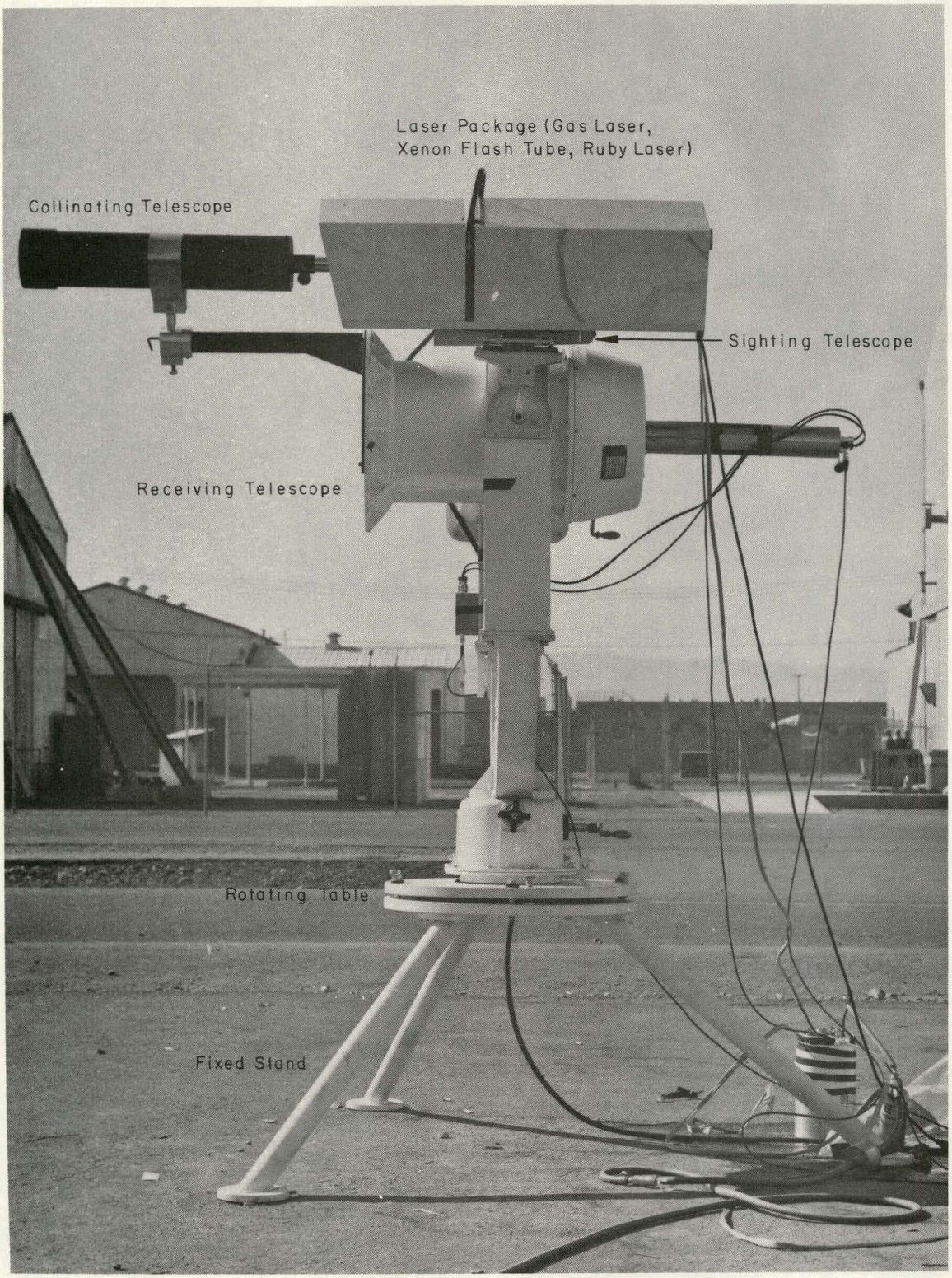

Figure 7.2 Laser Apparatus

(4) The distance to the cloud and the thickness of the cloud is then determined from the time it takes for the light to go to and from the front and back edges of the cloud. It is assumed that the signals from these interfaces are easily recognizable on the oscilloscope trace.

7.2.3 Fluorescent Particle Tracer Study. The fluorescent particle tracer study was conducted on Pre-Schooner II to determine whether such tracers could be mixed into the cloud in sufficient quantities to permit determination of cloud trajectory at various times after the detonation.

Small quantities (20 kg) of two colors of a fluorescent tracer, zinc cadmium sulfide (ZnCdS), were placed in two shallow holes near SGZ and covered loosely with dirt. Sampling stations downwind consisted of: (1) unmanned battery-operated ground filter units and rotating surface impaction collectors, and (2) an ARMS aircraft (operated by Edgerton, Germeshausen, and Grier, Inc. (EG&G) equipped with a filter unit mount. The ARMS aircraft was scheduled to sample the cloud during the time of laser beaming and as far downwind as daylight and terrain conditions would allow.

7.3 RESULTS

7.3.1 Cloud Photography Results

a. General. Figure 7.3 is a print from the helicopter film showing the Pre-Schooner II cloud at about three-fourths of its maximum growth. The right side of this print is in the general downwind direction. The specific cloud dimensions are discussed in the following paragraphs.

b. Base Surge Cloud Radius. Measurements of the base surge growth were taken in six directions from GZ as shown in Figure 7.1. The downwind direction at shot time (H + 1 minute) is also indicated in this figure. Curves showing base surge radius development as a function of time have been plotted in Figures 7.4 through 7.9. Each curve is labelled with the directions corresponding to those shown in Figure 7.1. Figure 7.6 (direction 3) is considered to be most representative of the cross wind, base surge radius growth. The maximum base surge radius as determined from this curve is 2100 feet.

c. Base Surge Cloud Height. Measurements of the base surge height were made from the Maurer Camera film (Camera Station No. 3). Figure 7.10 shows both upwind and downwind time history. There was a higher lobe that extended to an elevation of 700 feet on the downwind side which accounted for the difference in cloud height measurements. The representative base surge cloud height is considered to be 420 feet.

d. Main Cloud Height. Data from two film prints (Maurer and CL70) were used to determine the time history of the main cloud height. The data are plotted in Figure 7.11. Maximum main cloud height at stabilization is approximately 1400 feet.

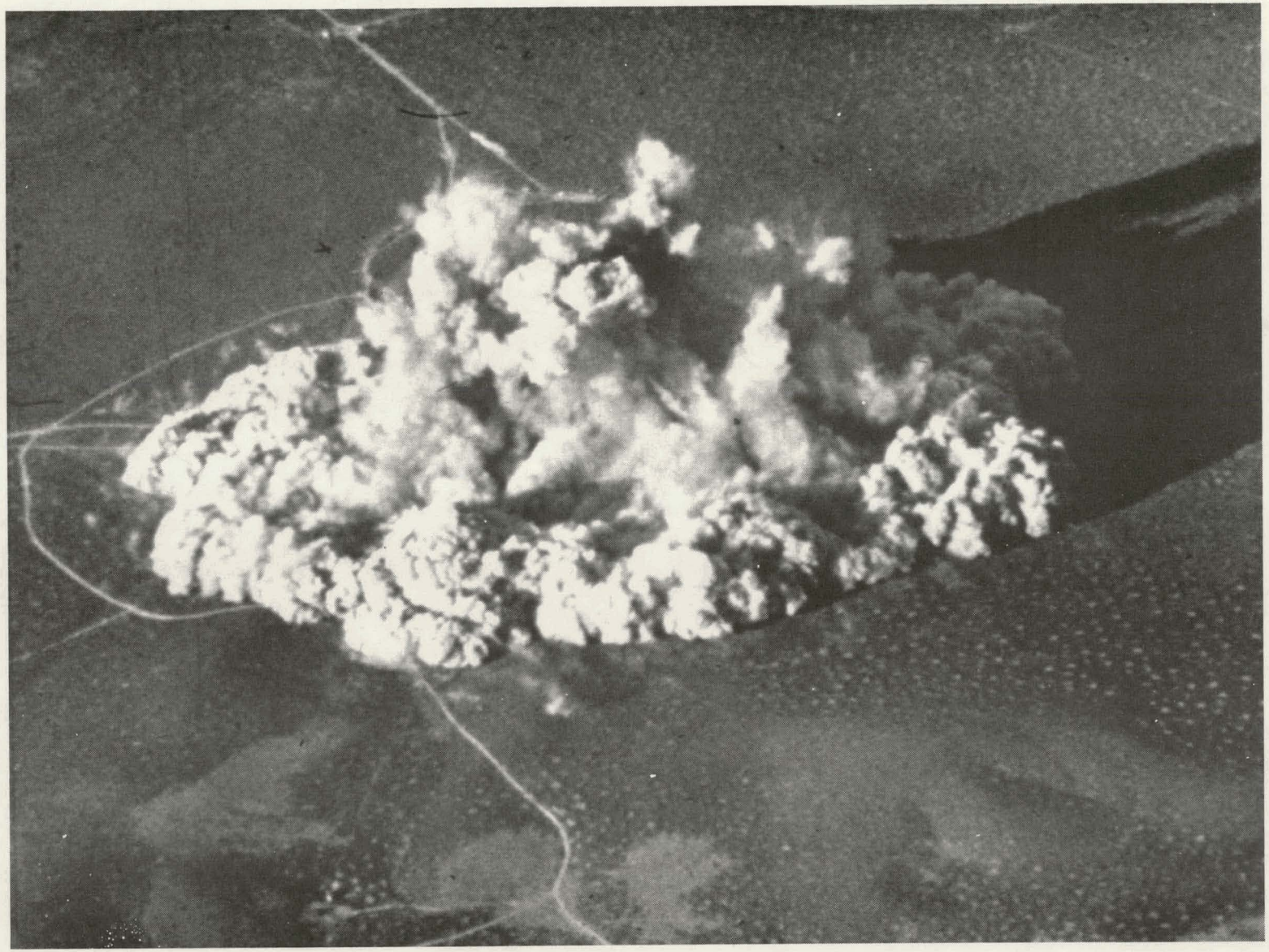

Figure 7.3 Cloud Development As Viewed From Helicopter.

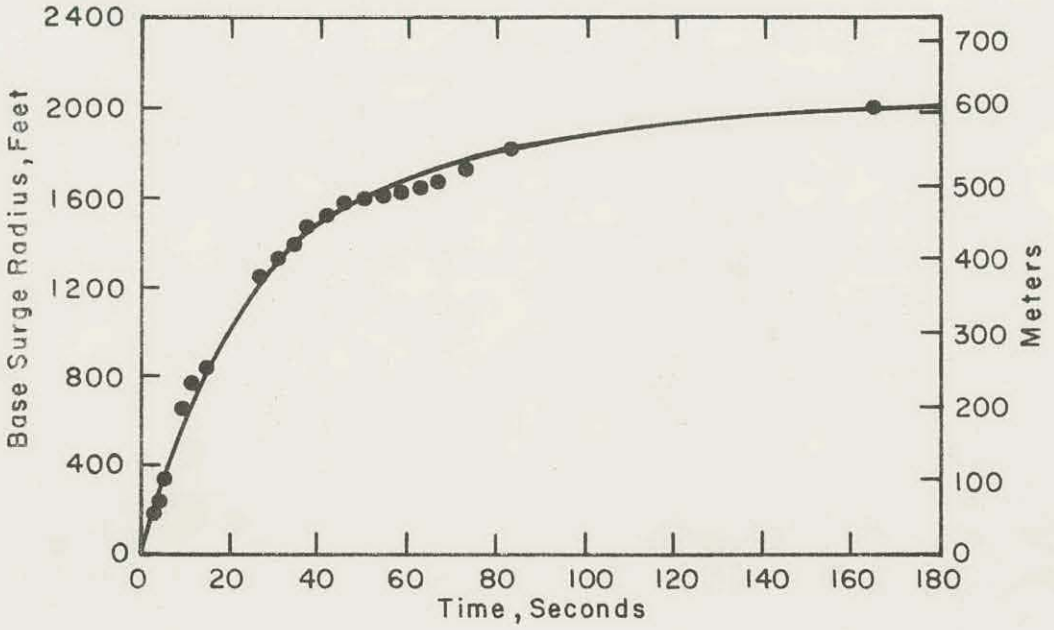

Figure 7.4 Base Surge Radius versus Time (Direction 1 - Helicopter Film).

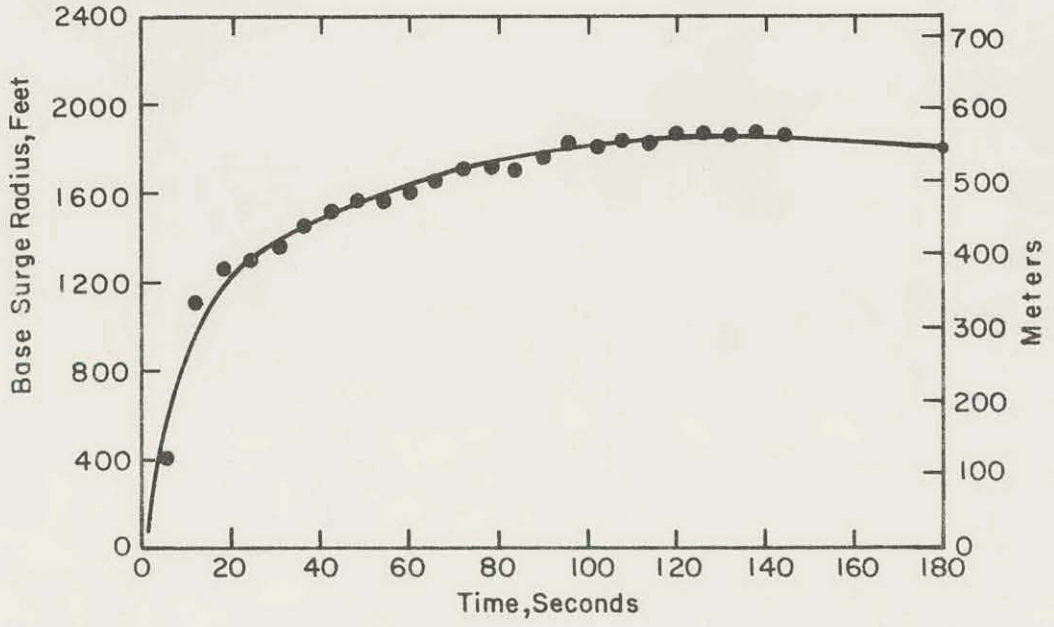

Figure 7.5 Base Surge Radius versus Time (Direction 2 - Camera Station No. 3 - DL 70 Camera).

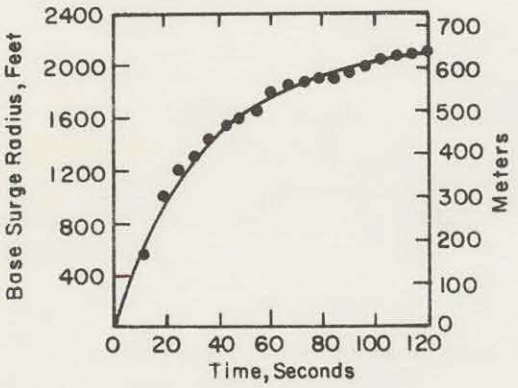

Figure 7.6 Base Surge Radius versus Time (Direction 3 - Camera Station No. 2 - Maurer Camera).

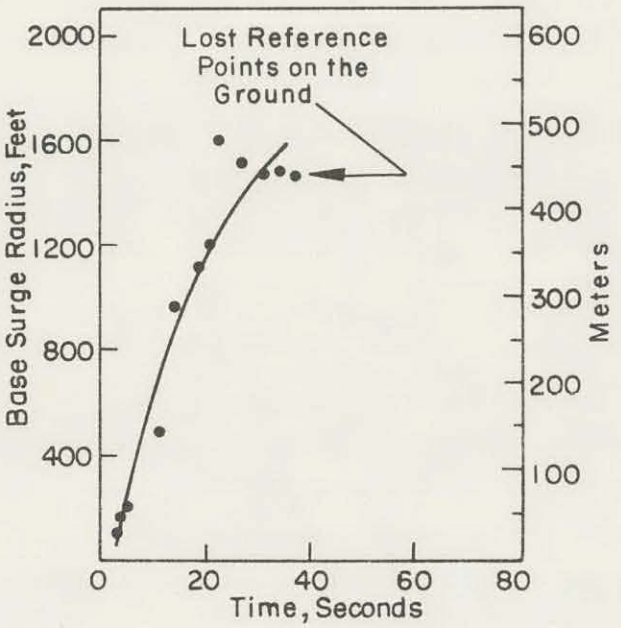

Figure 7.7 Base Surge Radius versus Time (Direction 4 - Helicopter Film).

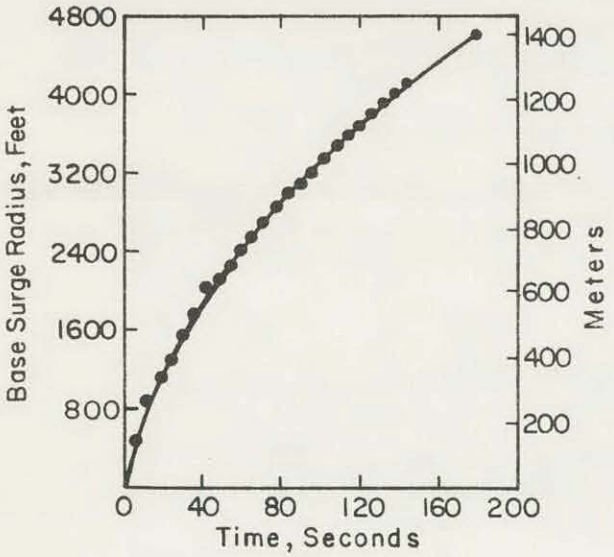

Figure 7.8 Base Surge Radius versus Time (Direction 5 - Camera Station No. 3 - D L 70 Camera).

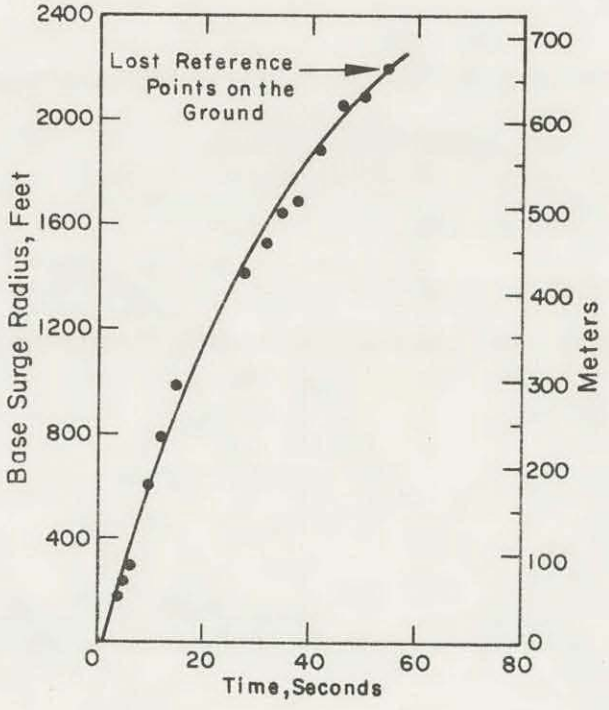

Figure 7.9 Base Surge Radius versus Time (Direction 6 - Helicopter Film).

e. Main Cloud Radius. The time history of the main cloud diameter was measured using the Maurer camera at Camera Station No. 2. The data are plotted in Figure 7.12. The maximum main cloud radius as determined from the curve is 1750/2 feet = 875 feet.

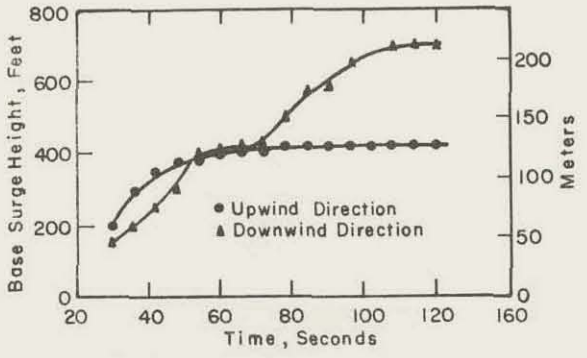

Figure 7.10 Base Surge Height versus Time (Camera Station No. 2 - Maurer Camera).

f. Lapse Rate Conditions. Figure 7.13 is a plot of altitude versus temperature at shot time (H + 1 minute) up to 1735 feet. Above this altitude, the lapse rate varied from slightly stable to isothermal. It is believed that the extremely unstable condition from the surface to ~175 feet influenced the base surge radial growth. The temperature change over this elevation is 4.3×10^{-2} deg. C/meter.

Table 7.2 presents a summary of the Pre-Schooner II cloud dimensions at stabilization. The predicted base surge cloud dimensions and the temperature-corrected base surge cloud radius as shown in Table 7.2 are discussed in Section 7.4.

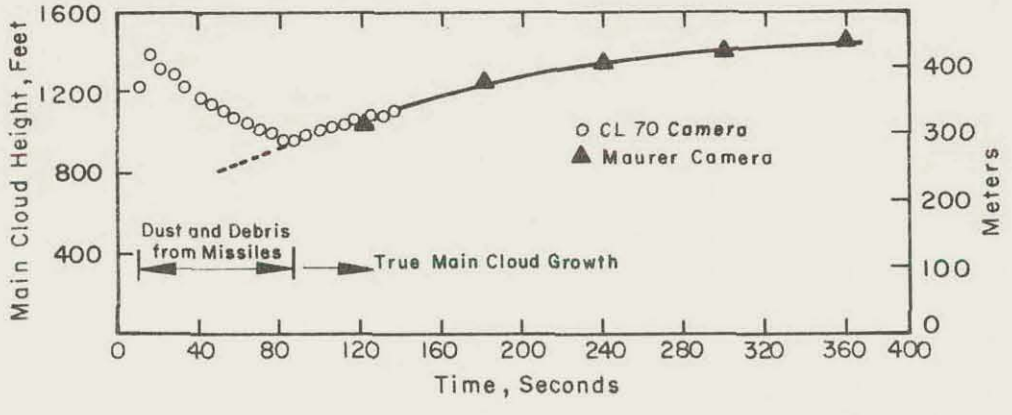

Figure 7.11 Main Cloud Height versus Time (Camera Station No. 2).

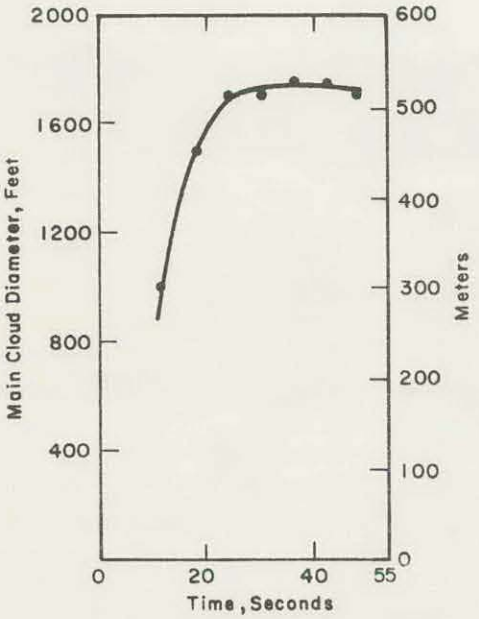

Figure 7.12 Main Cloud Diameter versus Time (Camera Station No. 2. Maurer Camera).

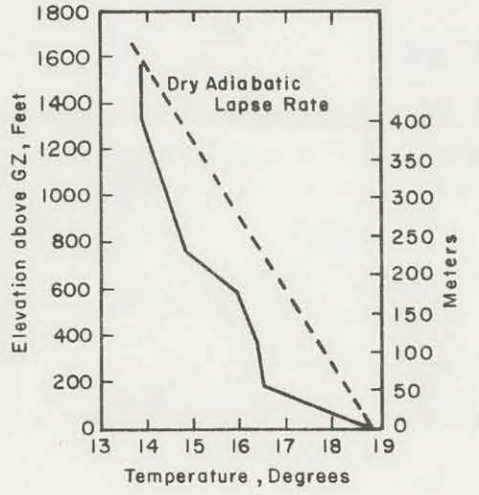

Figure 7.13 Altitude versus Temperature at H + 1 Minute.

7.3.2 Laser-Radar Results. The laser-radar operation during the time of the Pre-Schooner II detonation did not result in the determination of meaningful cloud dimension data. During dry run periods prior to shot day, however, the laser-radar system showed positive response from cumulus clouds. In fact, the distance to and thickness of the cumulus clouds as determined by the laser system during the dry runs agreed quite well with local cloud data provided by the USWB.

Analysis of the operational and atmospheric conditions existing at detonation time indicates that the position of the sun was a very influential factor in the poor response of the laser-radar system. At the time of detonation (1709 MST), the sun was in a position practically on a line between GZ and the laser station. It is believed that the high background signal from the sun which was received at the photomultiplier tube completely masked the returning ruby laser signal. None of the dry run laser operations, during which positive response was achieved, had been performed with the sun in a position similar to that on shot day.

Although the laser-radar operations did not accomplish the stated program objectives during the actual detonation, it is believed that valuable field experience was gained which will assist considerably in improving the design of laser-radar equipment for cloud tracking purposes.

7.3.3 Fluorescent Particle Tracer Results. All of the ground filter units placed downwind operated properly. The ARMS plane sampled the cloud for approximately 1 hour after the detonation.

TABLE 7.2 PRE-SCHOONER II CLOUD DIMENSIONS

Dimensions in feet.

	Predicted	Observed	Temp. Corrected
Base Surge Radius	970[a]	2100	965[a]
Base Surge Height	1060	420-700	--
Main Cloud Radius	--	875	--
Main Cloud Height	--	1400	--

[a]Neutral atmosphere.

To date, only a few of the ground filter unit samples have been analyzed. The fluorescent tracer, ZnCdS, has been present in these samples (Reference 6). The final results of this cloud tracer experiment will be reported in the final report (Reference 7).

7.4 DISCUSSION AND INTERPRETATION

7.4.1 Analysis of Base Surge Cloud Dimensions. Previous studies have indicated that the base surge growth is influenced by the temperature lapse rate (References 1, 2, and 3). A method for correcting the observed base surge radius to that which would have been produced in a neutral atmosphere was developed for the Pre-Buggy experiment (Reference 3) and was used to correct the observed cloud data for that experiment as well as for the Dugout and Pre-Schooner I experiments (References 1 and 2). A plot of the base surge data from the above-mentioned experiments and the data from nuclear cratering events (normalized to 1 kt using 0.3 power scaling) versus scaled depth of burst (in meters/$kt^{1/3}$) has indicated a systematic difference in the neutral-atmosphere base surge radius in basalt as compared to that in alluvium. In making base surge predictions for Pre-Schooner II, it was believed that it would be more nearly correct to scale from the basalt data rather than from the alluvium data since the detonation medium was a hard, dry rock classified as rhyolite. Base surge predictions, therefore, were made by scaling from Danny Boy cloud data, since the scaled depth of burst of Pre-Schooner II was approximately the same as that for Danny Boy (0.3 power scaling was used for base surge radius and 0.2 power scaling was used for base surge height). Since the Danny Boy event had no main cloud, no main cloud dimensions were predicted for Pre-Schooner II although all of the Pre-Schooner I 20-ton H. E.

events had what appeared to be a small main cloud, and such a cloud was expected for Pre-Schooner II. The predicted base surge height was not based on any specific atmospheric conditions.

Figure 7.14 gives the correction factor used to correlate the observed base surge radius in an unstable atmosphere to that of a neutral atmosphere. The data for for this plot are based on information contained in Reference 3. Using this curve and a lapse rate of 4.3×10^{-2} deg. C/meter (as determined for Pre-Schooner II shot day atmospheric conditions), a correction factor of 0.46 is obtained. As indicated in Table 7.2, application of this correction factor to the observed base surge radius results in a neutral-atmosphere base surge radius of 965 feet. The very close agreement between observed and predicted dimensions is somewhat fortuitous since the predicted dimension was based on a total charge weight of 100 tons of NM and the actual base surge radius was produced by a charge weight of 85.5 tons of NM. The Pre-Schooner II neutral-atmosphere base surge radius is plotted on Figure 7.15 together with data from the other cratering events.

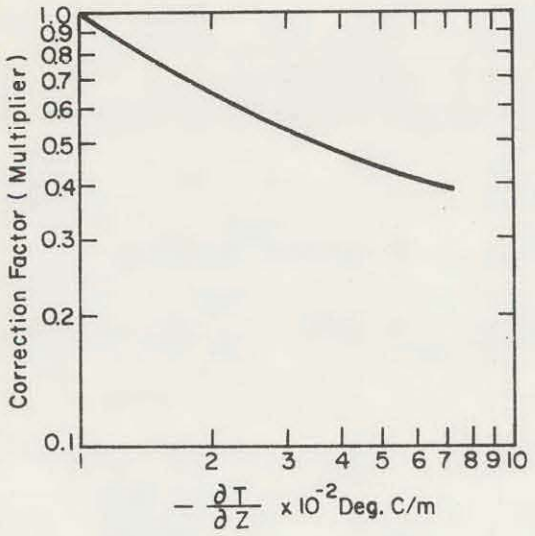

Figure 7.14 Correction Factor versus Lapse Rate.

The effect of an unstable atmosphere on base surge radius predictions is obvious from the foregoing discussion. The actual base surge radius could be as much as a factor of two larger in an unstable atmosphere than the radius that would be predicted from data based on an assumed neutral atmosphere condition.

7.4.2 Comments on Laser-Radar Operation. Since the laser-radar system used on Pre-Schooner II was an experimental item which had not been previously tested under field conditions, the fact that no meaningful cloud data were obtained by this technique is neither surprising nor particularly discouraging. The basic idea of using a system such as laser-radar to track the cloud at late times is well-founded. It is believed that the highly satisfactory response of the system to cumulus clouds during dry run periods prior to shot day is sufficient encouragement to proceed with development of a field operational laser-radar system for use in studying cloud behavior on future cratering events.

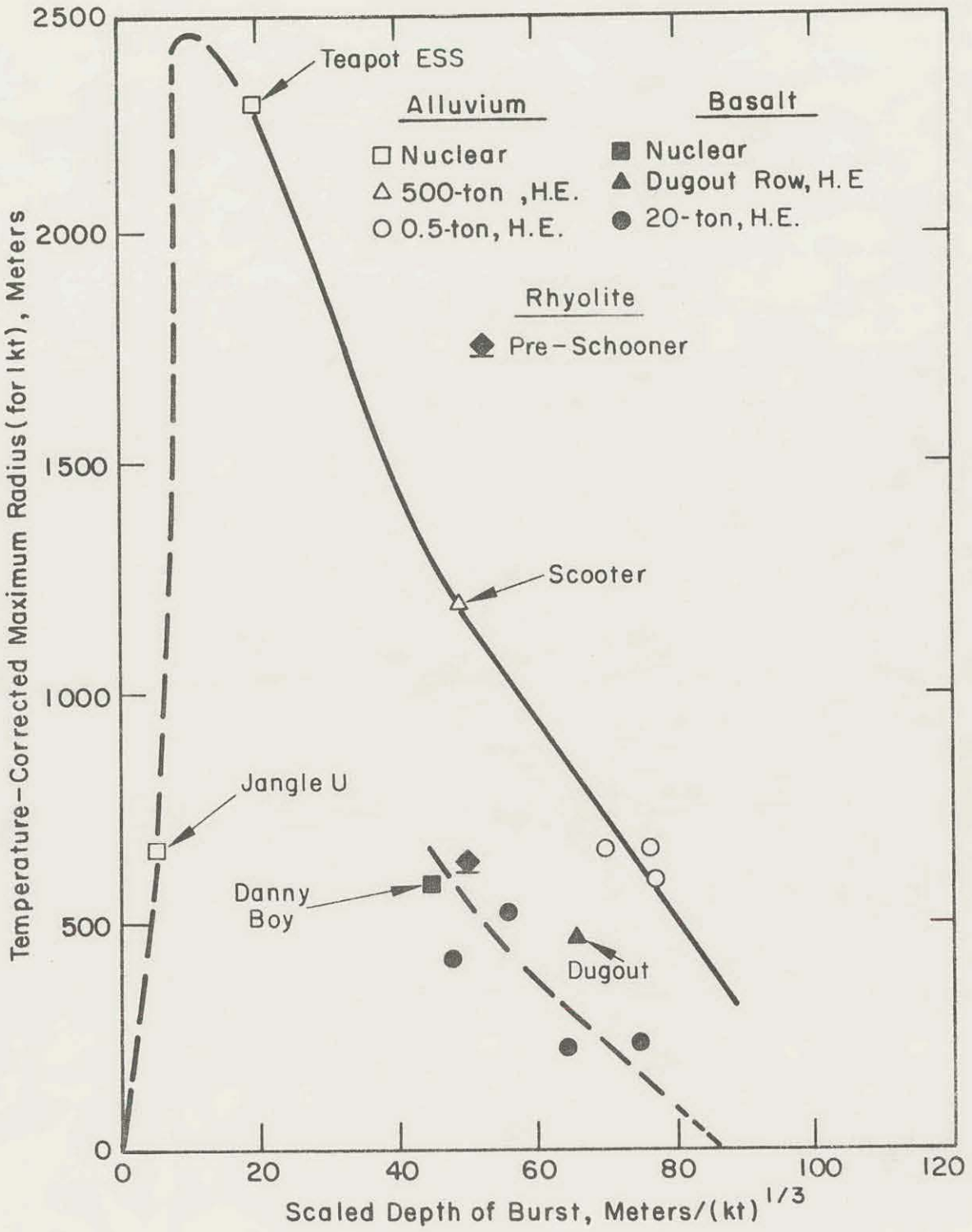

Figure 7.15 Scaled Maximum Base Surge Radii versus Scaled Depth of Burst (Alluvium, Basalt, and Rhyolite).

REFERENCES

1. M. D. Nordyke; "Technical Director's Summary Report, Project Dugout"; PNE 600F, December 1964; Lawrence Radiation Laboratory, Livermore, California.

2. R. F. Rohrer; "Base Surge and Cloud Formation, Project Pre-Schooner"; PNE 503F, April 1965; Lawrence Radiation Laboratory, Livermore, California.

3. J. B. Knox and R. F. Rohrer; "Base Surge Analysis"; PNE 304, September 1963; Lawrence Radiation Laboratory, Livermore, California.

4. J. R. Morrell, ESSA Research Station, Las Vegas, Nevada, 20 October 1965, private communication.

5. J. S. Kahn; "Laser Add-on to Pre-Schooner II"; LRL Internal Memorandum, 8 October 1965; Lawrence Radiation Laboratory, Livermore, California.

6. A. Prindle, Lawrence Radiation Laboratory, 19 November 1965, private communication.

7. W. C. Day and R. F. Rohrer; "Pre Schooner II Cloud Development Studies"; PNE 511F, to be published; U. S. Army Engineers Nuclear Cratering Group and Lawrence Radiation Laboratory, Livermore, California.

CHAPTER 8

AIR BLAST MEASUREMENTS

8.1 INTRODUCTION

The air blast resulting from nuclear cratering detonations is of major significance in assessing the operational safety aspects of nuclear excavation. Damage to structures in the region close to the detonation may be caused by the direct wave which is generally only moderately affected by meteorological conditions. Structural damage at longer ranges may result from atmospheric focusing of the air blast wave.

The following were the objectives of the Pre-Schooner II Air Blast Measurements Program, which was sponsored by Sandia Corporation:

a. To determine the extent of close-in blast suppression for the Pre-Schooner II detonation and to compare this suppression with that from other subsurface detonations. (The blast suppression factor may be defined as the ratio of overpressure that would be expected from a surface detonation to the observed overpressure from a subsurface detonation of the same yield at the same scaled range).

b. To determine long-range transmission factors[1] for the Pre-Schooner II detonation and to compare the results with data from previous detonations.

c. To determine the nature of close-in air blast transmission as a function of zenith angle and radial distance from SGZ.

d. To provide air blast data which may be used to predict outputs from the Schooner event and other planned nuclear excavation events.

8.2 EXPERIMENTAL PROCEDURES

8.2.1 Close-in Air Blast Measurements. Close-in air blast from the Pre-Schooner II detonation was measured by a line of ground level air blast gages and by an airborne blast gage array.

---

[1] "Transmission factor" is defined as the ratio of peak overpressure for a buried charge to that expected at the same range from the same yield detonated in free air.

a. Ground Level Gages. The ground level air blast gages were included in the air blast measurements program to determine the extent of blast suppression. The line of gages extended from GZ on a bearing of S44° 59' 46"E. The ground gage station locations are shown in Figure 8.1. Data pertaining to the characteristics of the gages are given in Table 8.1.

b. Airborne Gage Array. An airborne blast gage array was used to determine the nature of close-in air blast transmission as a function of zenith angle and radial distance from SGZ.

The airborne blast gage array consisted of two lines of gages supported from a balloon. The concrete anchor points for the gage-supporting cables were located at distances of 150 and 1000 feet from GZ along the line of the ground level gages. The airborne gage locations are shown in Figure 8.1. Pertinent data concerning the characteristics of the airborne gages are given in Table 8.2.

The signals generated by the air blast overpressure at the gages were transmitted to a recording trailer at the CP by two methods. A radio-telemetry system was used to transmit the signals from the following airborne gages: GA-3, GA-5, GA-7, GA-11, GA-13, and GA-15. The airblast signals from the other airborne gages and from all the ground level gages were transmitted to the recording trailer by hard wire.

c. Balloon Operation. The balloon operation conducted as a part of the air blast measurements program was designed to accomplish a twofold objective: (1) to support the two lines of air blast gages anchored 150 and 1000 feet from GZ, and (2) to demonstrate the feasibility of rapidly pulling a balloon down immediately after the detonation.

The helium-filled balloon which supported the two lines of airborne gages was 44 feet in diameter and 147 feet long. The balloon was flown at an altitude of approximately 4000 feet directly over the anchor point which supported the line of airborne gages 1000 feet southeast of GZ. The cable array attached to the balloon included one pulldown cable with a 10-ton breaking strength, two guy cables with breaking strengths of 5 tons one of which also served as a gage-supporting cable, and a lower strength gage-supporting cable.

It was planned to start pulling the balloon down from an altitude of 4000 feet to within 200 feet of the ground surface at 10 seconds after the Pre-Schooner II detonation (H + 10 seconds). A tractor attached to a multiloop cable and sheave system was scheduled for use to pull the balloon down at a descent rate of 18 to 20 mph. The purpose of the pulldown operation was to demonstrate the capability of pulling the balloon down below interference level in sufficient time to allow low-flying aircraft to pass over the GZ area. It was anticipated that a successful demonstration of this pulldown capacity would serve as evidence of the feasibility of using a balloon to support

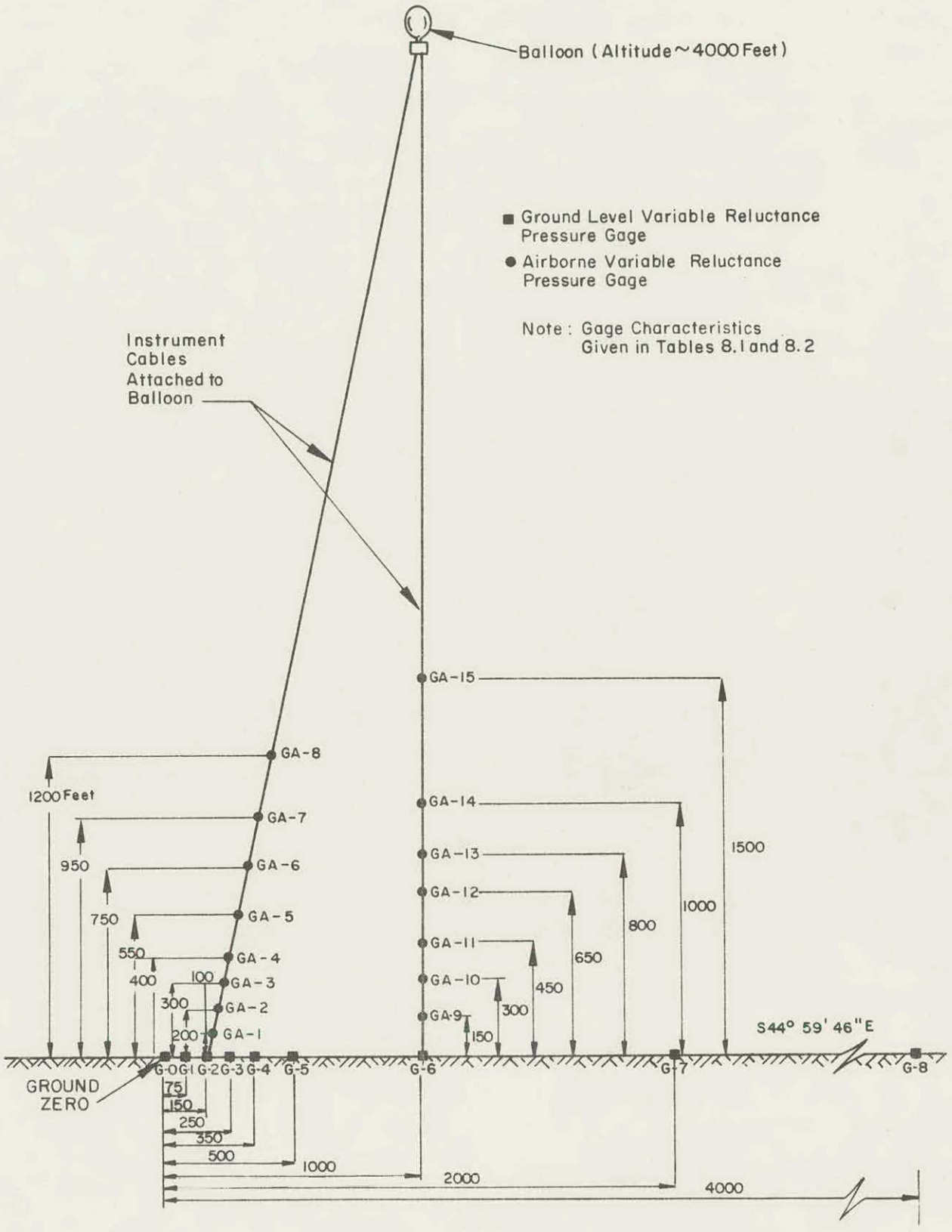

Figure 8.1 Schematic Layout of Ground Level and Airborne Pressure Gages.

TABLE 8.1 CHARACTERISTICS OF GROUND LEVEL GAGES[a]

Gage No.	Gage Location (Distance from GZ)	Full Gage Range	Set Gage[b] Range
	ft	psi	psi
G-0	0	--	--
G-1	75	10	7.5
G-2	150	5	1
G-3	250	1	0.5
G-4	350	0.25	0.10
G-5	500	0.10	0.08
G-6	1000	0.05	0.04
G-7	2000	0.05	0.02
G-8	4000	0.05	0.01

[a]See Reference 1

[b]Set Gage Range corresponds to the predicted level of overpressure expected at the gage location.

airborne blast gages in the vicinity of GZ during a nuclear cratering experiment. A rapid pulldown capability would be mandatory in order to use balloon-supported air blast gages in the vicinity of GZ during a nuclear cratering experiment since radiological monitoring planes must pass over the GZ area at relatively low altitudes shortly after shot time.

8.2.2 Long-Range Air Blast Measurements (Reference 2). Air blast waves at long ranges scaled from previous cratering detonations buried near optimum depth of burst have shown that:

a. Attenuation decreases with increasing yield

b. Attenuation is greater in alluvium than in hard rock

c. Attenuation is greater for N. E. than for H. E.

To verify these relations and to provide data for extrapolation to large-scale nuclear cratering experiments, six microbarograph stations were operated during Pre-Schooner II. The stations were established to record long-range air blast signals from the Pre-Schooner II detonation and from three H. E. calibration shots. The microbarograph observations from the H. E. calibration shots were to be appropriately

TABLE 8.2 CHARACTERISTICS OF AIRBORNE GAGE ARRAY[a]

Gage No.	Elevation of Gage Above Ground	Full Gage Range	Set Gage[b] Range
	ft	psi	psi
Gages Supported from Line Anchored 150 feet from GZ:			
GA-1	100	0.50	0.40
GA-2	200	0.25	0.20
GA-3	300	0.25	0.17
GA-4	400	0.25	0.15
GA-5	550	0.10	0.10
GA-6	750	0.10	0.08
GA-7	950	0.10	0.06
GA-8	1200	0.10	0.05
Gages Supported From Line Anchored 1000 feet from GZ:			
GA-9	150	0.10	0.04
GA-10	300	0.10	0.05
GA-11	450	0.10	0.05
GA-12	650	0.10	0.05
GA-13	800	0.10	0.04
GA-14	1000	0.05	0.04
GA-15	1500	0.10	0.04

[a]See Reference 1.

[b]Set Gage Range corresponds to the predicted level of overpressure expected at the gage locations.

scaled and compared with the signals from the Pre-Schooner II detonation to calculate the air blast transmission factors.

Due to the uncertainty in the projected upper wind conditions at shot time, it was decided to operate the six microbarograph stations at various directions from the detonation in order to insure maximum possible probability of obtaining meaningful long-range signals. The station locations selected were:

Location	Azimuth Referenced from GZ	Distance from GZ
	degrees	feet
Arco, Idaho	050	662,144
American Falls, Idaho	079	704,187
Lucin, Utah	128	583,551
Martin Creek, Nevada	243	583,679
Rome, Oregon	275	623,445
Ontario, Oregon	325	686,796

These station locations are shown in Figure 8.2.

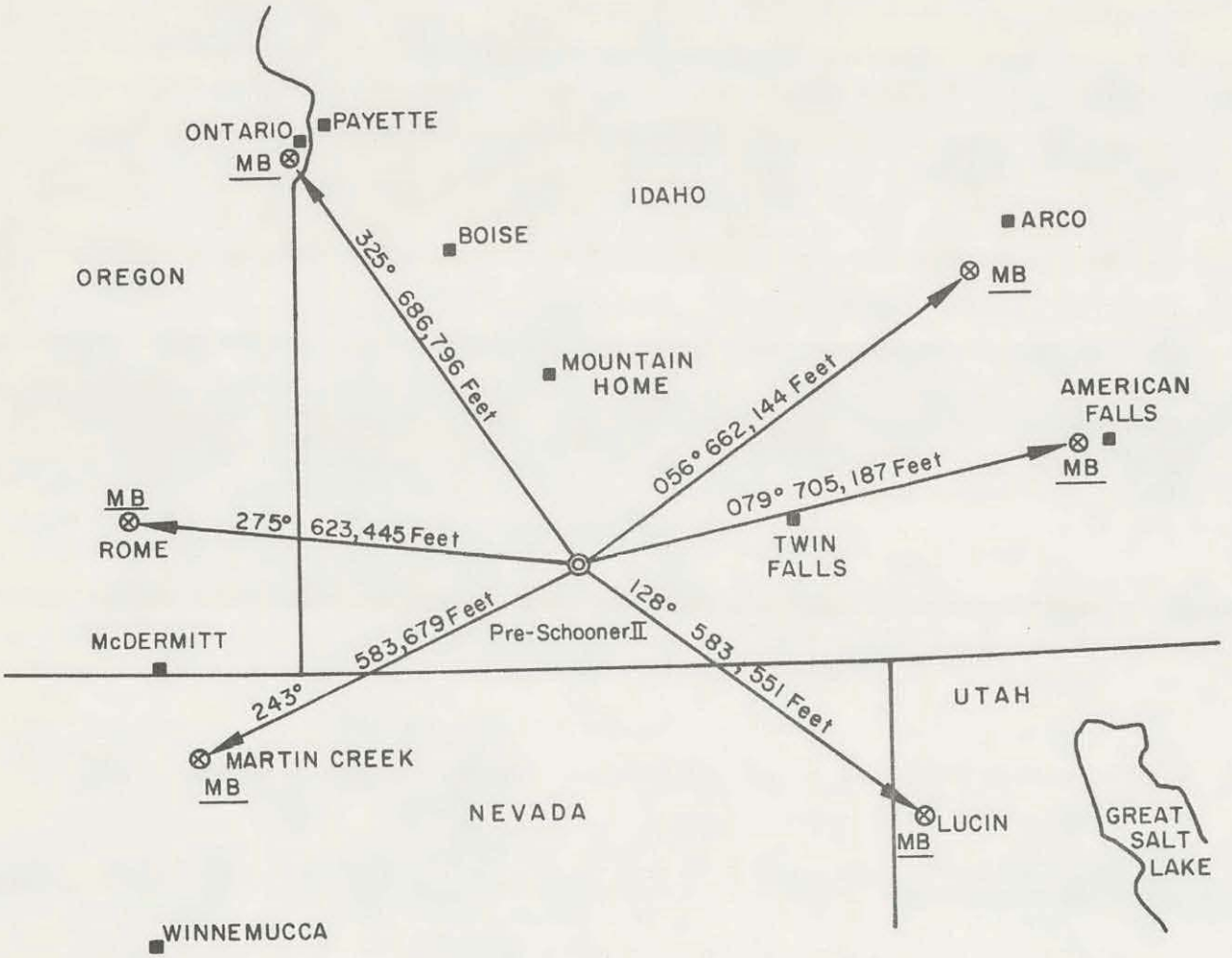

Figure 8.2 Microbarograph Station Locations.

Three 1.2-ton H. E. calibration shots identified as HE No. 1, HE No. 2, and HE No. 3, were scheduled to be fired on 15-foot high, wooden platforms at H - 2 minutes, H + 3 minutes, and H + 5 minutes, respectively.

Rocket upper-air observations were scheduled to be made at Tonopah to show approximately the winds which caused the observed blast propagations.

8.3 PRELIMINARY RESULTS

8.3.1 Close-in Air Blast (Reference 3). To date, the close-in gage measurements have not been completely analyzed. It is pertinent, however, based on a preliminary examination of the records and observations at the Pre-Schooner II site, to make some general comments concerning the results of the close-in air blast measurements program. A detailed presentation of the experimental procedure and the results will be given in the final report (Reference 4).

a. Airborne Blast Gage Measurements. As is characteristic of high explosive cratering detonations, the close-in air blast signal from the Pre-Schooner II detonation was composed of two distinct signals. The first signal resulted from a ground-shock-induced wave which reaches the epicenter after traveling at the sonic velocity of the shot medium. From the vicinity of the epicenter this wave tends to travel at sonic velocity in air. This pulse was followed by a second pulse which is related to the venting gas generated by the explosion. A preliminary examination of the Pre-Schooner II records for the airborne gages indicates that the gas-venting peak over-ranged 11 of the 14 gages (Gage GA-7 was not used for the air blast measurement program). The first peak associated with the ground-shock-induced wave appears to have been within the range of all but 4 gages; and, therefore, it is believed that meaningful first peak overpressure data can be obtained from the airborne gage records. Ground-shock-induced pressures from the Pre-Schooner II detonation were twice those from previous cratering detonations at comparable scaled ranges.

b. Ground Level Blast Gage Measurements. The ground level gage records indicate that the gas-venting peak over-ranged the GZ gage (G-0) but that the ground-shock-induced peak was within the range of the gage as was expected. At the next ground gage station (G-1), the record shows that the gas-venting peak was less than the ground-shock-induced peak. At the third station (G-2), the gas-venting peak was approximately equal to the ground-shock-induced peak. At the other stations (G-3 through G-8), the peak from the venting gases was larger than the ground-shock-induced peak and over-ranged the gages. An analysis of measurements from these gages will provide useful information concerning close-in air blast ground-shock-induced propagation from the Pre-Schooner II detonation.

The balloon which supported the airborne gages was lowered from an elevation of 4000 feet to an elevation of 200 feet immediately following the detonation. The lowering operation was completed in approximately 7 minutes. It is reasonable to conclude, therefore, that balloon-supported air blast instruments which an appropriate pulldown arrangement can be used during a nuclear cratering experiment without interfering with radiological monitoring aircraft.

8.3.2 Long-Range Air Blast (Reference 5). The first countdown for the Pre-Schooner II detonation was stopped at 9 seconds prior to zero time because it appeared that the baritol flares which were to be used as part of the ground surface motion studies program were not burning properly. Since calibration shot HE No. 1 had been fired at H - 2 minutes, the timing signal for calibration shot HE No. 3 (scheduled for firing at H + 5 minutes) was changed to detonate that shot at H - 2 minutes for a new zero time (this was a prearranged signal capability which had been incorporated in the firing system). The Technical Director started the second countdown within 30 minutes after the first countdown had been stopped, and the Pre-Schooner II detonation was fired. The two remaining H. E. calibration shots (HE No. 2 and HE No. 3) were detonated as scheduled at H - 2 minutes and H + 3 minutes.

In fall, as in spring, there is a seasonal reversal of upper atmosphere wind direction between summertime easterlies and wintertime westerlies. During these transitions upper winds may be light and variable, and long-range blast propagation is very weak in all directions. This was the case the day Pre-Schooner II was detonated (30 September 1965). When unseasonable snows struck the region in early September it was hoped that an early winter was at hand and that there would be good eastward blast propagation on shot day. In fact just the week before Pre-Schooner II, wind rocket reports from White Sands Missile Range showed some light winter westerlies. It was expected that stronger westerlies would prevail over more northern latitudes. As it turned out, however, the Tonopah wind rocket fired near shot time showed generally light and variable winds at all altitudes below about 180,000 feet where moderate westerlies did commence. The only sound ducting calculated from ozonosphere conditions was caused by the wind reported at 145,000 feet of 175° -35 knots. This gave a small sound ring, about 10 miles wide, over the Ontario station (see Figure 8.2). Recordings at Ontario did not verify that such a propagation ring was present. Pressure amplitudes recorded there were only one-fortieth to one-sixtieth as large as were calculated.

A summary of all station records is shown in Table 8.3. Calibration shots gave only 2 to 5 μb wave amplitudes, via ozonosphere propagation, at Ontario, Rome, and Martin Creek. No ozonosphere signals could be detected at any of the stations to the east. Thus, it appears that weak easterlies aloft, remnants of summertime, gave

TABLE 3.3 MICROBAROGRAPH MEASUREMENTS[a]

Station[b]	Signal Path[c]	Signal	HE No. 2 Detonated at H - 2 Minutes			Pre-Schooner II			HE No. 3 Detonated at H + 3 Minutes		
			Travel Time, t_a	Average Velocity, $\bar{V}$	Pressure Amplitude, p_k	t_a	$\bar{V}$	p_k	t_a	$\bar{V}$	p_k
			sec	ft/sec	μb	sec	ft/sec	μb	sec	ft/sec	μb
Ontario	Z	a	751.7	915	1.6[d]	753.4	913	2.84[d]	152.1	915	2.64
		b	756.4	910	2.0[d]	764.3	900	2.64[d]	766.2	897	2.64
Rome (Open)	Z	a	700.2	888	5.77	702.1	888	5.39	700.2	885	5.97
(Fenced)	Z	a	699.8	888	4.60	702.3	887	4.00	700.6	885	4.60
Martin Creek	Z	a	644.3	900	4.44	649.5	900	2.11	644.0	900	2.74
Lucin	T	a	510.8	1142	4.69[e]	511.5	1140	2.62[e]	511.9	1140	5.81[e]

[a]HE No. 1: Only Ontario station recorded signals: (1) t_a = 758.7 sec; $\bar{V}$ = 907 ft/sec; p_k = 2.69 μb; and (2) t_a = 761.7 sec; $\bar{V}$ = 903 ft/sec; p_k = 3.52 μb. Rome, Martin Creek, and Lucin operators shut off recorders when Pre-Schooner II was held at -9 sec before expected signal arrival times.

[b]No signals detected at American Falls (wind noise 2 μb, gusts to 8 μb) and Arco (wind noise 20 μb, gusts to 50 μb).

[c]Signal paths are Z: Ozonosphere (above 100,000 ft. MSL), and T: troposphere (below about 10,000 ft. MSL, in this instance).

[d]Electrical pulses on recording obscure probable maximum oscillation from blast waves.

[e]Possible signals, fair correlation between records, wind noise ≤2 μb at 3 cps, but 20 μb at 1/2 cps.

the slight westward propagations which were relatively uniform in amplitude at the three stations.

Weak signals reported at Lucin arrived early and, if real, must have been propagated by northerly winds in the turbulent boundary layer, probably below 10,000 feet MSL. Wind noise on this Lucin record makes these signal reports subject to considerable doubt but they appear to correlate fairly well.

Use of snow-fence rings around MB sensors worked exceptionally well. Without them, signal interpretation at the western stations would have been much more difficult. At Rome two sensors were installed. One was set up without fencing, and the signal reported from it could barely be separated from ambient noise by correlation. On the fenced sensor, however, wind noise was filtered by a factor of at least 5 or 6 and the blast signal was clear and easily read. Lower peak-to-peak amplitudes for the fence-filtered signals may have been caused by attenuation by the fence. It may, on the other hand, represent removal of spurious noise levels added to the open sensor record. This factor must be investigated further in other experiments.

Transmission factor calculations were made for each pair of comparable signals, one Pre-Schooner II wave and one calibration shot wave. Comparative data from Ontario between HE No. 2 and Pre-Schooner II were not used in averaging because it is clear that peak amplitude HE No. 2 waves were truly lost in electrical noise since comparatively large transmissivity values resulted. It should also be noted that data from Rome fenced and open sensors are not independent. The average transmissivity for ten points was calculated as T = 0.187. The best data points are the two comparisons from fenced sensor records at Rome, where both HE No. 2 and HE No. 3 gave 4.6 μb amplitudes and T = 0.199. In summary, it is recommended that an average value of T = 0.19 be used for the Pre-Schooner II detonation. With so few good record comparisons an adequate assessment for variability could not be made, but it appears that signal variability between the short time intervals is not so large as has been found from NTS propagations.

A transmissivity of 0.19 for 155 feet/$(\text{kt})^{1/3}$ scaled burst depth agrees well with other high explosives cratering test data.

REFERENCES

1. B. C. Holt, Sandia Corporation, private communication.

2. A. B. Church; "Experimental and Requirements Plan for Plowshare Operation, Pre-Schooner II Event, Microbarograph Project"; SC report, August 4, 1965; Sandia Corporation.

3. L. J. Vortman, Sandia Corporation, private communication.

4. L. J. Vortman and J. Reed; "Air Blast Measurement"; PNE-512F, to be published; Sandia Corporation.

5. J. Reed, Sandia Corporation, private communication.

APPENDIX A

PRE-SCHOONER II TECHNICAL REPORTS

Title of Report	Agency	Author and/or Technical Program Officer	Report Number
Technical Director's Summary Report	NCG	B. C. Hughes et al	PNE 507
Apparent Crater Studies	NCG	R. H. Benfer	PNE 508
Preshot Geologic Investigations and Engineering Properties	WES/NCG	W. C. Sherman, Jr./ R. A. Paul et al	PNE 509
Design and Postshot Evaluation of Access Hole Stemming	WES	K. L. Saucier	PNE 510
Base Surge and Cloud Formation	NCG/LRL	W. C. Day/R. F. Rohrer	PNE 511
Air Blast Measurements	SC	L. J. Vortman/ J. W. Reed	PNE 512
Surface Motion Measurements	NCG	K. L. Larner	PNE 513
Ground Shock Measurements	Roland F. Beers, Inc.	L. L. Davis	PNE 514
Subsurface Effects Measurements	LRL	M. Heusinkveld/ R. E. Marks	PNE 515
Postshot Geologic Investigations and Engineering Properties	NCG	A. D. Frandsen	PNE 516

DISTRIBUTION

	No. of Copies
LRL Internal Distribution, Information Division	30
M. May	
R. Batzel	
J. Gofman	
R. Goeckermann	
C. Haussmann	
J. Rosengren	
D. Sewell	
C. Van Atta	
R. Herbst	
C. McDonald	
E. Goldberg	
G. Higgins	
J. Carothers	
S. Fernbach	
J. Hadley	
J. Kane	
B. Rubin	
J. Kury	
P. Stevenson	
J. Bell	
E. Hulse	
W. Decker	
W. Harford	
G. Werth	
M. Nordyke	2
F. Holzer	2
H. Tewes	2
J. Knox	2
LRL Berkeley,	
R. K. Wakerling	
E. Teller	
D. M. Wilkes	

No. of Copies

LRL Mercury,

Larry Crooks

External Distribution,

TID-4500, UC-35, Nuclear Explosions-Peaceful Applications 273

Department of Mines and Technical Surveys, Ottawa, Ontario, Canada
D. J. Convey 2

Oil and Gas Conservation Board, Calgary, Alberta, Canada
Dr. G. W. Govier 2

U. S. Army Engineer Division, Lower Mississippi Valley
Vicksburg, Mississippi

U. S. Army Engineer District, Memphis, Tennessee

U. S. Army Engineer District, New Orleans, Louisiana

U. S. Army Engineer District, St. Louis, Missouri

U. S. Army Engineer District, Vicksburg, Mississippi

U. S. Army Engineer Division, Mediterranean, Leghorn, Italy

U. S. Army Liaison Detachment, New York, N. Y.

U. S. Army Engineer District, GULF, Teheran, Iran

U. S. Army Engineer Division, Missouri River, Omaha,
Nebraska

U. S. Army Engineer District, Kansas City, Missouri

U. S. Army Engineer District, Omaha, Nebraska

U. S. Army Engineer Division, New England, Waltham,
Massachusetts

U. S. Army Engineer Division, North Atlantic, New York, N.Y.

U. S. Army Engineer District, Baltimore, Maryland

U. S. Army Engineer District, New York, N.Y.

U. S. Army Engineer District, Norfolk, Virginia

U. S. Army Engineer District, Philadelphia, Pennsylvania

U. S. Army Engineer Division, North Central, Chicago, Illinois

U. S. Army Engineer District, Buffalo, New York

U. S. Army Engineer District, Chicago, Illinois

U. S. Army Engineer District, Detroit, Michigan

U. S. Army Engineer District, Rock Island, Illinois

U. S. Army Engineer District, St. Paul, Minnesota

U. S. Army Engineer District, Lake Survey, Detroit, Michigan

U. S. Army Engineer Division, North Pacific, Portland, Oregon

U. S. Army Engineer District, Portland, Oregon

U. S. Army Engineer District, Alaska, Anchorage, Alaska

U. S. Army Engineer District, Seattle, Washington

U. S. Army Engineer District, Walla Walla, Washington

No. of Copies

U. S. Army Engineer Division, Ohio River, Cincinnati, Ohio

U. S. Army Engineer District, Huntington, West Virginia

U. S. Army Engineer District, Louisville, Kentucky

U. S. Army Engineer District, Nashville, Tennessee

U. S. Army Engineer District, Pittsburgh, Pennsylvania

U. S. Army Engineer Division, Pacific Ocean, Honolulu, Hawaii

U. S. Army Engineer District, Far East, San Francisco, California

U. S. Army Engineer District, Honolulu, Hawaii

U. S. Army Engineer District, Okinawa, San Francisco, California

U. S. Army Engineer Division, South Atlantic, Atlanta, Georgia

U. S. Army Engineer District, Canaveral, Merritt Island, Florida

U. S. Army Engineer District, Charleston, South Carolina

U. S. Army Engineer District, Jacksonville, Florida

U. S. Army Engineer District, Mobile, Alabama

U. S. Army Engineer District, Savannah, Georgia

U. S. Army Engineer District, Wilmington, North Carolina

U. S. Army Engineer Division, South Pacific, San Francisco, California

U. S. Army Engineer District, Los Angeles, California

U. S. Army Engineer District, Sacramento, California

U. S. Army Engineer District, San Francisco, California

U. S. Army Engineer Division, Southwestern, Dallas, Texas

U. S. Army Engineer District, Albuquerque, New Mexico

U. S. Army Engineer District, Fort Worth, Texas

U. S. Army Engineer District, Galveston, Texas

U. S. Army Engineer District, Little Rock, Arkansas

U. S. Army Engineer District, Tulsa, Oklahoma

Mississippi River Commission, Vicksburg, Mississippi

Rivers and Harbors, Boards of Engineers, Washington, D. C.

Corps of Engineer Ballistic Missile Construction Office Norton Air Force Base, California

U. S. Army Engineer Center, Ft. Belvoir, Virginia

U. S. Army Engineer School, Ft. Belvoir, Virginia

U. S. Army Engineer Reactors Group, Ft. Belvoir, Virginia

No. of Copies

U. S. Army Engineer Training Center, Ft. Leonard Wood, Missouri

U. S. Coastal Engineering Research Board, Washington, D. C.

U. S. Army Engineer Nuclear Cratering Group, Livermore, California 50

wf:jd